ELSEVIER

Since January 2020 Elsevier has created a COVID-19 resource centre with free information in English and Mandarin on the novel coronavirus COVID-19. The COVID-19 resource centre is hosted on Elsevier Connect, the company's public news and information website.

Elsevier hereby grants permission to make all its COVID-19-related research that is available on the COVID-19 resource centre - including this research content - immediately available in PubMed Central and other publicly funded repositories, such as the WHO COVID database with rights for unrestricted research re-use and analyses in any form or by any means with acknowledgement of the original source. These permissions are granted for free by Elsevier for as long as the COVID-19 resource centre remains active.

CHAPTER SEVEN

Computer simulations of protein–membrane systems

Jennifer Loschwitz[a,b], **Olujide O. Olubiyi**[b,c], **Jochen S. Hub**[d], **Birgit Strodel**[a,b], **Chetan S. Poojari**[d,*]
[a]Institute of Theoretical and Computational Chemistry, Heinrich Heine University Düsseldorf, Düsseldorf, Germany
[b]Institute of Biological Information Processing (IBI-7: Structural Biochemistry), Forschungszentrum Jülich, Jülich, Germany
[c]Department of Pharmaceutical Chemistry, Faculty of Pharmacy, Obafemi Awolowo University, Ile-Ife, Nigeria
[d]Theoretical Physics and Center for Biophysics, Saarland University, Saarbrücken, Germany
*Corresponding author: e-mail address: chetan.poojari@uni-saarland.de

Contents

1. Introduction 277
  1.1 Lipid diversity: The scaffold of biological membranes 280
  1.2 Membrane proteins: The complexity of biological membranes 288
  1.3 Lipid rafts and hydrophobic mismatch: The regulation and organization of biological membranes 290
  1.4 Role of MD simulations in investigating protein–membrane systems 291
2. Lipid force fields 294
  2.1 Atomistic force fields for lipids 296
  2.2 Coarse-grained force fields for lipids 314
  2.3 Which lipid FF to choose for a simulation? 323
3. MD simulation setup and analysis of protein–membrane systems 324
  3.1 CHARMM-GUI 324
  3.2 Setting up protein–membrane system with other programs 327
  3.3 MD simulation software packages 329
  3.4 Analysis tools for studying protein–membrane systems 330
4. Case studies for protein–membrane systems 331
  4.1 Atomistic simulations of integral membrane proteins 331
  4.2 Atomistic simulations of membrane-associated proteins 345
  4.3 Coarse-grained simulations of membrane proteins 367
5. Conclusions and future directions 376
Acknowledgments 378
References 378

Abstract

The interactions between proteins and membranes play critical roles in signal transduction, cell motility, and transport, and they are involved in many types of diseases. Molecular dynamics (MD) simulations have greatly contributed to our understanding

Progress in Molecular Biology and Translational Science, Volume 170
ISSN 1877-1173
https://doi.org/10.1016/bs.pmbts.2020.01.001

© 2020 Elsevier Inc.
All rights reserved.

of protein–membrane interactions, promoted by a dramatic development of MD-related software, increasingly accurate force fields, and available computer power. In this chapter, we present available methods for studying protein–membrane systems with MD simulations, including an overview about the various all-atom and coarse-grained force fields for lipids, and useful software for membrane simulation setup and analysis. A large set of case studies is discussed.

Abbreviations

Computational methods

AA	all-atom or atomistic
AMBER	assisted model building and energy refinement
CHARMM	Chemistry at Harvard Macromolecular Mechanics
COM	center of mass
CLI	command line interface
CG	coarse-grained
ELBA FF	electrostatic-based FF
FF	force field
GROMOS	Groningen molecular simulation package
GUI	graphical user interface
HMMM	highly mobile membrane mimetic
LJ	Lennard-Jones
MD	molecular dynamics
MM	molecular mechanics
MM/PBSA	molecular mechanics Poisson–Boltzmann surface area
OPLS	optimized parameters for liquid simulations
PME	particle-mesh Ewald
QM	quantum mechanics
RESP	restricted electrostatic potential
TMD	targeted MD
UA	united atom
vdW	van der Waals

Experimental methods and databases

AFM	atomic force microscopy
cryo-EM	cryo-electron microscopy
EPR	electron paramagnetic resonance
FCS	fluorescence correlation spectroscopy
FRAP	fluorescence recovery after photobleaching
FRET	Förster resonance energy transfer
HDX-MS	hydrogen–deuterium exchange MS
MS	mass spectroscopy
NMR	nuclear magnetic resonance
OPM	orientations of proteins in membranes
PDB	protein data bank
PPM	position of proteins in membrane
SFG	sum frequency generation

Lipids, membranes, and related structures

ALA	α-linolenic acid
ARA	arachidonic acid
CHOL	cholesterol
CL	cardiolipin
DB	double bond
DCLE	1,1-dichloroethane
DGDG	digalactosyldiacylglycerol
DHA	docosahexaenoic acid
DLPC	dilauroylphosphatidylcholine
DMPC, DMPG	dipalmitoylphosphatidyl-choline, -glycerol
DOPC, DOPS	dioleoylphosphatidyl-choline, -serine
DPhPC	diphytanoylphosphatidylcholine
DPPC, DPPG	dipalmitoylphosphatidyl-choline, -glycerol
DSPC, DSPE	distearoylphosphatidyl-choline, -ethanolamine
DVPC, DVPS	divalerylphosphatidyl-choline, -serine
ER	endoplasmic reticulum
ER-phagy	ER-autophagy process
GPI	glycosylphosphatidylinositol
GPL	glycerophospholipid
GPMV	giant plasma membrane vesicle
GUV	giant unilamellar vesicle
GluCer	glucosylceramide
HB	hydrogen bond
LA	linoleic acid
LD	lipid droplet
LPC	lysophosphatidylcholine
LPS	lipopolysaccharides
MGDG	monogalactosyldiacylglycerol
PC, PE, PG	phosphatidyl-choline, -ethanolamine, -glycerol
PI	phosphatidyl-inositol
PIP	phosphatidylinositol-(3,4 or 5)-monophosphate
PIP(4,5)$_2$	phosphatidylinositol-4,5-biphosphate
PIP(3,4,5)$_3$	phosphatidylinositol-3,4,5-triphosphate
POPA, POPC	palmitoyloleoylphosphatidyl-acid, -choline
POPG, POPS	palmitoyloleoylphosphatidyl-glycerol, -serine
PS	phosphatidyl-serine
PUFA	polyunsaturated fatty acid
ROS	reactive oxygen species
SAPC	stearoylarachidonoylphosphatidylcholine
SDPC	stearoyldocosahexaenoylphosphatidylcholine
SDS	Sodium dodecyl sulfate
SLAS	sodium lauroyl sarcosine
SM	sphingomyelin
SOPC	stearoyloleoylphosphocholine
***sn*-1**	acyl chain of GPLs at the position 1 of glycerol
***sn*-2**	acyl chain of GPLs at the position 2 of glycerol
TG	triglyceride

Proteins, cofactors, and other biomolecules

$A_{2A}R$	adenosine A receptor
$A\beta$	amyloid-β
ABP	actin-binding protein
AD	Alzheimer's disease
apo A-1	apolipoprotein A-1
APP	amyloid precursor protein
AQP1	aquaporin-1
aSyn	α-synuclein
ATP	adenosine triphosphate
β_2AR	β_2-adrenergic receptor
CcO	cytochrome c oxidase
COX1	prostaglandin H2 synthase
δ-OPR	delta opioid receptor
DNA	deoxyribonucleic acid
hDAT	human dopamine transporter
hIAPP	human islet amyloid polypeptide
EGFR	epidermal growth factor receptor
FGF	fibroblast growth factor
GEF	guanine nucleotide exchange factor
Glc	glucose
GluA2	AMPA-sensitive glutamate receptor 2
GLUT1	glucose transporter 1
GPCR	G protein-coupled receptors
GRP1	general receptor of phosphoinositides 1
GTP	guanosine triphosphate
HDL	high-density lipoprotein
Kir2.1	inwardly rectifying potassium
Kiv1.2	voltage-dependent Shaker K^+ channel 1.2
LC3	light chain 3
LIR	LC3-interacting region
MSP	membrane scaffolding protein
NAC	nonamyloid-β component
NADH	nicotinamide adenine dinucleotide
Neu5Ac or NANA	N-acetylneuraminic acid
OMPF	outer membrane porin F
Pgp	P-glycoprotein
PH	pleckstrin homology
PMPs	peripheral membrane proteins
RHD	reticulon-homology-domain
RVFV	Rift valley fever virus
T2D	type 2 diabetes
TM	transmembrane
TMH	transmembrane helix
TLR4	toll-like receptor 4

1. Introduction

The complexity of biological systems constitutes one of the greatest fascinations for the research world, a complexity most easily exemplified in biological membranes. The interest in membrane structures has progressively risen in the last 50 years for various reasons, including the realization that about ∼50% of drug targets are membrane proteins.[1,2] Thus, developing new drug compounds against membrane proteins requires an understanding of the membrane-based macromolecular targets both in terms of composition and the specific and nonspecific interactions formed within the matrix constituted by biological membranes. The kingdom of life can be divided into prokaryotes (bacteria and archaea) and eukaryotes (animals, plants, and fungi), which exhibit different kind of cell structure and can be seen in Fig. 1A.

Membranes are characteristic of individual biological cells as well as their subcellular structures. For instance, they determine cell identity and in the eukaryotic cells membrane constitutions vary among organelles like the endoplasmic reticulum (ER), mitochondria, vesicles, or chloroplasts in plants. In contrast prokaryotes (bacteria or archaea) are unicellular and feature a plasma membrane and no organelles (Fig. 1A). By serving as a barrier between the cell and its environment as well as between subcellular compartments, membranes are crucial for cell survival and most cellular processes. For all cell types, the plasma membrane defines the cellular barrier, controlling the transport of molecules across the membrane structure and aids in signal transmission, e.g., in response to stress. In the eukaryotes, lipids and proteins synthesized in the ER and Golgi, respectively, are packaged inside and transported to their destinations by membrane-bound vesicles. Membrane-enclosed nucleus stores the cells genetic information as deoxyribonucleic acid (DNA), while the mitochondria produce energy in form of adenosine triphosphate (ATP) required for cellular processes and regulation. Vesicles transport nutrients, lipids, and proteins to different cell compartments or extracellularly secrete certain important substrates. Lysosomes, which are also membrane-enclosed, host different hydrolytic enzymes for the degradation of various classes of biomolecules (e.g., proteins, lipids, and ligands of receptors). An exception are the human erythrocytes (red blood cells) for the transport of oxygen and carbon dioxide via carrier protein hemoglobin throughout the body. In these cells, the nuclei and most of other organelles are missing to provide more space for hemoglobin.[2a,b]

Bacteria exhibit an additional cell wall, which consists of branched peptidoglycans and no membrane lipids are included. They can be divided in two subclasses: Gram-positive bacteria have a thick cell wall and are positive

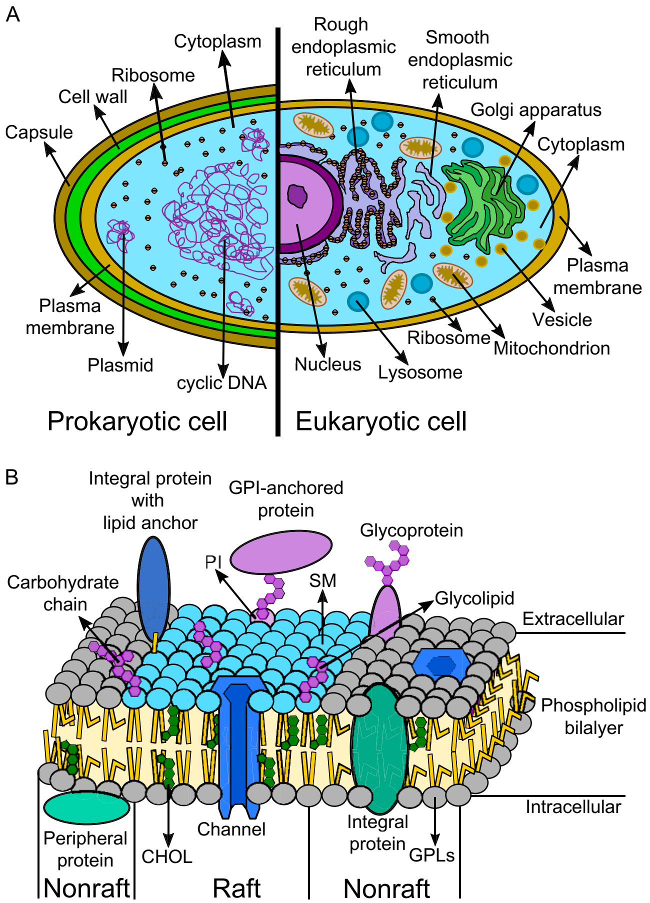

Fig. 1 Illustration of cell structures and membrane model. (A) Comparison between prokaryotic and eukaryotic cells. In prokaryotes, like bacteria and archaea, the cell exhibits no compartmentalization, thus, only the plasma membrane exists as barrier shielding the single circular DNA molecule as well as small plasmids along with all other metabolites in cytoplasm. Bacteria also have a cell wall of branched peptidoglycans in addition to the cell membrane. Most eukaryotes feature a membrane-bound nucleus and other organelles like ER, mitochondria, and the Golgi apparatus. In contrast to animals, plant cells have intracellular chloroplasts for photosynthesis, huge water vacuoles and a cell wall that contains plasmodesmata for a special cell–cell communication with the neighbor cells (not shown). (B) The fluid mosaic model describes a lipid bilayer which separates two different environments (intracellular/extracellular or luminal/cytosolic). The bilayer contains lipids that provide a structural scaffold for the membrane system. Integral and peripheral proteins that may contain posttranslational modifications (e.g., glycosylation by several sugars, leading to glycoproteins or -lipids) are found in membranes, serving as transporters and channels for substrates as well as receptors for transmembrane signal transfer. In the last years, the lipid-raft theory has become popular, in which the membrane is separated in nonraft (disordered region, L_d) with polyunsaturated glycerophospholipids (GPLs) and raft-like regions (ordered region, L_o) with high contents of cholesterol (CHOL) and sphingomyelin (SM) in the outer leaflet. Furthermore, proteins and lipids with glycosylation modification as well as glycosylphosphatidylinositol (GPI)-anchored proteins are enriched in L_o regions.

to the Gram stain test with crystal violet, which can be seen under the microscope. In contrast, Gram-negative bacteria exhibit a thin peptidoglycan cell wall that is sandwiched together with the periplasm between the inner cytoplasmic cell membrane and an additional outer membrane. The outer membrane protects the Gram-negative bacteria from many antibiotics and contains lipopolysaccharides (LPS) which can have toxic properties. Most archaea are extremophiles which can live in nonphysiological conditions, e.g., very high or low temperatures, at high salt concentrations or low pH values. Some of them exhibit a cell wall with pseudopeptidoglycans, which are structurally and physically similar to the bacterial peptidoglycans. In contrast to bacterial and eukaryotic cell membranes, their lipids are not ester-linked but more stable ether-linked, thus, which might be the reason of survival in extreme environments (see Section 1.1 for more information).

The total lipid composition of the cell membranes, called also as lipidomics, are required together with the corresponding proteins for fulfilling cellular functions and for providing the right environment for the chemical reactions unique to each cell. The plasma membrane in multicellular organisms exhibits a relative lipids to proteins composition of roughly 1:1 ratio, with the more precise ratio depending on the cell type. The membrane is crowded with about 15–30% of proteins[3] that are asymmetrically distributed laterally within the membrane structure and between the two leaflets. This contributes to the high complexity of biological membranes. The complex and dynamic structure of membrane systems was described by the fluid mosaic model (Fig. 1B) first introduced by Singer and Nicolson.[4] This model illustrates the organization of heterogeneous sets of components, including the lipid bilayer, integral and peripheral proteins (enzymes, channels and transporters), and modifications, like glycosylation of proteins and lipids. Over four decades, the model has successively been extended to a more complex model, capturing important phenomena such as membrane curvature, lateral and vertical heterogeneity of lipids and proteins distribution, differential occupancy of transmembrane, peripheral and extramembrane proteins as well as the cytoskeleton structure of the cell.[5–7]

In Sections 1.1–1.4, a short overview of the complexity of biological membranes is provided, including a brief introduction of the different types of lipids, proteins, and their modifications found in membranes. In Section 2, we examine the contributions of all-atom and coarse-grained force fields for modeling protein–membrane assemblies using molecular dynamics (MD) simulations. In Section 3, we present the general setting up and analysis of protein–membrane MD simulations. And finally in Section 4, we present selected case studies employing atomistic and/or coarse-grained force field-based MD simulations in studying different aspects of protein–membrane systems.

1.1 Lipid diversity: The scaffold of biological membranes

Biological membranes bounding cells and organelles typically comprise a lipid bilayer, forming a scaffold and usually consisting of more than a hundred lipid species. The dynamic barrier formed by this structural scaffold plays an important role for communication between different cells, between the intracellular and extracellular environments of a cell, as well as between an organelle's lumen and the cytosol. The lipid membranes additionally regulate the transport of substances, like nutrients into the cell and potentially toxic components out of the cells. Lipids are also involved in signaling processes, serving as energy resources, posttranslational modifications, and recruitment of proteins.

The diverse roles played by the membrane largely derive from the structural features of the lipids. Biological lipids share a common amphipathic character, containing a long hydrocarbon or acyl tail, that is distinctively hydrophobic, and a hydrophilic head group, which may possess a net charge. This amphipathic nature allows for a thermodynamically efficient spontaneous formation of a bilayer driven by the hydrophobic effect within a predominantly aqueous environment.[8] The inability of the nonpolar hydrocarbon chains to form hydrogen bonds with water contributes to the orientation of the hydrophobic tail away from water molecules, a process that is associated with an entropic term. The entropy S term defines the disorder of a system and is connected to the free energy change ΔG, the absolute temperature T and the enthalpy change ΔH according to Eq. (1).

$$\Delta G = \Delta H - T\Delta S \tag{1}$$

The lack of hydrogen bonds between the hydrophobic lipid tails and water would impose a cage-like ordering of water molecules around the hydrophobic parts of lipids, which would cause a decrease in ΔS of water (i.e., ΔS would become negative) and thus lead to a positive and thermodynamically unfavorable ΔG. In order to minimize contact with water and thus the entropic decrease, the hydrocarbon chains self-assemble and orient away from the aqueous medium. This effect is known as the hydrophobic effect and constitutes the fundamental mechanism governing the formation of lipid membrane structures. In this orientation the polar head groups interact with water molecules and other polar head groups that together form the contact area with the aqueous environment. This picture of membrane lipid assembly represents a highly simplified illustration of the membrane structure, with structural properties of different lipid types. An overview of the different types of membrane lipids found in biological membranes is presented in Fig. 2.

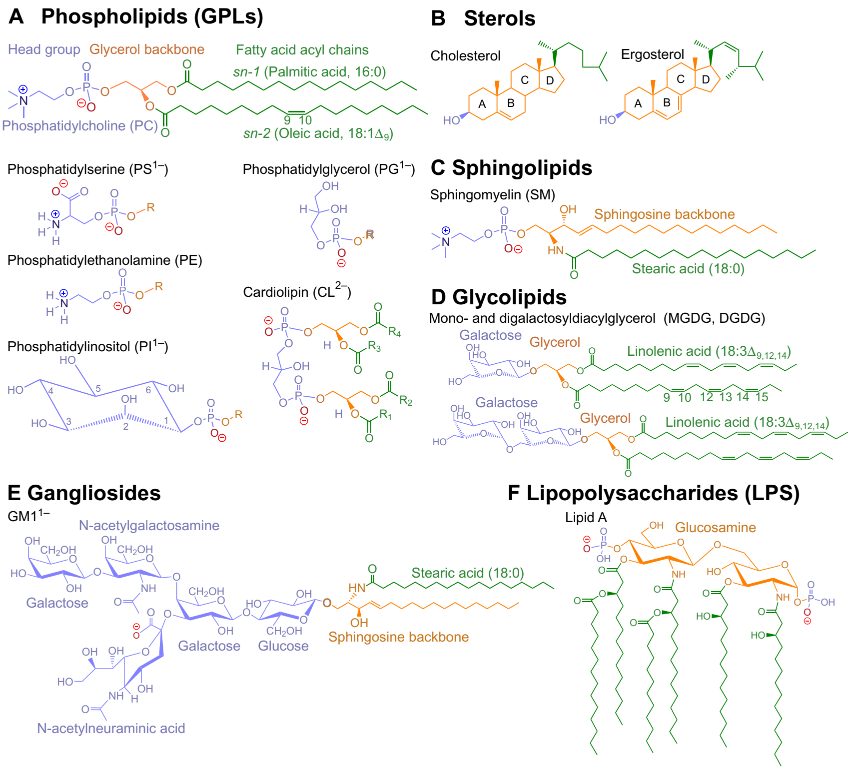

Fig. 2 Structure of membrane lipids. (A) GPLs or phospholipids represent the major components of membranes. The chemical structure of a palmitoyloleoylphosphatidylcholine (POPC– 16:0,18:1) molecule is shown, containing the polar head group indicated in *blue*, the glycerol backbone in *orange*, and two hydrophobic acyl chains in *green*. The positively charged atoms are shown in *dark blue* and the negatively charged atoms in *red*. Additionally, the different kinds of head groups, typically found in cell membranes, are displayed and in their corresponding abbreviation and net charge given in *parentheses*. (B) Sterols consist of a planar, four-ring system shown in *orange*, a hydrophobic acyl chain in *green*, and a polar hydroxyl group in *blue*. The common sterols cholesterol and ergosterol are shown. (C) Similar to GPLs, sphingolipids exhibit a polar head group (choline, serine, or ethanolamine), which is bound to the sphingosine backbone shown in *orange*, and a hydrocarbon chain with a typical length of 16–26 carbon atoms fused to sphingosine via N-acylation. (D) Glycolipids exhibit a sugar as polar head group instead of a phosphatidyl moiety in GPLs. The sugar head can contain one or two saccharides, e.g., mono- and digalactosyldiacylglycerol (MGDG, DGDG). (E) Another and complex class of sphingolipids comprises the gangliosides, containing sphingosine as backbone bound to an acyl chain and sugar acids as polar head group. One or more of the sugar groups are N-acetylneuraminic acid (NANA or Neu5Ac). To show the complexity of gangliosides, GM1, where G refers to ganglioside and M is for monosialic, is depicted. (F) Lipid A is an example for lipopolysaccharides (LPS).

The glycerophospholipids (GPLs, popularly referred to as phospholipids) represent the major component (up to ~75%) of most biological membranes. Like the name suggests, the head group of GPLs contains a phosphate and a glycerol group. The phosphate group is esterified at the *sn*-3 position of glycerol, whereas the fatty acid (or acyl) chains are esterified at *sn*-1 and *sn*-2 positions of the glycerol thus forming the hydrophobic region of the membrane (Fig. 2A). Usually, GPLs bear a total of one, two, or four fatty acid chains, with each chain containing between 12 and 24 carbons and sometimes featuring up to six double bonds. For instance, palmitic acid, an hexadecanoic acid that exhibits 16 carbons and no double bonds (DB), codified as 16:0 to represent the $N_{\mathrm{carbons}}:N_{\mathrm{DB}}$ ratio, whereas oleic acid has 18 carbon atoms and one double bond at the carbon atom 9 (i.e., octadecenoic acid) and is therefore labeled as $18:1\Delta_9$ or $18:1_{\omega 9}$. Unsaturated fatty acids in *cis* conformation introduce kinks in the chain and cause voids in the hydrophobic part of the membrane (packing defects) with the result that the bilayer is more fluid and flexible. In Table 1 the common fatty acids found in biological membranes are listed.[9]

The class of polyunsaturated fatty acids (PUFAs), which exhibit more than one double bond, include the essential omega-3 (ω3) and omega-6 (ω6) fatty acids. Here, the number following the omega characterizes the position of the first double bond with respect to the terminal methyl group in the chemical structure. For example, in the (ω3)-PUFAs the first unsaturation bond appears at the third carbon atom from the end of the acyl chain. For humans, linoleic ($18:2_{\omega 6}$, LA) and α-linolenic acid ($18:3_{\omega 3}$, ALA) belong to the essential PUFAs, which have to be obtained via food like seeds, nuts, and oils and from which longer PUFAs like arachidonic ($20:4_{\omega 6}$, ARA) and docosahexaenoic acid ($22:6_{\omega 3}$, DHA) can be synthesized. However, the biosynthesis of DHA from ALA is rather endogenous and so limited in humans to a maximum of 4%,[10] thus, DHA is mainly derived from food like fish oil. Many of the PUFAs are located in biological membranes. For instance, DHA is contained in the retina and in brain membranes, where it has a modulation function on membrane proteins, the transport of choline, glycine, and taurine, as well as on the response of rhodopsin[11] (see Section 4.2.1 for a case study, in which DHA is involved in Alzheimer's disease).

Table 1 Some native saturated and unsaturated fatty acids found in biological membranes.

Symbol	Condensed formula	Common name (systematic name)	Melting point (°C)
12:0	$CH_3(CH_2)_{10}COOH$	Lauric (*n*-Dodecanoic)	44.2
14:0	$CH_3(CH_2)_{12}COOH$	Myristic (*n*-Tetradecanoic)	53.9
16:0	$CH_3(CH_2)_{14}COOH$	Palmitic (*n*-Hexadecanoic)	63.1
18:0	$CH_3(CH_2)_{16}COOH$	Stearic (*n*-Octadecanoic)	69.6
20:0	$CH_3(CH_2)_{18}COOH$	Arachidic (*n*-Eicosanoic)	76.5
24:0	$CH_3(CH_2)_{22}COOH$	Arachidic (*n*-Tetracosanoic)	86.0
16:1	$CH_3(CH_2)_5CH{=}CH(CH_2)_7COOH$	Palmitoleic ($16{:}1_{\omega 9}$)	−0.5
18:1	$CH_3(CH_2)_7CH{=}CH(CH_2)_7COOH$	Oleic ($18{:}1_{\omega 9}$)	13.4
18:2	$CH_3(CH_2)_4CH{=}CHCHCH_2CH{=}CH(CH_2)_7COOH$	Linoleic ($18{:}2_{\omega 6}$, LA)	−5.0
18:3	$CH_3CH_2CH{=}CHCH_2CH{=}CHCH_2CH{=}CH(CH_2)_7COOH$	Linoleneic ($18{:}3_{\omega 3}$, ALA)	−11.0
20:4	$CH_3(CH_2)_4(CH{=}CHCHCH_2)_3CH{=}CH(CH_2)_3COOH$	Arachidonic ($20{:}4_{\omega 6}$, ARA)	−49.5
22:6	$CH_3(CH_2CH{=}CH)_6(CH_2)_2COOH$	Docosahexaenoic ($22{:}6_{\omega 3}$, DHA)	−44.0

The melting point for each fatty acid is given to assess the phase state at room temperature. Normally, the saturated fatty acids are solid and unsaturated species exhibit the liquid state at room temperature.

The complexity of the GPLs derives not only from the diversity of their head groups but also from the structural varieties of the acyl chains in terms of length, stereochemistry, degree of saturation and hydroxylation of the lipid tails, and the presence of other lipid types. As a consequence, different combinations of the head group structures and acyl chains can lead to different polymorphic shapes of lipids (Fig. 3). In the crystalline liquid state

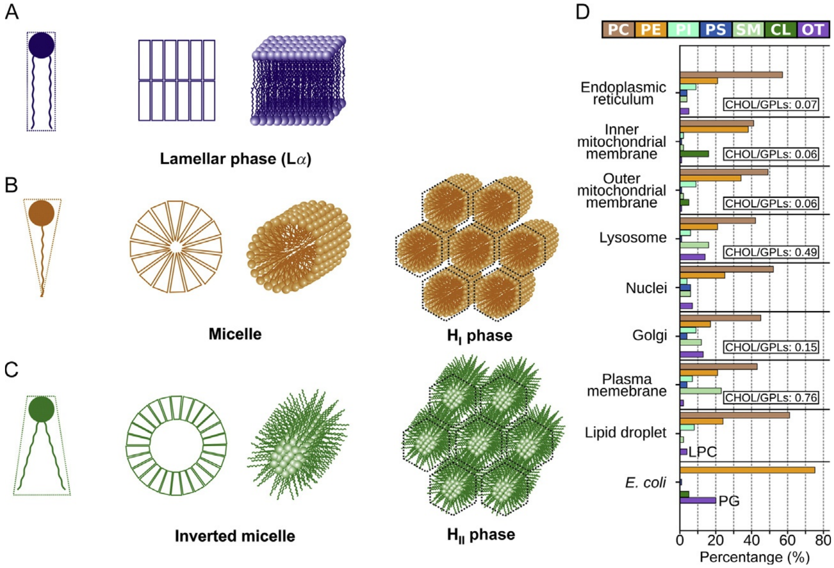

Fig. 3 The polymorphism of lipid assemblies in aqueous solution and the lipid composition of certain organelles. (A) The lamellar phase describes the typical lipid bilayer which is found in biological membranes. It can exist in two major states: First, the crystalline liquid phase (L_α) with the unsaturated and saturated acyl chains in *gauche* conformation providing free spaces within the hydrophobic part to accommodate protein conformational changes and a certain degree of passive permeability. The second extreme phase is the gel phase (L_β, not shown), involving all saturated acyl chains in *trans* conformation and the barest minimum levels of flexibility. This phase is generally not favored in biological membranes. The lipids PC, SM, PS, CL, PA, PG, and PI can form lipid bilayers as they have a rectangular shape. (B) Micellar and H_I shapes are induced by lipids with one acyl chain (lysophospholipids), in which the bulky polar groups are oriented toward the surrounding water, while the acyl chains associate with one another at the core. Lysophospholipids and detergents exhibit an inverted cone shape. (C) Lipids with polar head groups much smaller in comparison to the acyl chains (e.g., PE) or in low pH conditions (e.g., PA and PS under pH 3) or in the presence of divalent cations like Ca^{2+} (CL, PA) favor the inverted micellar or H_{II} structure.[16] Here, the polar groups form an own aqueous phase inside the inverted micellar structure and the acyl chains face the water phase. (D) The bar plot represents the relative abundance of each class of GPLs/SM in organelles based on composition data from different sources,[17] for lipid droplets from murine hepatocytes[18] and *Escherichia coli*.[19] The bar for other lipids (OT) includes PG, PA, and lysophospholipids (e.g., lysophosphatidylcholine, LPC), if it not otherwise mentioned. All data are given in mol%. Additionally, the molar ratio of cholesterol (CHOL) to GPLs is shown for certain organelles.[17] *Panels A–C: Reprinted with the permission from Lladó V, López DJ, Ibarguren M, et al. Regulation of the cancer cell membrane lipid composition by NaCHOleate: effects on cell signaling and therapeutical relevance in glioma. Biochim Biophys Acta Biomembr 2014;1838(6):1619–1627, https://doi.org/10.1016/j.bbamem.2014.01.027. Copyright 2014 Biochimica et Biophysica Acta (BBA)—Biomembranes.*

(lamellar phase or L_α, Fig. 3A), biological membranes adopt the shape of a lipid bilayer, which enhances mobility of the membrane components and passive permeability for water and other small molecules. In this phase, the acyl chains can exist in the all-*trans* or one of the two *gauche* conformations. The latter causes a kink in the acyl chain and thus generates space in the hydrophobic bilayer region, increasing its passive permeability. In contrast, the nonnative ordered gel phase of a lipid bilayer (L_β) forms when most of the acyl chains adopt the very rigid all-*trans* state. Generally, GPLs contain an unsaturated fatty acid with one or two double bonds at the *sn*-2 and a saturated or monounsaturated fatty acid at the *sn*-1 position of glycerol.[12,13] GPLs with only one acyl chain at the *sn*-1 position are called lysophospholipids and act as signaling molecules for the activation of membrane proteins. They are also involved in the generation of micellar structures, in which the polar head groups orient to the water phase and the acyl chains associate in the core (Fig. 3B).

The classification of GPLs is based on the head groups and the fatty acid content. The simplest GPL is phosphatidic acid (PA), which is negatively charged at physiological pH and exists as an intermediate during the biosynthesis of other lipids. It is generally not highly present in biological membranes. Mammalian cell membranes are mostly populated by GPLs with phosphatidylcholine (PC) head groups, in which the phosphate is connected with the alcohol choline. Interestingly, PCs are almost absent in prokaryotic cells. Under physiological conditions, PC is zwitterionic ($^{+}N(CH_3)_3$, PO_4^-) with a zero net charge. Zwitterionic phosphatidylethanolamines (PE) are found in all cell membranes, but in higher quantities in prokaryotic cells. In contrast, they are almost restricted to the inner leaflet of the plasma membrane (cytosolic side) in eukaryotes. The polar group of PE ($^{+}NH_3$, PO_4^-) displays stronger intramolecular interactions than PC and is more nonpolar in the aqueous phase, with the result that an hexagonal H_{II} arrangement (Fig. 3C) is more stable in an inverted orientation than in a micelle. In the inverted orientation, the polar PE groups are oriented toward the core region, whereas the acyl chains are extended outwards into the surrounding water. PE is the major GPL class in bacteria cell membranes together with phosphatidylserine (PS), phosphatidylglycerol (PG), and cardiolipin (CL or diphosphatidylglycerol). While the head group of PS is negatively charged ($^{+}NH_3$, PO_4^-, COO^-) and is mostly located in the inner leaflet of eukaryotic and prokaryotic cells, PG (also negatively charged) and CL (four fatty acid chains, twice negatively charged) have only been found in mitochondrial membranes of eukaryotes and in most of the bacterial plasma membranes.

The localization of CL to mitochondria suggests the evolutionary fusion of prokaryotes, as endosymbionts, with eukaryotic cells in the past. Phosphatidylinositols (PI) represent another class of GPLs that have been found to be involved with lipid and cell signaling, as well as regulation of membrane proteins and membrane trafficking.[14,15] PIs show a high diversity in the head group structure, especially since the hydroxyl groups of inositol can be phosphorylated at positions 3, 4, and 5 to generate any of three PI monophosphates (PI(3)P, PI(4)P, PI(5)P), three bisphosphates (PI(3,4)P_2, PI(3,5)P_2, PI(4,5)P_2), or one triphosphate (PI(3,4,5)P_3). PIs are mostly absent in prokaryotic cells.

The next class of membrane lipids are sterols, which play an essential role in eukaryotic cell, however, they are not found in bacteria and archaea. Cholesterol, also abbreviated as CHOL, is the major component in mammalian cells, which are not able to grow without cholesterol.[9] The chemical structure of cholesterol (Fig. 2B) consists of four fused rings with a double bond in ring B, a hydrocarbon chain at ring D, and a polar hydroxyl group at ring A, leading to a planar conformation with an amphipathic character. The hydroxyl group interacts with the polar head group of GPLs and sphingolipids and is orientated to the water side, whereas the planar ring system and the hydrocarbon chain are in contact with the acyl chains. Interestingly, although ergosterol from yeast shares a very similar structure with cholesterol, they cannot replace each other.[9] The fundamental role of cholesterol is the maintaining and controlling the membrane fluidity by increasing the membrane packing and thickness. Thus, cholesterol decreases the packing defects in the hydrophobic part and encourages the all-*trans* conformation in GPLs, which leads to a decrease of the membrane permeability for ions and small molecules.[9] Furthermore, cholesterol modulates membrane proteins in special conformations by decreasing the free volume in the membrane and mostly inhibits these proteins or can directly bind membrane proteins. Moreover, cholesterol can cause lateral membrane phase separation between cholesterol enriched and poor regions in order to regulate membrane proteins. The concept of lipid rafts will discussed later in this chapter (see Section 1.3).

Similar to GPLs, the sphingolipids in eukaryotic cells represent a further major component of biological membranes. Instead of a glycerol backbone, sphingosine serves as scaffold, in which the acyl chain is N-linked and the head group is O-linked. Sphingomyelin (SM, Fig. 2C), consisting of phosphatidylcholine and stearic acid, is the major sphingolipid in biological membranes (e.g., in human blood cells and membranous myelin sheaths of nerve cell axons) and is normally located in the outer leaflet membrane of cells. Like PC, SM is able to form bilayers in aqueous environment and interacts with cholesterol to build lipid rafts[20,21] (see Section 1.3). Instead of a phosphatidyl group at the position 1 of glycerol, one neutral sugar (typically, galactose, glucose, and lactose) can be covalently bound via glycosidic linkage to form cerebrosides. Additionally, the sugar group can be connected with a sulfate to build the sulfatides. They are found in all kind of species, especially located in brain membranes of mammalians.[22] Fig. 3D shows the distribution of GPLs and SM over the organelles.

Another class of sphingolipids is given by the complex gangliosides, which are based on the sphingosine backbone and a complex sugar acid head group. They play important roles in cell recognition and regulation of membrane proteins and are highly populated in nerve cells.[23] An example is the negatively charged GM1 (Fig. 2E), containing an N-acetylneuraminic acid (Neu5Ac or NANA), N-acetylgalactosamine, two galactose and one glucose (Glc) moiety. It is located in the outer leaflet of nerve cells and is involved in the development of Alzheimer's disease[24,25] (see also Section 4.2.1).

In the plant kingdom, glycerolglycolipids like mono- and digalactosyldiacylglycerol (MGDG, DGDG) have a major role in regulation of the photosynthesis in chloroplasts (Fig. 2D), whereas Lipid A (Fig. 2F) represents a basic component of the outer membrane in Gram-negative bacteria. The chemical structure of Lipid A reveals a glucosamine backbone, containing six acyl groups with chain length between 12 and 14 carbon atoms, as well as two phosphate groups. Lipid A represents the basic part of the lipopolysaccharides (LPS) which contains a core region and a long polysaccharide moiety termed O-antigen. As Lipid A is the main component of the outer membrane, Gram-negative bacteria have a greater intrinsic resistance to antibiotics. In addition, Lipid A acts as endotoxin upon destruction of bacteria cells which provokes immune response in host cells.

The final lipid class, which we want to briefly introduce, are the tetraether bolalipids of the archaea, which feature an ether-linkage between glycerol instead of the ester-linkage typical for eukaryotes and prokaryotes. Moreover, this kind of lipids occurs as dimers by the covalent binding of the end of acyl chains of two lipids to form one molecule with two polar head groups and one or two connected tails. Due to the ether-linkage and the connecting tails, they form highly stable membranes that can sustain incredibly hostile environments, such as extremely high temperatures and pressures, low or high pH values.[26]

With their different head groups, the charge behavior of membrane bilayers has an important impact on the regulation of membrane proteins, an effect which depends on the concentration of Na^+, Ca^{2+}, and Mg^{2+} for anionic GPLs (e.g., CL and PA). The existing potential difference between the two leaflets of the membrane is also very important for survival at the cellular level. Changes in membrane potential are employed in signal transduction by nerve cells and in regulating both cardiac automaticity and contraction by cardiomyocytes. Moreover, the phospholipids, glycolipids, CHOL, and PUFA's are all susceptible to oxidation due to excessive levels of reactive oxygen species (ROS). The oxidized lipids change membrane properties and indirectly affect protein–lipid interactions and other cellular processes, thus leading to cardiovascular, neurodegenerative, and pulmonary diseases. For more information on lipid composition of membranes, the reader is referred to the books[9,16] or the reviews.[12,27,28]

1.2 Membrane proteins: The complexity of biological membranes

We have already examined the complexity of membranes deriving from the diversity of lipids, especially from the different combinations of head groups and acyl chains. Now we want to present the complexity of biological membranes deriving from different classes of membrane proteins, which are known to perform diverse and essential functions. Membrane proteins are involved in protein–lipid interactions for cell–cell recognition, molecular transport across membrane barriers, energy synthesis, maintenance of concentration gradients, signal transduction, as well as formation of vesicles (see Fig. 4A for an overview and specific examples). Membrane proteins can be broadly divided into two classes:

(1) Peripheral proteins directly interacting with the membrane or with integral membrane proteins.

(2) Integral proteins embedded within the membrane or associating with a lipid anchor.

Peripheral proteins are usually not in full contact with the hydrophobic part of the membrane and can be washed off by changing the ionic concentration or pH of the system. In contrast, integral proteins directly interact with the hydrophobic core of membranes with a part of their structure. Examples include lipid anchorage via posttranslational lipidation of amino acids, and interactions involving hydrophobic sequences in transmembrane (TM) α-helices or β-barrel structures (Fig. 4B and D). Membrane proteins with

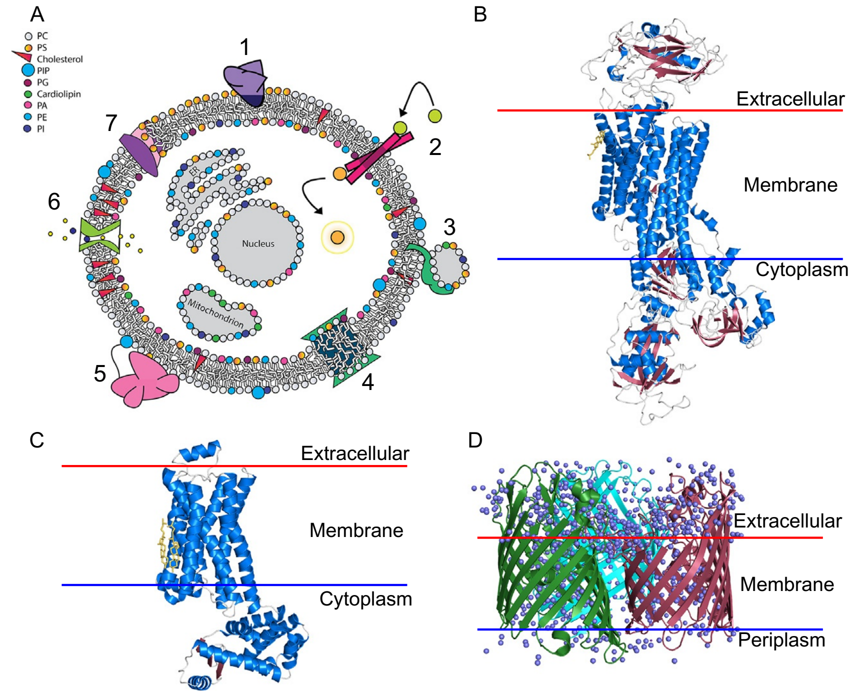

Fig. 4 Membrane protein functions and examples of membrane proteins. (A) Membrane proteins interact with lipids in biological membranes in different ways: (1) A peripheral membrane protein binds with a lipid-specific hydrophobic anchor (PS here). (2) An integral protein, contributing to TM signaling, binds ligands from the outside. (3) A membrane protein binds to and promotes the fusion of a vesicle with the cell membrane. (4) An integral protein induces local curvature via hydrophobic mismatch. (5) A peripheral protein binds a lipid, while its globular domain interacts with the membrane surface. (6) Protein channels regulate ion transport across the membrane via interaction with cholesterol. (7) Phospholipid scramblase transports lipids across the membrane. (B) The structure of the transmembrane Na$^+$K$^+$-ATPase (PDB code: 4HYT[36]), which actively (via ATP hydrolysis) pumps three Na$^+$ ions extracellularly and two K$^+$ into the cytoplasm against its concentration gradient. The pump maintains membrane resting potential, regulates cellular transport, and modulates cell volume. Cholesterol is displayed as *yellow sticks*. (C) The crystallographic structure of the human β2-adrenergic receptor (PDB code: 3D4S[37]), a G-protein-coupled receptor (GPCR) expressed in pulmonary and cardiac myocyte tissue featuring cholesterol (shown as *yellow sticks*) binding sites. (D) The porin OMPF (outer membrane protein F, PDB code: 3POX[38]) shows a β-barrel conformation, which is highly expressed in the outer membrane of *E. coli*. It serves to facilitate the selective entry of hydrophilic molecules (e.g., water molecules, shown as *blue spheres*) into the periplasm. The 3D structures were generated with PyMol version 1.8. *Panel A: Adapted with the permission from Muller MP, Jiang T, Sun C, et al. Characterization of lipid-protein interactions and lipid-mediated modulation of membrane protein function through molecular simulation. Chem Rev. 2019;119(9):6086–6161, https://doi.org/10.1021/acs.chemrev.8b00608. Copyright 2019 American Chemical Society.*

TM α-helices (TMH) are generally found in the plasma membrane and the inner membrane of bacteria cells, while β-barrels (e.g., outer membrane porin F from *Escherichia coli*, OMPF) are located in outer membranes of Gram-negative bacteria, cell walls of gram-positive bacteria, as well as the outer membrane leaflets of mitochondria and chloroplasts. Membrane lipids can influence membrane proteins via direct binding that allosterically affects the conformational preferences. Furthermore, membrane proteins can exhibit posttranslational modifications in form of sugars and GPLs, as seen for instance in glycosylphosphatidylinositol (GPI)-anchored proteins, which have functional roles in membrane protein transport, cell adhesion, cell wall synthesis, and cell surface protection. We will discuss different protein–lipid interactions in the case studies in Section 4.

1.3 Lipid rafts and hydrophobic mismatch: The regulation and organization of biological membranes

In the 1970s, membranes were shown to exhibit lateral heterogeneity using an experimental protocol that extracted membrane proteins and lipids in detergents. Within the past few years, the theory of lipid rafts developed by Simons and Ikonen has become established[29] and involves the accumulation of less flexible lipids for the building of ordered nanodomains, called rafts (L_o, <200 nm, especially via cholesterol, PC and SM), which are surrounded by disordered and more fluid lipid areas (L_d, polyunsaturated acyl chains). This activates membrane proteins in terms of conformational changes or oligomerization. Cholesterol has been observed to play a key role as at concentrations below 10 mol% of cholesterol no domain separation was reported between the phases. This was demonstrated for ternary membrane systems using in vitro methods and in both synthetic giant unilamellar vesicles (GUVs) and giant plasma membrane vesicles (GPMVs)[30,31] extracted from cells, as well as via MD simulations.[32,33] Until now, no experimental technique is available to visualize the process of raft formation in living cells since conventional optical microscopy is limited to a resolution of ~250 nm. Nevertheless, there are evidences for their existence originating from the presence of lipid raft markers which are located in lipid rafts as well as from other biophysical methods (see Refs. 21, 34).

Functional raft-like domains are involved in cellular processes like immune signaling. For instance, the SRC family kinases are located in raft-like domains, where they phosphorylate immune receptor complexes, whereas the phosphatases reside in nonraft domains. Another example is the host–pathogen interactions featured in bacterial or viral infections, involving the binding of specific bacterial toxins and viruses to special membrane proteins in raft-like domains.[21] With the help of microsecond-scale MD simulations, a three-component raft-like system of cholesterol and PC with saturated and unsaturated acyl chains has been successfully built. However, it remains to elucidate the mechanism of assembly of membrane components in different phase domains since this has not been unambiguously shown in living cells with the attendant level of structural complexity.

Another driving force to organize membrane domains derives from the hydrophobic interactions between TM proteins and the different kinds of lipids. In the case of hydrophobic mismatch, which is the difference between the thicknesses of the hydrophobic regions of a TM protein and of the biological membrane, it spans leading to unfavorable exposure of hydrophobic surfaces to water, membrane sorting and orientation of membrane proteins are affected.[21,39] TM proteins and surrounding lipids can adapt to the hydrophobic mismatch by different means. When the hydrophobic part of a TM protein is longer than the hydrophobic bilayer thickness, the protein might aggregate in the membrane to minimize the exposed hydrophobic area, it could tilt to reduce its effective hydrophobic thickness, or adopt a different conformation. Lipids in turn can modulate the membrane thickness by stretching their acyl chains or even assemble into another membrane state. When the hydrophobic part of a TM protein is too small to match the hydrophobic bilayer thickness, again this might result in protein aggregation or changes to its orientation or conformation. Lipids, on the other hand, could decrease the effective bilayer thickness by becoming more disordered or disrupting the bilayer organization to form an inverted nonlamellar structure.

1.4 Role of MD simulations in investigating protein–membrane systems

The biological membranes, as discussed in Sections 1.1–1.3, in composition, organization as well as protein–lipid interactions are highly complex systems. Thus, this complexity constitutes a unique kind of challenge for structural study. While experimental methods can be used to detect protein–lipid interactions, unraveling structural mechanisms at the atomistic level often remains problematic. Many membrane proteins are involved in disease pathologies (e.g., cystic fibrosis, Parkinsonism, Alzheimer's disease, atherosclerosis, and cancer) and to properly understand the molecular events associated with such disease states, their structural dynamics needs to be resolved. For drug development purposes, there is also continual need to investigate protein–lipid interactions.[40] For atomistic insight into protein–lipid interactions, experimental techniques like X-ray crystallography, nuclear magnetic resonance (NMR) spectroscopy, and cryo-electron microscopy (cryo-EM) are often used. X-ray structures in the 1–3 Å resolution range represent an often dynamic system with single snapshots and the crystallization process sometimes involves harsh treatments capable of generating nonnative protein conformations. Furthermore, flexible regions (e.g., loops) cannot be detected by X-ray crystallography. On the other hand, NMR can describe protein dynamics but it is limited to small protein systems of ~50 kDa. Cryo-EM has in recent years become an important tool for investigating protein–lipid association in membranes systems with a resolution of 2–4 Å.[41] Every resolved protein structure is available in the RCBS Protein Data Bank (PDB)[42,43] (https://www.rcsb.org), while the orientation of membrane proteins in biological membranes is provided by the Orientations of Proteins in Membranes (OPM) database[44] (https://opm.phar.umich.edu/).

MD simulations provide a computational complement to these experimental techniques. The history of lipid bilayers studied by MD simulations with no explicit water molecules began in the 1980s with investigations of few lipid molecules.[45–47] After about a decade, MD simulations were successfully employed in the study of increasingly complex and more realistic lipid bilayers, including PCs and PSs with explicit solvents,[48–52] and including embedded proteins.[53–56] These initial studies, however, were limited to conformational sampling on the picosecond timescale. Following the developments in hardware and software, MD simulation have increasingly begun to capture the structural dynamics of larger macromolecular systems, like ribosomes,[57] protein–membrane systems (e.g., transporters and channels),[58,59] virus membranes,[60] and lipid rafts.[32,33] By overcoming the resolution limits of the experimental methods and exploring the fine molecular details of macromolecular events, MD simulations can now serve as *molecular microscope*[35,61] to investigate lipid–lipid and protein–lipid interactions of more realistic cell membranes on submillisecond timescale (Fig. 5A). Different MD simulation techniques apart from traditional all-atom (AA) models have been developed for this purpose. These include coarse-grained (CG) force fields,[62,63] the highly mobile membrane mimetic (HMMM) model,[64] and multiscale models (Fig. 5B). To decrease the calculation time during the MD simulation, CG models represent multiple atom groups as fewer pseudoparticles (so-called beads), while the HMMM model employs a membrane core of organic solvent combined with truncated lipids for the head group region for increasing the lateral diffusion of membrane lipids. However, these approaches imply a loss in resolution such that in CG model small protein conformation changes cannot be captured, while the HMMM model is restricted to modeling peripheral protein–membranes systems.[64]

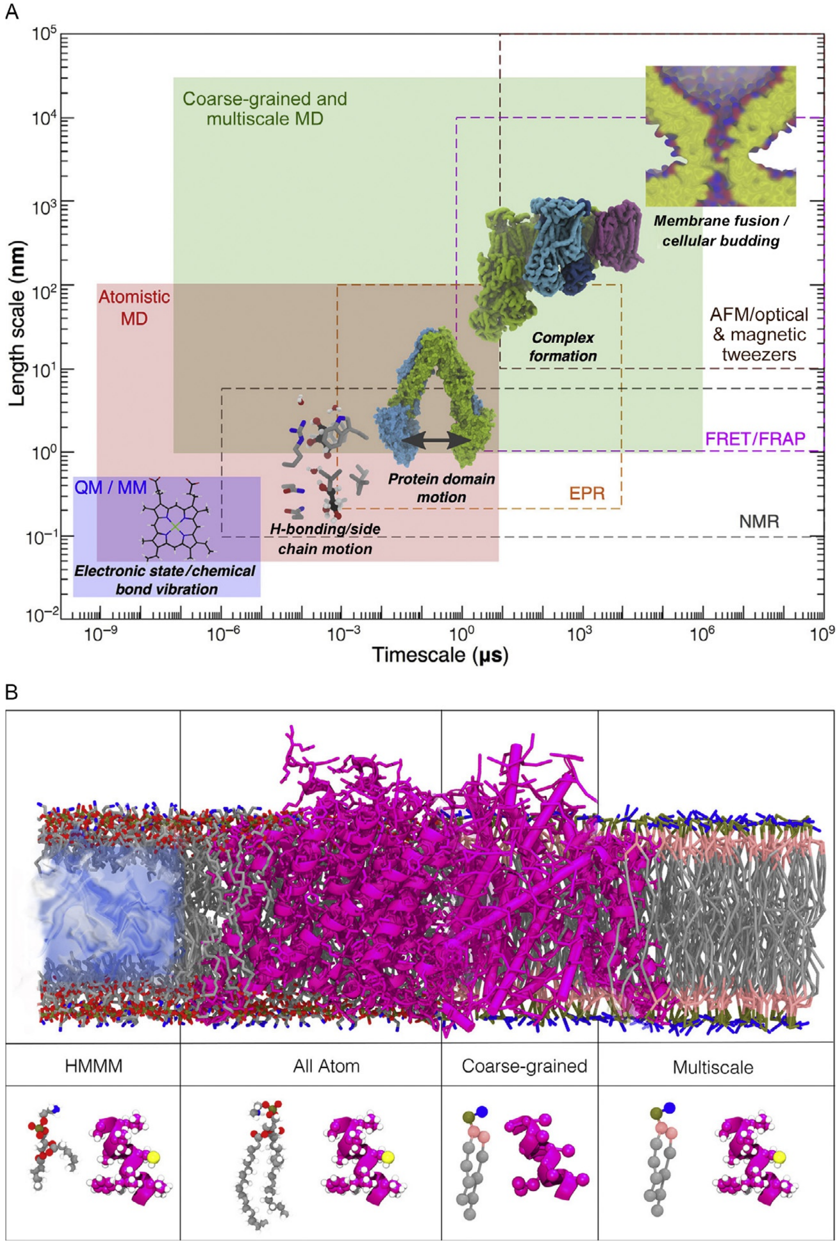

Fig. 5 See legend on next page.

Multiscale methods comprise the use of different levels of representation in performing MD simulations, e.g., starting with CG simulations to extract different large-scale conformations, which are then converted to atomistic structure to study at a better resolution.[65]

In the next Section 2, the different all-atom and coarse-grained models for lipids are discussed, while Section 3 describes how to set up and analyze MD simulations of protein–membrane systems. In Section 4, we describe different case studies of selected AA- and CG-MD simulations to grant a perspective into how MD simulations are employed in studying interactions between lipids and different membrane proteins. The presented systems include associated and integral membrane proteins in interaction with lipids.

2. Lipid force fields

In this section, three groups of lipid FFs will be reviewed. The all-atom (AA) FFs represent the most detailed description, where all atoms of a molecule are described in an explicit manner. The united-atom (UA) FFs merge the nonpolar hydrogens connected to heavy atoms to one interaction site. For instance, the methyl (CH_3) and methylene (CH_2) groups will

Fig. 5 Length- and timescale of experimental and MD simulation methods. (A) Application of methods to analyze the dynamics of chemical and biological processes. The effective length and timescales of QM/MM (quantum mechanics/molecular mechanics), AA, and CG/multiscale simulations are displayed in the *shaded boxes*. The experimental techniques nuclear magnetic resonance (NMR), electron paramagnetic resonance (EPR), Förster resonance energy transfer (FRET), fluorescence recovery after photobleaching (FRAP), atomic force microscopy (AFM), and magnetic and optical tweezers are indicated by the *dashed boxes*. (B) The resolution of different MD simulation techniques in protein–lipids interaction studies is shown. In the *upper panel*, the chloride ion channel (PDB code: 1OTS[66]) is represented in different resolutions, while in the *lower panels* a PS lipid and a short α-helix are displayed with different resolution. All-atom resolution implies explicit treatment of all interactions, whereas in CG simulation certain atoms have been merged into fewer beads. Multiscale simulations involve combining of multiple levels of resolutions either at the same time or in sequence. The highly mobile membrane mimetic (HMMM) model uses truncated lipids and a membrane core of organic solvent for increasing the lateral diffusion of membrane lipids. *Panels A and B: Reprinted with the permission from Muller MP, Jiang T, Sun C, et al. Characterization of lipid-protein interactions and lipid-mediated modulation of membrane protein function through molecular simulation. Chem Rev. 2019;119(9):6086–6161, https://doi.org/10.1021/acs.chemrev.8b00608. Copyright 2019 American Chemical Society.*

each be displayed by a single interaction site, resulting in a decrease of interaction sites from 4 to 1 and 3 to 1, respectively. This leads to lower costs of computing time, while still reaching a similar accuracy as with the AA FFs. The next level of reduction is the summarizing of 3–4 heavy atoms into a single interaction site (known as bead), which is typically called a coarse-grained (CG) model. Important FFs that were developed for lipids are listed in Table 2 and are shortly discussed in this section.

Table 2 All-atom (AA), united-atom (UA), and coarse-grained (CG) force fields for lipids.

Developer	Lipid FF	Resolution	Years published
CHARMM	CHARMM22 (C22)[67,68]	AA	1996/1997
	CHARMM27 (C27)[69]	AA	2000
	CHARMM27 (C27r)[70,71]	AA	2005
	CHARMM36 (C36)[72,73]	AA	2010
	CHARMM36 united atom FF (C36-UA)[74]	UA	2014
AMBER	GAFF[75,76]	AA	2007/2008
	Lipid11[77]	AA	2011
	Lipid14[78]	AA	2014
Jambeck & Lyubartsev	Stockholm (S)lipids[79,80]	AA	2012/2013
OPLS	OPLS-UA[81,82]	UA	1999/2000
	OPLS-AA[83]	AA	2014
GROMOS	GROMOS (Berger)[84]	AA	1997
	GROMOS (Chiu)[85]	UA	1999
	GROMOS (45A3)[86]	UA	2003
	GROMOS (53A6)[87]	UA	2004
	GROMOS (53A6-CPK)[88–90]	UA	2009/2011
	GROMOS54A7/54B7[91]	UA	2011
MARTINI	MARTINI[62,63]	CG	2004,2007
Shinoda, DeVane, & Klein	SDK[92,93]	CG	2007

2.1 Atomistic force fields for lipids

2.1.1 General description of classical force fields

MD simulations capture the different types of interactions defined by a potential energy function $U(r^N)$, called the force field. An MD simulation is based on Newton's second law of motion (Eq. 2) for a system of interacting particles, with the interactions being defined by $U(r^N)$, according to which velocities and positions are calculated for every time step. The parameters needed for the definition of $U(r^N)$ are derived from either quantum mechanical (QM) calculations or spectroscopic data. Eqs. (3) and (4) show the basic form of an AA-FF, which is divided into bonded and nonbonded interaction contributions and approximate a QM energy surface as a function of the atomic coordinates:

$$F = -\frac{\partial U(r^N)}{\partial r_{i,n}} = m_i \cdot \dot{v}_{i,n} \quad \text{with } i = 1,\ 2,\ 3, \ldots,\ N \text{ atoms};\ \ n = x,\ y,\ z;\ m = \text{mass} \tag{2}$$

$$\begin{aligned} U(r^N)_{\text{bonded}} = {} & \underbrace{\frac{k_{ij}}{2}(r_{ij} - r_{ij,0})^2}_{\text{bonds}} + \underbrace{\frac{k_{ijk}}{2}(\theta_{ijk} - \theta_{ijk,0})^2}_{\text{angles}} \\ & + \underbrace{\frac{V_n}{2}(1 + \cos(n\Phi_{ijkl} - \Phi_{ijkl,0}))}_{\text{torsion}} + \underbrace{\frac{k_{ijkl}}{2}(\Phi_{ijkl} - \Phi_{ijkl,0})^2}_{\text{improper torsion}} \end{aligned} \tag{3}$$

$$U(r^N)_{\text{nonbonded}} = \underbrace{4\varepsilon_{ij}\left[\left(\frac{\sigma_{ij}}{r_{ij}}\right)^{12} - \left(\frac{\sigma_{ij}}{r_{ij}}\right)^{6}\right]}_{\text{Lennard–Jones}} + \underbrace{\frac{1}{4\pi\varepsilon_0\varepsilon_r}\frac{q_i q_j}{r_{ij}}}_{\text{Coulomb}} \tag{4}$$

For computational efficiency, classical FFs employ some approximations in the treatment of bonded and nonbonded interactions. The bond lengths, angles, and improper torsion angles are often described by harmonic potentials, and for this reason, and unlike to QM descriptions, bond cleavage is not possible in classical MD simulations. With harmonic potentials even small deviations from the equilibrium values ($r_{ij,0}$, $\theta_{ijk,0}$, $\Phi_{ijkl,0}$) can cause considerable increases in the energy of the system, which also depend on the force constants (k_{ij}, k_{ijk}, k_{ijkl}). To model the rotation around bonds in accordance with thermodynamic data, a cosine function of the dihedral angle is typically used, where V_n is the force constant belonging to the torsion, $\Phi_{ijkl,0}$ is the angle where the potential passes through its minimum value, and n is the multiplicity, which indicates the number of minima as the bond is rotated through 360 degrees.

To describe van der Waals (vdW) and electrostatic interactions, the Lennard-Jones (LJ) 12/6 potential and Coulomb's law are employed, respectively. The attractive term of the LJ potential (r^{-6}) represents the component of the interactions based on London dispersion forces originating from induced dipole–dipole interactions. The repulsive term (r^{-12}) derives from the overlap of electron orbitals and describes the Pauli repulsion at short ranges, which can be efficiently calculated by squaring the attractive term. For each combination of atoms i and j, the well depth ε_{ij} and collision diameter σ_{ij} are required for the calculation of the LJ potential, in addition to the interatomic distance r_{ij}. The last important contribution to a FF is the electrostatic interaction between atoms, which is calculated using a Coulomb potential that depends on the distance r_{ij} and the partial charges of the atoms q_i and q_j as well as contains the permittivity of vacuum ε_0. With Eqs. (3) and (4), electrons are not explicitly considered. The atomic partial charges are derived from the electron distribution in a molecule as determined by QM calculations. In this approximation, the continuous function of the electron density becomes distributed point charges. Moreover, the partial charges, which are dependent on molecular conformations, are usually also fixed in most of the FFs. The interested reader is referred to chapter "Pairwise-additive and polarizable atomistic force fields for molecular dynamics simulations of proteins" by Lemkul of this book, which provides a more detailed discussion of classical FFs, including polarizable FFs that go beyond the fixed-charge approximation. In most MD simulations employing periodic boundary conditions, the particle-mesh Ewald (PME) method[94,95] is employed for treating the sum over electrostatic interactions, which are long-range interactions and thus require special care in periodic systems. In this method, the electrostatics interactions are divided into two parts: (1) a short-range contribution and (2) a long-range contribution. While the short-range contribution is calculated in real space in combination with a cutoff value (0.8–1.2 nm), the long-range contribution is computed using a Fourier transformation. This approach guarantees rapid convergence of the electrostatic energy calculation as compared with that of a direct summation.

The FF expression in Eqs. (3) and (4) was proven to be robust from thousands of applications in the past years, principally because it is sufficiently accurate in most cases for describing biomolecular interactions in a computationally efficient manner. The parameters needed as input for a FF are either derived from QM calculations or by empirical fitting to reproduce experimental observables, which are common strategies used for the parameterization of FFs. Moreover, atom types are defined to represent the different atoms and their chemical environment in the FF. As the different FFs usually followed diverse kinds of parameterization strategies, they usually employ slightly different atom types along with distinct values for the force constants as well as equilibrium distances and angles.

2.1.2 Experimental observables for the validation of lipid force fields

To study lipids and membrane proteins, various experimental techniques like X-ray, NMR, and different fluorescence spectroscopy methods were constantly developed and improved, with which characteristic properties of membranes can be determined. For instance, X-ray spectroscopy can be applied for the determination of membrane thicknesses, areas per lipid, electron density profiles, and lateral diffusion constants. To prove the phase state of a bilayer, structural and dynamic properties of the acyl chains are measured by NMR spectroscopy (e.g., area per lipid and order parameters). Moreover, various fluorescence spectroscopic techniques are available for determining the lateral diffusion of bilayer lipids, where the components of interest are marked with a fluorescent molecule for the measurements. Thus, besides expensive QM calculations experimental observables can be used to validate and improve lipid FFs. Here, we briefly discuss a set of membrane properties which are commonly used for benchmarking lipid FFs. Some of these observables are presented in Fig. 6. For more details on membrane properties used for the validation of FFs, we recommend the reviews by Poger et al.,[96] Leonard et al.,[97] and Moradi et al.[98]

2.1.2.1 Area per lipid

The first quality check of a lipid FF can be easily done by the calculation of A_L (Fig. 6A). It is related to the degree of fluidity of the membrane in a certain phase and, at the same time, a good indicator for whether equilibrium of an MD simulation has been reached. This common membrane parameter can be experimentally determined using X-ray or neutron scattering factors, volumetric methods, as well as NMR spectroscopy. From MD simulations, it can be calculated with Eq. (5):

$$A_L[nm^2] = \frac{B_x B_y}{n} \tag{5}$$

Here, the lateral dimensions B_x and B_y of the simulation box (unit cell) are along the x- and y-axes, respectively, while n is the number of lipids per leaflet. However, this equation can only be used for homogeneous membranes

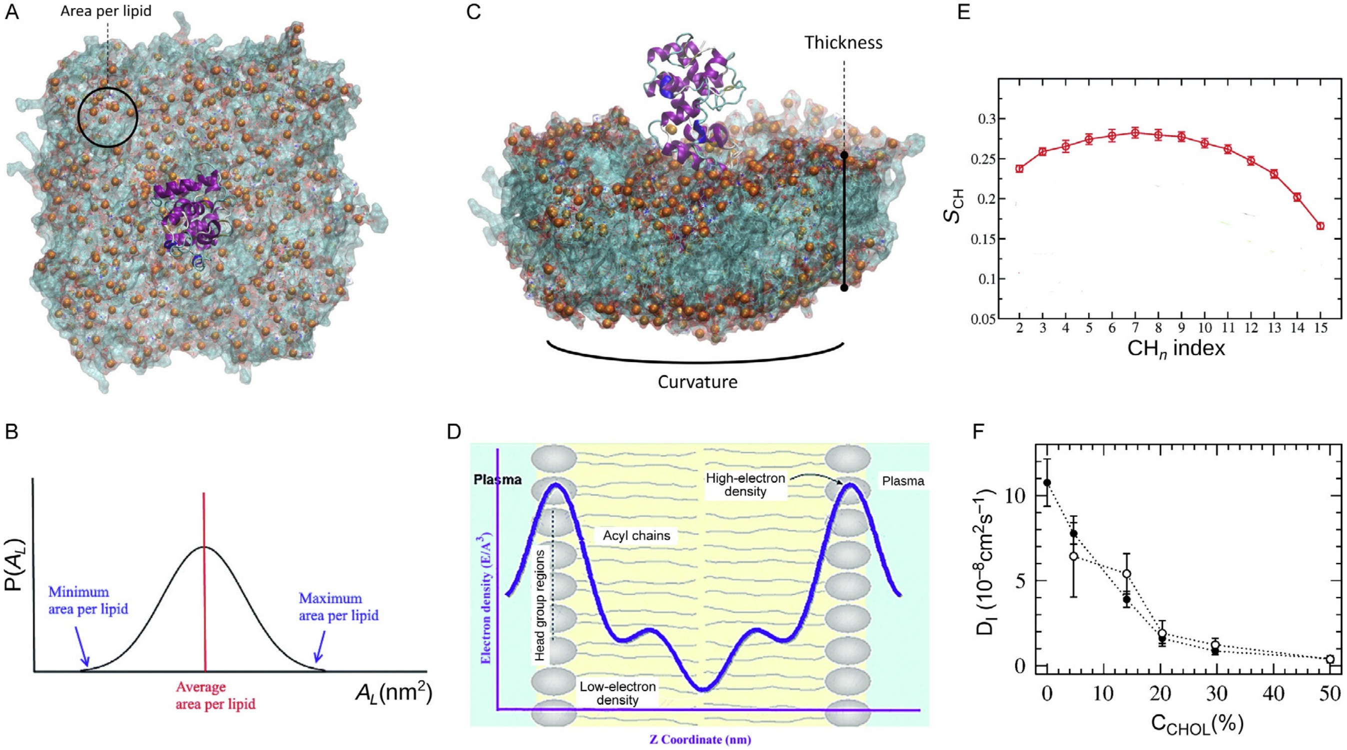

Fig. 6 See legend on next page.

with one lipid species. In the case of mixed bilayers, the membrane area must be partitioned into segments, for example by using two-dimensional Voronoi tessellation[100,101] or grid-based methods based on atomic vdW radii,[99,102] where the size difference between the different lipids and sterols are taken into account. A_L is tightly related to other membrane properties, like acyl chain ordering, compressibility, and molecular packaging. The time-average of A_L can be used to judge the equilibrium state of a bilayer during an MD simulation. An equilibrated bilayer shows only small fluctuations around an average value of A_L. However, this can only be assessed if the MD simulation is conducted in the NpT ensemble where the simulation box dimensions are allowed to fluctuate. In this ensemble, the number of molecules N, the pressure p, and the temperature T are constant, which is a more realistic ensemble than the NVT ensemble (where the volume V is kept constant) for comparison to experiments.[98] A higher value of A_L corresponds to a more disordered state, whereas low A_L values reflect highly packed lipids in the membrane. The probability distribution $p(A_L)$ for the area per lipid molecule can also be calculated (see Fig. 6B for an example distribution), allowing to determine the minimum, maximum and average values of A_L, which can be important for processes such as lateral diffusion.[98]

Fig. 6 Membrane properties commonly used for the validation of lipid force fields. (A) The average area per lipid (A_L) is computed by dividing the area of the *xy*-plane of the simulation box by the number of lipids per leaflet. (B) A representative probability distribution for the area per lipid. (C) The membrane thickness can determined by the mean distance between the head groups, marked by the positions of the phosphorus atoms (*orange*) of the outer and inner leaflet of the bilayer (D_{HH}). (D) An example for the electron density along the bilayer normal, from which the membrane thickness D_{HH} can be calculated. (E) A typical S_{CH} order parameter profile for a saturated acyl chain as obtained from an MD simulation. (F) Changes of lateral diffusion coefficient D_l of DPPC (•) and cholesterol (∘) molecules depending on cholesterol (CHOL) concentration. *Panels A and C: Adapted with permission from Goossens K, De Winter H. Molecular dynamics simulations of membrane proteins: an overview. J Chem Inf Model. 2018;58(11):2193–2202, 10.1021/acs.jcim.8b00639. Copyright 2018* American Chemical Society*; Panels B, D, and E: Adapted with permission from Moradi S, Nowroozi A, Shahlaei M. Shedding light on the structural properties of lipid bilayers using molecular dynamics simulation: a review study. RSC Adv. 2019;9(8):4644–4658, 10.1039/C8RA08441F. Copyright 2019* Royal Society of Chemistry (Creative Commons Attribution 3.0 Unported Licence)*; Panel F: Adapted with permission from Falck E, PatraM, Karttunen M, Hyvönen MT, Vattulainen I. Lessons of slicing membranes: interplay of packing, free area, and lateral diffusion in phospholipid/cholesterol bilayers. Biophys J. 2004;87(2):1076–1091, https://doi.org/10.1529/biophysj.104.041368. Copyright 2004* Elsevier.

The comparison of A_L obtained from MD simulations to experimental values can be difficult because this quantity cannot directly be determined by experimental techniques. Nonetheless, several methods exist to estimate A_L from experiments, for instance by using volumetric data and the electron density profiles of homogeneous bilayers,[103] or the lipid volume V_L and the Luzzati thickness D_B,[104] or the average NMR order parameter of carbon–deuterium bonds of the acyl chains.[105] Depending on which method and bilayer model were used, the resulting A_L values can significantly vary, which in turn generates some uncertainty with regard to the true value of A_L for a lipid bilayer in a given phase. Moreover, the determination of A_L is affected by thermal fluctuations in the lateral and transverse directions of lipid bilayers. In the last decades, it occurred that different A_L values for the same kind of bilayer were obtained with the same experimental technique or calculated by the same researcher group. Nevertheless, A_L determined from simulation studies using the same FF usually result in very similar values as opposed to those derived from experiments, which can be explained by the fact that the FFs were parameterized to produce a certain A_L value (see Table 1 in Ref. 96). It should further be considered that undulations or fluctuations in the lipid bilayer structure, which may result from insufficient sampling or from simulations artifacts (e.g., due to finite system size or periodic boundary conditions) may also cause uncertainties in A_L. As a consequence, A_L alone is not sufficient to evaluate the quality of a lipid FF or to assess the degree of fluidity of a lipid bilayer; it should be considered together with the electron density profile across the bilayer and the bilayer thickness for judging the phase state of a membrane.

2.1.2.2 Membrane thickness and electron density profile

While A_L facilitates information about the lateral structure of a lipid bilayer, the membrane thickness provides information on the orthogonal direction (Fig. 6C). Generally, the membrane thickness is in the range of 3–5 nm. There are three slightly different quantities commonly used to represent the thickness of a membrane: (1) the head-to-head thickness (D_{HH}) derived from the distance between the averaged z-positions of the phosphorus atoms of opposing leaflets, (2) the bilayer thickness obtained from the water density probability at half-maximum (D_B), and (3) the hydrophobic thickness ($2D_C$) calculated from the half-maximum of the density of the atoms in the hydrophobic acyl chains. The quantity D_{HH} can be determined by X-ray scattering as the distance between the two maxima of the electron density profile of the lipid bilayer (see Fig. 6D). With this approach, the accuracy of D_{HH} is limited by the Fourier truncation error. For measuring D_B, neutron scattering experiments can be applied by making use of the high contrast between the protiated lipid and deuterated water accurately defining the bilayer thickness, which is correlated to the penetration of the lipid bilayer by water molecules. Both D_{HH} and D_B can be easily determined from MD simulations. D_{HH} is usually computed as the average distance between the phosphate planes of the two leaflets. D_B is calculated using Eq. (6) (with the bilayer normal in z-direction and d being the simulation box length in that direction) as the distance between the points along the membrane normal, where the water density probability $p_w(z)$ is one half:

$$D_B[nm] = d - \int_{-d/2}^{d/2} p_w(z)dz \tag{6}$$

The third measure for the membrane thickness, $2D_C$, refers to the thickness of the hydrophobic core of a bilayer[96] and is determined based on the positions of the CH_2 groups in each leaflet of a lipid bilayer. These positions can be derived from X-ray or neutron scattering data, or from NMR making use of the carbon-deuterium bond order parameters in the acyl chain. However, $2D_C$ is highly dependent on the underlying approximations (e.g., for the volume of a methylene group or the estimate for the average tilt of the acyl chains with respect to the bilayer normal), thus the outcomes can significantly differ and are only comparable to the values determined from MD simulations as long as the same assumptions are employed.[96] Together with A_L, the membrane thickness allows one to assess the state the bilayer in question. In fact, a decrease in A_L almost always relates to an increase in the lipid bilayer thickness, which is further accompanied by a stronger ordering of the acyl chains in the membrane.

An electron density corresponds to the probability of the electrons being present at a specific location. With the help of X-ray crystallography, the electron density of a membrane can be experimentally estimated. In MD simulations, where electrons are not explicitly considered, the time-averaged positions of electrons can be inferred with good accuracy from the atomic positions. Fig. 6D shows a typical electron density profile across a membrane, which is characterized by following observations: The profile exhibits a global minimum in the middle of the bilayer (near the terminal CH_3 groups of the acyl chains), two maxima corresponding to the positions of the head groups (phosphate groups) in each leaflet, and a local minimum reflecting the water layer outside the membrane. The thickness D_{HH} is defined as the distance between the two maxima of the electron density profile, which changes upon the insertion or interaction of a molecule with a membrane. In the case of mixed membranes involving cholesterol, the peaks of the phosphate groups are slightly shifted depending on the cholesterol concentration, whereas the rest of the profile exhibits no significant changes.[98] The electron density profile is symmetric if the two leaflets have the same composition and when the bilayer is in its equilibrium state. The main aspects of an electron density profile are required to be reproduced by a FF, like the overall profile shape and the position of the peaks corresponding to specific groups of atoms (e.g., head groups, glycerols, carbonyls, methylenes in the hydrocarbon chains). In addition, these profiles can be also calculated from the mass density across the bilayer, which shows how the mass is distributed along the membrane z-axis and exhibits the same shape as the electron density distribution. In the case of a typical hydrated membrane system, the mass density is high at the beginning of the lipid chain, similar to the mass density of several soft polymers (0.9–1.3 g cm^{-3}). At carbon position 9, the density is reduced to the one of liquid hexadecane (0.753 g cm^{-3}) and it is considerably lower in the middle of the membrane (0.60 g cm^{-3}). This shows that the acyl chain region of the bilayer in the liquid crystalline phase is far from being homogeneous.

2.1.2.3 Acyl chain order parameters

Lipid bilayers can be characterized by their degree of orientational lipid order. Experimentally, the measurement of the carbon–deuterium (or hydrogen) bond order parameters S_{CD} (S_{CH}) can be accomplished by NMR spectroscopy using ^{2}H (deuterium, D) selectively labeled lipids. More recently also ^{1}H–^{13}C labeled lipids have been employed. The order parameters S_{CD} depend on a combination of local, molecular, and collective motions as well as static disorder, and the decomposition the overall value into individual contributions is difficult. ^{2}H NMR spectroscopy has been widely applied to determine the S_{CD} values of the acyl chains of GPLs, which have become an important target property to validate lipid FFs. The order parameter S_{CD} of a C–D bond of an acyl chain measured by NMR can be directly compared with values for S_{CH} calculated from a simulation using the following equation:

$$S_{\mathrm{CH}} = \frac{1}{2}\langle 3\cos^{2}(\theta_{z}) - 1\rangle \tag{7}$$

Here, θ_z is the (time dependent) angle between the C–H bond vector and the bilayer normal (experimentally the magnetic field or z-axis of the simulation box). The angular brackets denote a time and ensemble average. The order parameter adopts values between -0.5 and 1, where a value of -0.5 means that the two vectors are perpendicular to each other, while a value of 1 implies that the two vectors are parallel. The order parameters do not only depend on the orientation, but also (dis)order of the system. For instance, $S_{\mathrm{CH}} = 0$ can either arise from C–H bonds isotropically disordered with respect to the bilayer normal, or all corresponding bond vectors are perfectly oriented at the magic angle relative to the bilayer normal (that is 54.7 degrees, corresponding to $\cos^2(\theta_z) = 1/3$).

The general focus is on the values of S_{CD} as a function of the position of the carbon atom in an acyl chain, but S_{CD} (or S_{CH} in simulations) can be also determined for other lipid moieties, like the glycerol or the head group. The S_{CH} order parameter profiles that are obtained for saturated acyl chains look qualitatively similar to the one shown in Fig. 6E. It is characterized by some degree of disorder in the alkyl groups close to the water interface, which is followed by an increase in order with a order maximum at about the middle of the acyl chains. Toward the center of the membrane, corresponding to increasing C atom number positions along the acyl chain, the disorder increases (i.e., decreasing S_{CH}). This results from the greater degree of conformational flexibility of the acyl chains in the core region of a membrane. Furthermore, the length of an acyl chain influences the S_{CD} values, with longer chains reducing the order parameter. Similarly, temperature affects S_{CH}, with lower temperatures implying an increase in S_{CH} due to the closer packing of the lipids.

Differences between the experimental and calculated order parameters can be a result of incomplete sampling during the MD simulation in question. Moreover, membrane undulations and fluctuations in both experiments and simulations can contribute to the value of S_{CD} (S_{CH}). In simulations, large enough lipid bilayers are required to limit the artifacts due to a finite system size and periodic boundary conditions. If a UA-FF was used during an MD simulation, the C–H bond vector needs to be reconstructed. This is done based on the positions of three successive CH_2 groups and assuming tetrahedral geometry for the central C atom. It should be noted that this calculation only holds when the hydrogen atoms of a methylene group are equivalent and, more importantly, it is not valid around unsaturated bonds due to their different geometry.

2.1.2.4 Membrane area compressibility

Compressibility, which describes the relative volume change of a given substance in response to stress, is extensively studied for lipid bilayers. Membrane area compressibility, in particular, indicates the resistance of a lipid bilayer to isotropic area dilation and is defined by an area compressibility modulus K_A:

$$K_A[Nm^{-1}] = A\left(\frac{\partial \gamma}{\partial A}\right)_T = \frac{Ak_\mathrm{B}T}{\sigma_A^2} = \frac{A_L k_\mathrm{B}T}{N_l \sigma_A^2} \tag{8}$$

Here, γ represents surface tension, A is the average total area, k_B is the Boltzmann constant, T is the temperature, A_L is the area per lipid (see above), N_l is the number of lipid molecules, and σ_A^2 is the mean square fluctuation of A_L. As the area compressibility modulus is inversely proportional to the area fluctuations, K_A is a reliable parameter to estimate the rigidity of a lipid bilayer.

2.1.2.5 Lateral diffusion coefficient

In the last several years, lateral diffusion processes in biological membranes have been studied with experimental and computational methods, but the underlying molecular mechanism is still unknown. The lateral diffusion of lipids and proteins depends on the neighboring molecules. It is a fast and spontaneous movement relative to translational motions between the two leaflets, where special membrane proteins, called flippases and floppases, are required for this lipid transport. The experimental techniques for determining lateral diffusion constants range from fluorescence techniques (e.g., FRAP, FRET and fluorescence correlation spectroscopy, FCS) to EPR and NMR spectroscopy (e.g., ^{1}H, ^{2}H, ^{19}F, and ^{31}P). As for other membrane observables, the resulting values for the lateral diffusion constants can vary even of one uses the same method, as it is sensitive to experimental conditions, like the temperature, hydration content, pH, ionic strength and experimental setup.[96] Furthermore, EPR and fluorescence methods have to use labeling molecules (e.g., spin labels or fluorophores) for tracking the lipid diffusion. Here, the measured lateral diffusion coefficient derives from the labeling molecules instead from the lipid itself, which is not negligible in some cases depending on the type of labeling, its concentration, and whether the measurement was done in a bilayer or monolayer.[96] Neutron scattering can be used for fast, short-range diffusion (motions for 0.1–10 nm in $<$1 ns), while the other techniques sample slower, medium-to-long-range diffusion processes (motions of $>$0.1 μm on the ns-to-ms timescale).[106]

For the movement of lipids and other membrane molecules during MD simulations, the Einstein relation based on the average lateral mean squared displacement (MSD) $\langle [\Delta r(t)]^2 \rangle$ can be used for computing the lateral diffusion constant by applying the following equation:

$$D_l[cm^2 s^{-1}] = \frac{1}{2n_f} \lim_{t\to\infty} \frac{\langle [\Delta r(t)]^2 \rangle}{t} \tag{9}$$

Here, the n_f denotes as number of translational degrees of freedom ($n_f = 2$ for an in-plane motion or in the xy-plane) and $r(t)$ is the center of mass (COM) position of the molecule under study at time t. In general, the MSD is calculated as average over all lipids. As for experimental methods, the resulting lateral diffusion constants can vary as they depend on the applied FF, system size, the cutoff scheme for the truncation of long-range electrostatics, the time step, and the frequency used to update the nonbonded pair list. Thus, the comparison between the results from several studies is difficult; Table 2 in Ref. 96 lists some lateral diffusion constants obtained from simulations. Flack et al.[99] studied the influence of cholesterol on the lateral diffusion of lipids using 100 ns MD simulations of a DPPC bilayer with varying amounts of cholesterol, which demonstrated that the lateral diffusion coefficients of both DPPC and cholesterol decreased with increasing concentrations of cholesterol (see Fig. 6F). In general, the lateral diffusion can be evaluated only in the liquid crystal state.[98]

2.1.3 Comparison of the atomistic lipid force fields

In chapter "Pairwise-additive and polarizable atomistic force fields for molecular dynamics simulations of proteins" by Lemkul of this book, the historical development of the different protein FFs was described in detail. Thus, we concentrate here to give an overview about the FFs that are available for studying protein–membrane systems, including to list their advantages and shortcomings.

2.1.3.1 CHARMM

The CHARMM (Chemistry at Harvard Macromolecular Mechanics) all-atom force field originates from the lab of Martin Karplus at Harvard University and has an active community who developed a huge set of FFs with a focus on biomolecules, such as lipids,[72,73] carbohydrates,[107–110] nucleic acids,[111,112] and proteins.[113,114] Additionally, a general force field, known as the CHARMM General FF (CGenFF)[115] allows simulations with other biomolecules and drugs that conform to the general parameterization scheme applied in CHARMM. In addition to the common FF terms (see Eqs. 3 and 4), the intramolecular interactions include the so-called Urey–Bradley term for covalent angles, which is a cross term connecting the motions of bond angles and lengths:

$$U(r,\theta) = \underbrace{k_{ub,i(i+2)}\left(r_{i(i+2)} - r_{i(i+2),0}\right)^2}_{\text{Urey-Bradley}} \tag{10}$$

The Urey–Bradley term with force constant $k_{ub,i(i+2)}$ applies to atoms i and $i + 2$ connected by two bonds. However, this term is only used for older CHARMM parameters but not for newer ones. The parameterization strategy of CHARMM is based on fitting to reproduce experimental and ab initio QM data at the HF/6-31(g) level of theory of small model compounds (e.g., alkanes for the acyl chain) that are transferable to larger molecules (e.g., to lipids) with some further optimization. Furthermore, it is recommended to use the modified TIP3P water model—even though better water models like TIP4P are available—when employing the CHARMM pairwise additive FF,[97] since the parameters for interaction of biomolecules with water were optimized for this water model and the usage of another water model could lead to imbalances in the electrostatic and solvation energies. Another peculiarity of CHARMM is that this FF applies force-based cutoffs in which the force is smoothed to zero at a cutoff of 1–1.2 nm, affecting the overall potential. Therefore, this cutoff value must be used when using CHARMM. Moreover, the nonbonded interactions of atoms that are separated by four bonds, so-called 1–4 interactions are not scaled, which in turn implies that the dihedral potential parameters depend on the electrostatic and the LJ parameters. Thus, optimization of these coupled parameters is typically carried out in an iterative fashion, in which the dihedral parameters are fitted to the obtained LJ and electrostatics parameters per iteration step.

The first CHARMM parameters for lipids were published with the CHARMM22 parameter set (denoted as C22)[68] by the Pastor group. They were updated with the release of the CHARMM27 parameter set (C27),[69] which was the first widely available and thus used AA-FF for lipids. For a DPPC lipid bilayer C27 produced a good agreement with experimental deuterium NMR order parameters (S_{CD}) for the acyl chains and the electron density profiles.[69] However, further investigations revealed non-negligible disagreements with experiment (e.g., for the A_L value)[116] as well as for dynamical properties obtained from NMR relaxation times, indicating that probably the C27 torsional barriers were too high.[117] For fully saturated lipids it was shown that the bilayers often exhibited a gel phase at conditions corresponding to liquid crystalline phases. To circumvent this problem, many MD simulations with C27 were performed in the NVT ensemble[118] with a fixed A_L value or under nonzero surface tension,[119] as under these conditions the *trans* conformation of the acyl chains is more preferred than the *gauche* conformations.[120] There was an update to the C27 parameter set[70,71] (called C27r), but the phase state problem of the lipid bilayers was still present and also the correct A_L could not be reproduced with MD simulations at zero surface tension (NpT ensemble).[70,121]

Five years later, the CHARMM36 parameter set (C36) was published[73] by Klauda et al. and verified with MD simulations of bilayers involving six saturated and monounsaturated lipids (DLPC–12:0,12:0; DMPC–14:0,14:0; DPPC–16:0,16:0; DOPC–18:1,18:1; POPC–16:0,18:1; POPE–16:0,18:1). Partial atom charges and torsion potentials were reparameterized by using ab initio computations, as well as revision of some LJ parameters for matching with semiempirical QM results of small bilayer assemblies, solvation free energies, and S_{CD} near the membrane interfacial region. Moreover, the description of the lipid head group structure and dynamics was improved in the same manner like as in the work by Sonne et al.[122] and compared to NMR data. Properties as average A_L at zero tension ($\gamma = 0$), structure factors, dipole electrostatic potential indicated good agreement with experiment and better than with the C27r parameter set.[73] The key improvement was that the C36 lipid FF accurately matched the X-ray and neutron form factors, bilayer and hydrocarbon thickness as well as S_{CD} of POPC and POPE bilayers. To sum up, the C36 FF allows to accurately represent bilayer properties of fully saturated and monounsaturated lipid molecules in the NpT ensemble.[73] In the last years, different kind of lipids were added to C36 using the same parameter strategy, such as a variety of acyl chains (PUFAs,[123] branched[124] chains and chains with cyclic moieties[125]) and head groups (PA, PG, PI, and PS),[72,126,127] sterols (cholesterol,[128] ergosterol[129] and plant sterols[130]), sphingolipids[131] and ceramides[132] as well as glycolipids[133] and LPS[126,134] making use of the CHARMM carbohydrate FF.

To accelerate the sampling during an MD simulation, the C36-UA FF was developed based on the C36-AA lipid parameters,[74] in which the acyl chains have the UA representation, while the head groups are described in an explicit manner. It performs well for lipid membranes and micelle formation of a surfactant. MD simulations of DMPC, DPPC, POPC, DOPC, and DMPC/CHOL bilayers produced good values for the A_L, X-ray and neutron form factors, and acyl chain order parameters S_{CD}.[74] However, the Klauda lab reported general issues (unpublished data) with too high values for the density of alkanes and too small values for the hydrophobic bilayer thickness; furthermore the head groups needed additional parameterization.[97]

2.1.3.2 AMBER

For a long time, no proper parameters for lipids were available for the AMBER FF (Assisted Model Building and Energy Refinement), although some attempts were done to simulate bilayers. However, the A_L values for DMPC and DOPC bilayers modeled with the Generalized Amber Force Field (GAFF)[135] with the extension to lipids[75] were underestimated[76] compared to the experimental values. A certain surface tension had to be applied to obtain the correct lipid area. In contrast to CHARMM, in AMBER the 1–4 LJ and Coulomb interactions are scaled by a factor of 0.833; moreover, the restricted electrostatic potential (RESP) method[136,137] is used for the calculation of the partial charges of whole molecules. With the goal to develop a lipid FF that is comparable to C36 FF, the Lipid11 FF[77] was developed, in which a careful reparameterization of LJ and charge values to improve modeling of lipid bilayers was undertaken. Bilayers of DOPC, POPE, and POPC were tested, but again a surface tension term had to be applied to obtain good agreement with experimental scattering profiles and NMR S_{CD} data. In an alternative approach, modifications to the GAFF LJ parameters for the simulation of acyl chains were made to generate accurate and stable simulations of pure lipid bilayers of DLPC, DMPC, DPPC, DOPC, POPC, and POPE, yielding the GAFFlipid FF.[138] For all six lipid types tested it achieved a higher level of agreement between simulation and experiment for numerous structural properties, like A_L, volume per lipid, bilayer thickness, order parameter, and head group hydration. Based on the GAFFlipid parameters, the Lipid11 FF was updated yielding the current standard AMBER lipid FF, named Lipid14,[78] which allows the simulation of a number of lipids without an additional surface tension term. As for C36, the Lipid14 FF has been tested by simulating bilayers of six different lipid types (DLPC, DMPC, DPPC, DOPC, POPC, and POPE) and no longer requires a surface tension to be applied for keeping the lipid area constant. Membrane properties, such as A_L, isothermal compressibility, bilayer thickness, and NMR S_{CD} parameters, favorably agree with experiment, reaching the same level of accuracy as C36. The only shortcoming is that S_{CD} for the head group and order splitting for carbon-2 on the *sn*-2 chain were not tested. Lipid14, which works well with the tensionless *NpT* ensemble, can be combined with the AMBER FFs for proteins, nucleic acids, carbohydrates,[139] and small molecules, and was extended to mixed membranes including cholesterol.[140] There is also an update to the Lipid17 FF for anionic head groups and polyunsaturated acyl chains[141]; however, it has not been applied yet, leaving it open how well it performs.

2.1.3.3 Slipids

Around the same time when the C27r FF was updated to the C36 FF and based on the suggestions in these papers,[120,122] a new AA-FF named Slipids (Stockholm lipids) for fully saturated phospholipids[142] and monounsaturated lipids[79] was published, which was extended a year later to include the lipid head groups PG, PE, PS, and SM as well as cholesterol.[80] As starting point the recent C36 parameter set was used and following optimizations performed: (1) The partial charges, LJ and torsion angle parameters of all lipid tails were updated by using high-level ab initio calculations, whereas the parameters for covalent bonds and angles along with some of the torsion angle and LJ parameters were used from C36. (2) The head group parameters were improved using QM calculations at a low level of theory and the water dielectric constant readjusted using the TIP3P water model. (3) Scaling factors for the LJ/Coulomb parameters for the 1–4 interactions were introduced, using a value of 0.5 between hydrogens of the lipid carbon chain and varying values for the rest, which is based on AMBER FFs with a scaling factor of 0.833. (4) The RESP method[136,137] was applied to determine the partial charges, as done for the AMBER parameters. For testing, the resulting Slipids FF was applied to DLPC, DMPC, DPPC, POPC, SOPC, POPE, and DOPE bilayers[79,142] as well as to mixed membranes with cholesterol.[80] A good agreement to the experimental values of many membrane observables, like A_L, NMR order parameters and structure factors was obtained. The most important aspect is that the parameters are able to reproduce structural properties of single and double component membranes without employing a surface tension, therefore, it allows to study complex systems containing many different lipids and proteins in a fully atomistic resolution in the *NpT* ensemble. Due to the parameterization close to the AMBER strategy, it is compatible with the AMBER FFs for proteins, which was tested for a WALP23 peptide (modeled by three versions of the AMBER protein FF),[79] and for drug-related compounds in combination with lipid bilayers.[143,144]

2.1.3.4 OPLS-AA

The development of the OPLS-AA FF (Optimized Parameters for Liquid Simulations All Atom) by Jorgensen et al. was mainly done for organic liquids to reproduce the experimental values for thermodynamic and partitioning properties.[145,146] Quite recently, lipids were parameterized[83] along with other biomolecules[147–149] for this OPLS-AA FF. The partial charges were obtained with the similar route as followed for AMBER FFs and the optimization of dihedral angles was accomplished as for the C36 lipid FF, using small molecules to represent the PC lipid head groups. Only a single 200 ns MD simulation of a DPPC bilayer at 323 K was performed for the parameterization that showed good agreement with experimental S_{CD} and X-ray form factors.[83] Furthermore, the inclusion of the dihedral optimization for the lipid head groups reproduced similar values as NMR spectroscopy for this region of the lipid. Since then, the OPLS-AA FF was extended to lipids with chain unsaturation,[150] cholesterol,[151] ether linkages,[152] PE,[152,152a] PI,[152b] PS, and SM[152a] with different saturation/unsaturation levels and acyl tail lengths as well as GM1.[152c] Apart from these, POPC oxidized lipids such as 1-palmitoyl-2-(9′-oxo-nonanoyl)-sn-glycero-3-phosphocholine (PoxnoPC) and 1-palmitoyl-2-azelaoyl-sn-glycero-3-phosphocholine (PazePC) were also paramterized for study with OPLS-AA FF.[152d] However, further developments are necessary to obtain the lipid diversity available in C36 and the AMBER FFs. There is also an OPLS-UA FF, which was initially developed for DMPC and resulted in good agreement with the experimental value of A_L at 303 K.[81] It was extended to cholesterol[82] and epicholesterol,[153] but lacks further lipids necessary to simulate more realistic biological membranes.

2.1.3.5 GROMOS

(Groningen molecular simulation package)[86] uses the UA approach to represent each nonpolar CH, CH_2, and CH_3 group of hydrocarbons as a single particle, thus reaching an about threefold acceleration in comparison to AA FFs. The main objective in the development of GROMOS FFs is the reproduction of thermodynamic properties of model compounds (small molecules representing biomolecular fragments), like enthalpies and free energies of solvation in polar and apolar environments. Therefore it became a popular choice for the simulation of membrane proteins. GROMOS FFs applied for bilayer simulations can be split into two groups: (1) using the original GROMOS nonbonded parameters (e.g., 45A3,[86] G53A,[87] and G54A[154] parameter sets) and (2) the Berger modification[84] (also called Berger lipid FF), in which the Ryckaert–Bellemans potential was implemented for describing torsion rotations of the hydrocarbon chains of lipids. Several studies with the 45A3 parameter set (e.g., DPPC)[86] and Berger lipids (e.g., DOPC and DMPC)[116,119,155,156] revealed that the GROMOS FF did not properly reproduce a number of experimental properties, like the electron density profile, structure factor, and A_L. Moreover, with GROMOS, MD simulations cannot produce the proper gel phase of bilayers at temperatures below the melting point.[157] Based on further ab initio computations and fitting to thermodynamical data for liquid alkanes, the 43A1-S3 parameter set[158] showed better results for A_L than the previous versions and was updated to the G53A6 parameter set,[87] which exhibited very good agreement with experimental membrane properties of DPPC bilayers (A_L and volume per lipid, electron density profiles, bilayer thickness and hydration, S_{CD} of acyl chains). Furthermore, it reproduces the structural and hydration values of common GPLs of varying length and degree of unsaturation of the acyl chains (e.g., DLPC, DMPC, DOPC, and POPC) in a liquid crystal phase.[159] In addition, the G53A6 parameter set can be applied for the MD simulation of PC bilayers in the liquid crystalline phase. The G53A6 FF was further improved with the Kukol parameters[88] and the parameters by Piggot[89] (known as the CKP parameter set) for saturated and unsaturated PC and PG lipids and later also for PG, PE, and CL.[90] Although it is known that the Berger parameters are not the best choice for reproduction of experimental lipid properties, they are still used in many recent papers in combination with older versions of the GROMOS FF or AMBER FFs. Finally, the last update is the G54A7 parameter set for a number of lipid types.[91] In addition to the G53A6 FF, the G54A7 parameters include bacterial lipids with branched fatty acids in their lipid chains,[160] with cyclopropane moieties,[161] as well as hopanoids and sterols.[162] However, the number of different lipids that has been tested for this FF is rather limited.

2.1.4 Limitations of atomistic lipid force fields

In spite of great hardware and software developments, which facilitated MD simulations of large protein–membrane systems on the microsecond timescale and with atomistic resolution, the sampling of protein conformations can become problematic due to high-energy barriers separating the different protein states. Enhanced sampling techniques, such as metadynamics or umbrella sampling may provide a means to overcome free energy barriers during MD sampling; they are discussed in detail in chapter "Enhanced sampling and free energy calculations for protein simulations" by Liao of this book. However, these methods are not often applied on lipid bilayers, except for surface tension replica exchange[163] adaptive biasing force[164] and metadynamics.[165] Another approach is given by reducing the degrees of freedom that need to be sampled, leading to CG-FFs, which allow to simulate larger systems for longer times compared to AA-MD simulations and are discussed in more detail in the next section. Before, we briefly introduce the highly mobile membrane mimetic (HMMM) model, which is not a CG model but nonetheless accelerates lipid dynamics by modeling the acyl tails in the membrane center as a fluid organic solvent.

2.1.4.1 The HMMM model

At physiological temperatures, the lateral diffusion of lipids in a membrane is typically on the order of 10^{-8} cm^2 s^{-1}, which can prevent the membrane association of peripheral proteins or spontaneous lipid mixing to occur in AA-MD simulations given their typical timescale of hundreds of nanoseconds. It would require at least orders of magnitude greater sampling to reach diffusive equilibration. A workaround to this problem was presented by Ohkubo et al. with the development of the HMMM model,[64] which uses an organic solvent layer to describe the hydrophobic core of the membrane while maintaining an atomic description of the lipid head groups and shortened GPL acyl tails. This leads to an acceleration of the lipid diffusion without sacrificing the atomistic level of detail for the head groups, which are essential for protein–membrane interactions. In the HMMM model, the GPLs are truncated in the acyl chains. The resulting space in the membrane core is then filled with an organic solvent, most often 1,1-dichloroethane (DCLE) to reproduce the characteristics of the hydrophobic core of lipid bilayer (Fig. 5B, left panel).

In the original HMMM model study,[64] the authors demonstrated the efficiency and robustness of their approach. They used the CHARMM36 General FF parameters[115] to perform the simulations. First, they demonstrated that the HMMM model is indeed able to form and maintain bilayers. To this end, an initial biphasic solvent box, containing water and DCLE was set up, and 54 divalerylphosphatidylserine (DVPS, 5:0,5:0) molecules, which were chosen to present the head groups and shortened acyl chains of PS lipids in this particular HMMM model, equally distributed in that box. A fully formed bilayer formed within 20 ns of MD and was stable in the remainder of that 40 ns simulation. Comparison to a DOPS (18:1,18:1) membrane simulated under the same conditions confirmed that the HMMM model was able to reproduce the atomic distribution of various chemical groups in the membrane, in particular in the head group region that is often essential for protein binding. Furthermore, the extent of hydration and the degree of counterion penetration was similar compared to the full-membrane system. As a second test, a set of five simulations were performed to calculate the lateral diffusion constant of the lipids in the HMMM model and its dependence on different configurations. The lateral diffusion constants of the DVPS molecules were found in the range of 10^{-5}–10^{-6} cm^2 s^{-1}, presenting an increase of one to two orders of magnitude in comparison to the full-membrane system. This improvement enables more efficient sampling of head group configurations, e.g., during the binding and insertion of peripheral proteins. To test this, the authors employed the HMMM model for studying the membrane association of the coagulation Factor VII GLA domain, which is involved in the membrane binding of different peripheral proteins. The GLA domain is a common membrane-anchoring domain in coagulation proteins and predominantly binds to PS-rich regions of the cellular membrane, resulting in an increase of the catalytic activity of these proteins. At the time of the original HMMM model study, classical AA-MD simulations failed to reproduce the association of the GLA domain to membranes, while this event was sampled within 50 ns of MD simulations using a PS-HMMM model.[166]

Since its publication, the HMMM model has been applied to various membrane-associated proteins, including coagulation factor GLA domains,[167] cytochrome P450,[168] and TM domains.[169] Furthermore, the free energies from AA and CG simulations for the partitioning of amino acids into the interfacial membrane region could be reproduced by the HMMM model.[170] The application of the HMMM model to study membrane association of amyloid peptides[171,172] is discussed in Section 4.2.1. Despite its various successful applications, it should be noted that the HMMM model also exhibits several limits. First, it cannot be applied for accurately representing the energetics and processes at the membrane core because the behavior of DCLE significantly differs from that of acyl chains in the lipid bilayer core.[170,173] Second, simulations of TM proteins with the HMMM model are still difficult as the DCLE solvent destabilizes multihelix TM domains in the core region.[173] Finally, it still remains to be shown whether the HMMM model can also reproduce the characteristics of membranes involving other lipids, such as sphingolipids and sterols.

2.2 Coarse-grained force fields for lipids

To fully understand membrane systems, it is desirable for MD simulations to be able to study relevant timescales, which in practicality are beyond what most existing resources can currently handle at the atomistic level. For instance, subcellular processes involving lipid bilayers such as domain formation, spontaneous lipid aggregation into full micellar and vesicular structures, particle insertion, and other dynamical phenomena occurring at large time and length scales require CG models.[74,174,175]

In CG models, a certain number of atoms whose physical and chemical properties can be averaged to achieve the FF design philosophy is chosen and treated as a single particle (Fig. 7A). This reduces the degrees of freedom, and thus the computational effort for the integration of Newton's equation of motion (Eq. 2). With this, sampling larger timescales becomes increasingly possible, while bigger lipid systems (both homogeneous and mixed) that are closer to realistic biological membranes can be studied. CG-based MD simulations can more effectively sample conformational landscapes of molecular systems, in effect because they transform the typically rugged energy landscape into a much smoother surface; the level of *smoothness* depends on the level of coarse-graining (Fig. 7B). The coarser a model is, the smoother is the underlying energy landscape and the more efficiently can conformational and energy states be simulated. By using smooth potentials, most currently available CG models are able to employ integration steps much greater than the 2 fs time steps commonly employed in all-atom simulations. For instance, in MD simulations using the MARTINI FF time steps of 10–20 fs are typically used. However, this scale up in conformational sampling efficiency comes with a cost: atomistic resolution is lost and so is information about properties deriving directly from individual atomic constitution.

CG-FFs stand between AA-FFs and continuum models with respect to the level of resolution, speed of sampling the phase space, level of approximation, as well as properties that can be investigated. There is always a trade-off in resolution associated with the different scales of simulation, from QM to AA- and CG-MD, and to continuum models. The trade-off relates to different degrees of neglect in the explicit treatment of electronic (AA) and atomic properties (CG), and in each case it is deliberately accommodated in order to achieve more extensive sampling of time- and length-scales relevant to some biomolecular properties. And in the case of CG models of membrane systems, the founding philosophy of a particular model dictates both resolution and extent of sampling. Each CG model represents an attempt to address specific aspects of the membrane and it is important for the user to decide which CG model has been designed to provide answers to the kind of research questions that are being asked. Parameter sets available for most CG models are either the result of a top-down approach, a bottom-up approach, or a mix of both. In the top-down approach, the goal

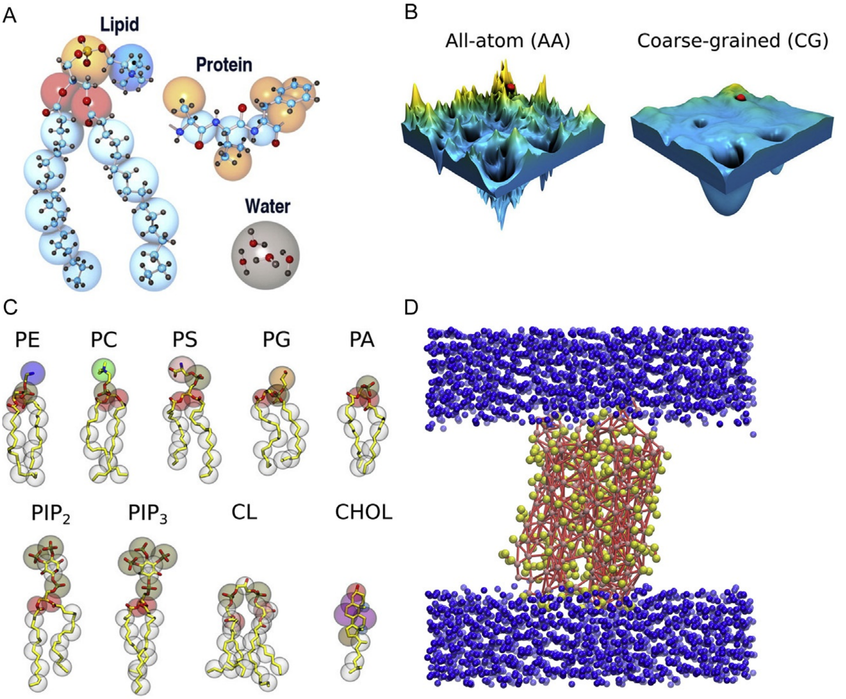

Fig. 7 MARTINI mapping and elastic network approach for proteins. (A) The AA-to-CG mapping underlying the MARTINI FF. *Balls* and *sticks* are used for the AA representation, while the CG beads are shown as large spheres. Each bead merges four heavy atoms with the associated hydrogen atoms. The mapping is exemplarily shown for a lipid (PSPC or POPC), a fragment of a protein chain, and a water molecule. (B) Comparison between AA and CG energy landscapes. Coarse-graining smoothens the energy landscape, facilitating a more efficient exploration of the energy landscape in an MD simulation. (C) The AA-to-CG mapping for common lipids in MARTINI, overlaid on the corresponding AA structures (hydrogen atoms are removed for clarity). The CG beads are displayed as transparent vdW spheres. (D) Schematic representation of the dummy bonds (*red*) in the elastic network approach used in MARTINI to keep the secondary structure of a protein (displayed with *yellow CG beads*) in its initial assignment. The water beads are shown as *blue spheres*, while the membrane bilayer is not shown for clarity. *Panels A and B: Reprinted with permission from Kmiecik S, Gront D, Kolinski M, Wieteska L, Dawid AE, Kolinski A. Coarse-grained protein models and their applications. Chem Rev. 2016;116(14):7898–7936, https://doi.org/10.1021/acs.chemrev.6b00163. Copyright 2016* American Chemical Society*; Panel C: Reprinted with permission from Muller MP, Jiang T, Sun C, et al. Characterization of lipid-protein interactions and lipid-mediated modulation of membrane protein function through molecular simulation. Chem Rev. 2019;119(9):6086–6161, https://doi.org/10.1021/acs.chemrev.8b00608. Copyright 2019* American Chemical Society*; Panel D: Reprinted with permission from Goossens K, De Winter H. Molecular dynamics simulations of membrane proteins: an overview. J Chem Inf Model. 2018;58(11):2193–2202, https://doi.org/10.1021/acs.jcim.8b00639. Copyright 2018* American Chemical Society.

is to develop FFs that can satisfactorily reproduce specific sets of experimental data. In the bottom-up approach, the CG model employs building blocks capable of reproducing atomic-level properties obtained from AA-MD simulations or from experimental. It is also possible to mixed up both approaches. The developers of the MARTINI FF adopted the bottom-up approach. MARTINI represents the currently most widely employed CG model for studying membrane systems. Although originally designed in 2003 for lipids,[176] this FF has since gone through developments both vertically (improvement in parameters for studying the same class of system) and horizontally (development of parameter sets for studying new system classes). The MARTINI FF has since been extended to most major biomolecules like proteins,[177] carbohydrates,[23] and nucleic acids.[178,179] Therefore, our focus in this chapter is the MARTINI FF because of its wide extensibility to a range of other macromolecular systems.

2.2.1 The MARTINI CG model

2.2.1.1 The all-atom to coarse-grained mapping

One of the implications of coarse-graining is the replacement of the atomic representation with few pseudoparticles (called beads) and pseudo-bonds. The MARTINI model generally employs a mapping scheme that represents four atoms with one CG bead; there are some special situations that require the assignment of fewer atoms to a bead. The speed up achievable with the MARTINI model is immediately apparent if one considers the implication of the reduced degree of freedom. In AA-FFs, atom types are required to more accurately describe different chemical environments (see chapter "Pairwise-additive and polarizable atomistic force fields for molecular dynamics simulations of proteins" by Lemkul and also Section 2.1). For instance, in the GROMOS53A6 UA-FF, the 17 atoms commonly encountered in biomolecular systems have specially defined parameter sets. Carbon, oxygen, nitrogen, and hydrogen have 15, 9, 7, and 3 atom type definitions, respectively; in total, there are 53 atom types for all seventeen atoms. This directly leads to $53!/(2! \cdot (53-2)!) = 1378$ combinations of nonbonded atom type pairs. By mapping four heavy atoms into one CG current implementation (version 2.2) has four essential bead types:

(1) apolar bead C for modeling hydrophobic groups like butane;

(2) polar bead P for modeling groups that are readily soluble in water such as ethylene glycol;

(3) nonpolar bead N for modeling groups which are partly polar and partly apolar like propyl alcohol); and

(4) charged bead Q for modeling explicitly charged groups like ammonium.

A greater resolution is achieved by having subtypes for each of the four bead types: P_{1-5} and C_{1-5} represent increasing level of polar and apolar features, respectively, while Q_d/N_d, Q_a/N_a, Q_{da}/N_{da}, and Q_0/N_0 describe the hydrogen bonding (HB) ability of charged and nonpolar beads based on whether they are HB donor (d), HB acceptor (a), HB donor and acceptor (da), or unable to participate in HB formation (0). In total, 18 distinct types of CG beads are natively available in the MARTINI FF translating to $18!/(2! \cdot (18-2)!) = 153$ possible combinations of nonbonded bead pairs.

To correctly treat certain chemical groups, MARTINI employs special beads that are parametrically different from the 18 bead types. First, smaller beads are required to correctly model structural peculiarities, especially in ring systems where two or three atoms are mapped to one CG bead. Such beads are distinguishable in the topology by having an S prefix (e.g., SP for a small polar bead) with the LJ parameters scaled down. The normal MARTINI CG beads employ a vdW radius of $\sigma = 0.47$ nm (see Eq. 4), while a value scaled down by 91.5% is employed for the S beads, but only when computing interactions with another bead of the S subtype. Similarly, the ε value (corresponding to the LJ well depth and binding energy between two atoms/beads, see Eq. 4), associated with the main bead types is scaled by 0.75 when computing the interaction between two small beads. Second, specially big antifreeze particles, called BP4, with their vdW radius scaled up to $\sigma = 0.57$ nm and to $\varepsilon = 5.6$ kJ/mol for all interactions with P4 beads of the MARTINI CG water model were introduced. The large particle size of the BP4 beads as well as the strong interaction with water beads disrupt the otherwise neatly ordered lattice packing of the similarly sized water beads, which in earlier MARTINI version caused the water to freezing at temperatures higher than the freezing point of real water.[63]

The detailed presentation of the few bead types illustrates the basis of simulation speedup and improved sampling of the phase space achievable with a CG model like the MARTINI FF. Improved efficiency is obtained in many more ways, including simplified representation of bond types and the use of a uniform bead mass of 72 amu (equivalent to the mass of four water molecules). AA-FFs often use different force constants, equilibrium bond lengths, and angles for treating bonded potentials (Section 2.1). Instead, the MARTINI FF uses a 1.25×10^3 kJ mol^{-1} nm^{-2} harmonic force constant and a 0.47 nm equilibrium length for its pseudo-bonds. However, the FF retains the flexibility of tuning both force constant and equilibrium distance in cases, where more accurate description of molecular topology is desired. A particularly large increase in computational efficiency is achieved by the use of short-range potentials. The potential energy function employed by the MARTINI model closely mirrors the generally adopted expression in most AA-FFs (the full potential energy function is presented in Eqs. 3 and 4), i.e., the vdW interaction is modeled using the LJ 12/6 potential and electrostatic interactions are modeled with the Coulombic function. Beads *i* and *j* are separated by a distance r_{ij}, ε_{ij} is the LJ well depth and binding energy between beads *i* and *j*. The LJ interaction strength is discretized into 10 energy levels (0 to IX) parameterized to reproduce oil/water partition constants and varying from a most attractive $\varepsilon = 5.6$ kJ/mol interparticle binding energy to the least attractive $\varepsilon = 2.0$ kJ/mol as it may occur for a charged bead interacting with a strongly apolar bead.[63] The LJ parameter σ_{ij} is the vdW radius of the bead using 0.47 nm as the default. Special cases, involving aromatic rings require the use of CG beads with smaller bead radius, that is the S bead discussed above. Together, these result in a distance-dependent accounting of the LJ energy, which is continuously shifted in a way that it becomes zero at 1.1 nm cutoff. It should be noted that in MARTINI dipolar interactions, involving partial charges, are adequately captured by the LJ interaction matrix just explained, such that only the interactions involving explicitly charged beads of the Q type (with charges q_i and q_j) are modeled with a Coulombic expression. In order to correct the increase in hydration strength resulting from some of the recently introduced bead types, the dielectric constant in the latest version of the MARTINI FF was reduced from $\varepsilon_r = 20$ employed in the 2003 model[62] to $\varepsilon_r = 15$.[63] The Coulombic interactions are similarly screened to zero at 1.1 nm cutoff as done for the LJ potential.

2.2.1.2 CG mapping of lipids

Currently, the MARTINI FF provides parameter sets for different classes of lipids, which cumulated to over ~214 lipid models available at the MARTINI website.[180] The major classes of lipids include mainstream phospholipids, like PC, PE, PS, PG, PA, and PI, glycerols, lysophosphatidylcholine, SM, ceramides, glycosphingolipids, glycoglycerolipids, sterols, surfactants, and fatty acids (few examples are shown in Fig. 7C). Models for other smaller lipid classes like cardiolipin, bolalipid, and lipopolysaccharide are also provided. Using the CG mapping protocol discussed above and the lipid dipalmitoylphosphatidylcholine (DPPC– 16:0,16:0, see also Figs. 2A and 7A for the chemical structure of PC and palmitoyl moiety) as an example, we will describe the CG mapping scheme presented in Fig. 1A in Ref. 181.

As earlier discussed, the structure of most lipids is traditionally divided into a head group which is usually charged or polar, and one or more aliphatic tail groups. The differences among the thousands of lipids in existence essentially derive from the structural differences in the head groups and aliphatic tails. The head group of DPPC consists of a positively charged choline ($N^+(CH_3)_3$, dark blue bead in Fig. 7A lipid structure) which in the MARTINI FF is modeled with a Q_0 bead (charged without forming HB), and a negatively charged phosphate (PO_4, orange bead in Fig. 7A lipid structure) group modeled as Q_a (charged and acting as HB acceptor). With these assignments, the charged state and the hydrogen bonding property of the lipid head group are appropriately captured (the charge of each bead needs to be explicitly specified in the topology parameter file). The two uncharged C_{16}-aliphatic chains of palmitic acid (light blue beads in Fig. 7A lipid structure) are each represented with four C_1 beads, which are hydrophobic and with the least possible polarity. There are certain instances, however, where the chemistry of the compound demands some degree of uneven distribution in the CG mapping. In such a situation, the exact choice of mapping will ultimately depend on the user but importantly also on the property to be investigated. In a case where the the lipid aliphatic tails contain uneven number of carbon atoms, e.g., for a C_{15} saturated system, there is the additional need to maintain molecular symmetry in the mapping. For instance, using -$C_1(3)$-$C_1(4)$-$C_1(4)$-$C_1(4)$ bead (number of atoms per bead in parentheses) mapping for the *sn*-1 tail and -$C_1(4)$-$C_1(3)$-$C_1(4)$-$C_1(4)$ mapping for the *sn*-2 tail would introduce some level of dissymmetry in the two tails.[63] The charged PC head group and the hydrophobic lipid tail region are linked together by a glycerol backbone, which forms an ester bond with each aliphatic tail (Figs. 2A and 7A). This glyceryl ester bridge is represented with a nonpolar HB acceptor N_a bead (red beads in Fig. 7A lipid structure) for each of two the hydrophobic tails. Qualitatively, this representation suffices since the otherwise electronic (polar and HB) property has been coarse-grained into the N_a linker bead. This is especially appropriate since the standard bond length has been reduced to 0.37 nm for this particular bead in an attempt to capture its peculiarities.[63] However, if it is desirable to more explicitly reflect the polarity of the C_1 bead proximal to the polar linker bead, it is possible to tune MARTINI parameters to capture the specific property of interest.

Because of its versatility and acceptable accuracy at reproducing experimental and atomistic MD data, the MARTINI model has rapidly grown to become the most popular CG lipid FF that has been extended to many biomolecular and polymer systems. This was achieved in spite of its simplicity in the treatment of chemical systems and the unavoidable loss of atomic resolution.[62,63,176] By reducing the degrees of freedom in a physicochemically meaningful manner and, by adopting a bottom-up parameterization approach focused on reproducing experimental thermodynamic properties, the FF has been able to achieve a good degree of transferability to nonlipid biological systems, for which it was not originally designed. Good concordance with experimental data was obtained in the values of the partition free energy with various solvent systems as presented in Table 3 reproduced from reference.[63] In most cases, agreement between the MARTINI model (computed from the density distribution for the MARTINI model) was obtained within 1 $k_B T$ of experimental partition free energy values, and in some cases within 2 $k_B T$ (Boltzmann constant: $k_B = 1.381 \cdot 10^{-23}$ m^2 kg s^{-2} K^{-1}; Temperature: $T = 293$ K). A consequence of modeling nonbonded interaction with the LJ 12/6 potential is an overestimation of vaporization and hydration free energies, which was also observed for the MARTINI FF. This was shown to result in the underestimation of the water/vapor tension, especially in tested systems containing 1600 CG beads. Nevertheless, this is not of great concern as long as it is employed in studying condensed phases, where events are mostly governed by the partition free energies, which were correctly reproduced by the MARTINI FF. And of course, properties dependent on the degrees of freedom approximated out by the MARTINI FF cannot be directly investigated, expect by coupling to a multiscale modeling procedure. This is exemplified by the relative insensitivity at reproducing thermodynamic data for 1-propanol and 2-propranol[63] in Table 3.

The MARTINI FF described here refers to version 2.2. Since 2018, the beta version of MARTINI 3 is available, which contains topologies for over 120 lipids, includes new beads types, and revised parameters for some of the existing bead types. However, the MARTINI 2.2 lipid parameters are mostly unaffected by the transformation to version 3; rather the parameterization of the protein beads was revised as the protein–protein interactions are generally too attractive in MARTINI 2.2.[182]

2.2.2 Other lipid CG models

Some of the other popular CG-FFs available for simulation of membrane lipids include the SDK (named after its developers Shinoda–DeVane–Klein) FF,[93] later extended as SPICA FF,[183] the ELBA (stands for electrostatic-based) FF,[184] the SIRAH FF,[185] and the UNRES FF[186] (see also chapter "Scale-consistent approach to the derivation of coarse-grained force fields for simulating structure, dynamics, and thermodynamics of biopolymers" by Liwo of this book). The SDK CG lipid FF was originally developed for the study of surfactants and zwitterionic lipids.[93] Developed by Shinoda, DeVane, and Klein in 2010, it represents an extension of an earlier CG-FF by the same authors dedicated to the simulation of polyethylene

Table 3 Predicted versus experimental thermodynamics data (in bracket).

Bead type	Sample fragment	ΔG_{vap}	ΔG_{hyd}	$\Delta G_{H/W}$	$\Delta G_{C/W}$	$\Delta G_{E/W}$	$\Delta G_{O/W}$
C_1	Butane	−10 (−11b)	14 (9)	18 (18)	18 (NA)	14 (NA)	17 (16)
C_2	Propane	−10 (gas)	10 (8)	16 (NA)	15 (NA)	14 (NA)	16 (14)
C_3	1-Chloropropane	−10 (16)	5 (−1)	13 (12)	13	13	14 (12)
C_4	2-Butyne	−10 (−15)	5 (−1)	9 (NA)	13	13	9 (9)
C_5	Methyl ethyl sulfide	−10 (−17)	1 (−6)	5 (7)	10 (NA)	10 (NA)	6 (9)
N_0	Methoxyethane	−10 (−13)	−2 (−8)	−2 (1)	6 (NA)	6 (3)	5 (3)
N_a	2-Propanone	−13 (−17)	−9 (−16)	−7 (−6)	0 (1)	2 (−1)	3 (−1)
N_d	2-Propylamine	−13 (−17)	−9 (−18)	−7 (−6)	0 (1)	2 (−3)	3 (3)
N_{da}	1-Butanol	−16 (−25)	−9 (−20)	−7 (−5)	0 (2)	2 (4)	3 (4)
P_1	1-Propanol	−16 (−23)	−14 (−21)	−11 (−9)	−2 (2)	1 (0)	−1 (1)
P_1	2-Propanol	−16 (−22)	−14 (−20)	−11 (−9)	−2 (2)	1 (−1)	−1 (0)
P_2	Ethanol	−16 (−22)	−14 (−21)	−17 (−13)	−2 (−5)	1 (−3)	−2 (−2)
P_3	Acetic acid	−18 (−31)	−18 (−29)	−21 (−19)	−10 (−9)	−6 (−2)	−7 (−1)
P_4	Water	−18 (−27)	−18 (−27)	−23 (−25)	14 (NA)	−7 (−10)	−9 (−8)
P_5	Acetamide	sol (sol)	−25 (−40)	−28 (−27)	−18 (−20)	−13 (−15)	−10 (8)
$Q_0/Q_a/Q_d/Q_{da}$	Choline	–	−25 (NA)	−30 (<30)	−18 (NA)	13 (NA)	−18 (NA)

Data are shown for free energies of vaporization (ΔG_{vap}), hydration (ΔG_{hyd} (exp.)), and partitioning in hexadecane/water ($\Delta G_{H/W}$), chloroform/water ($\Delta G_{C/W}$), ether/water ($\Delta G_{E/W}$), and octanol/water ($\Delta G_{O/W}$) binary mixtures for different studied building blocks modeling different bead types. Extended data available in Ref. 63 from which the data were sourced.

glycol surfactants[92] and has been shown to reliably reproduce water/lipid interfacial tension. The ELBA FF was developed by Orsi and Essex and it employs two interdependent properties, explicitly modeled electrostatics and water molecules with single-point dipoles.[184] The SIRAH FF is another commonly employed CG-FF with parameters for a range of different molecules, including lipids, proteins and nucleic acids. The SIRAH FF is based on a top-down philosophy that aims to correctly reproduce lipid thickness and area per lipid among other membrane properties.[185]

2.3 Which lipid FF to choose for a simulation?

Choosing the right FF for the protein–membrane system to some extent depends on the availability of the right parameters for the desired lipids. The C36-AA, UA, GROMOS and MARTINI FF contain the largest variety of lipids as can be seen in Table 4.[97] Here, GROMOS currently has no FF parameters for chains with cyclic moieties, which are important in certain bacterial membranes, but in general GROMOS is able to simulate the same diversity of lipids as compared to C36-AA. Only parameters for ether lipids and lipid chains of bacteria are missing in the MARTINI FF, whereas Slipids and Lipid14 lack a variety of lipids. With the head group as AA, the C36-UA-FF would be similar to the C36-AA, however, it exhibits inaccuracies and can currently not be recommended for lipids other than PC and PE.[97] In general, the SDK FF could be an alternative to the MARTINI CG-FF, however, it has currently only a limited number of lipid and surfactant molecules implemented.

Table 4 Lipid parameters availability in the different FFs.

Lipids	**C36-AA**	**Slipids**	**lipid14**	**GROMOS**	**OPLS-AA**	**C36-UA**	**MARTINI**
PC/PE	✓	✓	✓	✓	✓	✓	✓
PG/PS/PA	✓	PG/PS	x	✓	PS	x	✓
PI/PIs	✓	x	x	✓	PI	x	✓
SM/Cer	✓	SM	x	✓	SM	x	✓
Sterols	✓	CHOL	CHOL	✓	CHOL	x	✓
Others[a]	✓	PUFAs	x	✓	ether, oxidized, GM1	x	✓

[a] Here, the less common lipids are summarized: CL, ether lipids, glycolipids, LPS, fatty acid, surfactants and PUFAs.

A tick means that all lipids of that group are available, while a cross indicates that none of the lipids in question are parameterized in the corresponding FF. Sterols include cholesterol, ergosterol and plant sterols if it is not marked otherwise.

3. MD simulation setup and analysis of protein–membrane systems

Biological membranes are complex and consist of different species of lipids, proteins and sugars. Recent developments in the field have enabled researchers to gain insights into the structure and function of biological membrane systems at atomistic resolution. In the following sections, we first present programs and tools that are available to build protein–membrane systems and prepare the input for corresponding MD simulations. Finally, we briefly discuss different tools for analyzing membrane properties from protein–membrane MD simulations.

3.1 CHARMM-GUI

To build initial protein–membrane systems for MD simulations in atomistic and CG resolution, the web-based and user-friendly CHARMM-GUI server,[126] developed by Im's group (http://www.charmm-gui.org/), has become widely popular over the last 10 years since the project started in 2006.[187,188] Currently, there are 434 different lipids available for the selection as a membrane component: GPLs, sterols, CLs, PUFAs, SM, detergents, ether-linked GPLs, fatty acids, LPS and glycolipids. There is the possibility to prepare both single- and multicomponent membranes, including the option of varying lipid concentration between the two leaflets. Moreover, the files that are generated by CHARMM-GUI are compatible with several MD engine programs,[164,188,189] including GROMACS,[190,191] AMBER,[192] NAMD,[193] GENESIS,[194] OpenMM,[195] CHARMM/OpenMM,[196] LAMMPS,[197] and Desmond.[198] Several *builder* and *maker* programs to create protein–membrane, protein–ligand, and protein–protein systems were developed within CHARMM-GUI. Here, we concentrate on setting up protein–membrane MD simulations via the *Membrane Builder* and *MARTINI Maker*. *Membrane Builder* offers different options to generate bilayers, monolayers, nanodisc, hexagonal phases and micelles with and without protein, as discussed in more detail below. At this stage, the force field parameters of CHARMM36 or CHARMM36m have to selected, which can be converted for use with several MD engines, including the change to another FF when running the MD simulations as explained in Section 3.2. To get further information about CHARMM-GUI, visit the http://www.charmm-gui.org/ website or consider this review.[188] All the lipid and protein files for the different CHARMM FFs can be downloaded from the MacKerell lab homepage (http://mackerell.umaryland.edu/charmm_ff.shtml#gromacs).

3.1.1 PDB loader and manipulator

Membrane Builder provides a PDB loader, which at the starting step imports a protein structure from either the OPM[44] database or the RCBS PDB.[42,43] In the next step, the user can decide to use the whole or only part(s) of the loaded protein, for instance, only a certain chain or certain residues of each available chain. Furthermore, the protein structure can be modified by the PDB manipulator to introduce cap groups, mutations, disulfide bridges, unnatural amino acids, or posttranslational modifications, including glycosylation, lipidation for a lipid anchor, phosphorylation, or attachment of a GPI-anchor. Additionally, the protonation state of each residue can be defined or missing residues can be added. Afterwards, the orientation of the protein in or on the membrane can be defined by the user if one does not want to use the preoriented protein coordinates provided by OPM. Several options, like protein flipping, translation along the z-axis, or rotation in the xy-plane are available. The Position of Proteins in Membrane (PPM) server may be of help here, as it calculates rotational and translational positions of transmembrane and peripheral proteins in membranes.[199] It is thus possible to place the protein in or on the membrane, or with a defined distance away from the membrane. At each step, the user can check the conformation of the protein and its position relative to the membrane. The next step is then to build the envisaged membrane type with the desired lipid composition.

3.1.2 Mono- and bilayer builder

Mono- and bilayer membranes can be built with CHARMM-GUI, where one can choose from 434 lipids that are currently available for creating realistic membranes. Next, the user can decide on the size of the membrane and the ratio of the chosen lipids in each leaflet. The desired protein can then be inserted into the membrane system, which will be done by a replacement or an insertion algorithm. In the last step, the user can choose the FF (CHARMM36m, CHARMM36, and most recently also AMBER lipid17), the MD software engine for which the input files shall be generated, and the MD parameters like temperature and ensemble.

3.1.3 Nanodisc builder

In many biophysical and biochemical studies, nanodiscs are used for studying membrane proteins in solution and are often better biological membrane mimics than micelles, liposomes, or bicelles. Nanodisc are stabilized by surrounding membrane scaffolding proteins (MSPs) to build a discoidal lipid bilayer. Most of the MSPs are derived from the apolipoprotein A-1 (apo A-1) with the long helical structure as it generates the discoidal shape of high-density lipoprotein (HDL), which is involved in cholesterol transport from the artery walls to the liver for degradation. In CHARMM-GUI, the *Nanodisc Builder* allows to create nanodisc systems involving proteins, which can also be inserted into the nanodisc. Depending on the size of the nanodisc, users can choose from twelve different MSPs, which are able to modulate the size of the nanodisc and includes a double-belt model for placing the MSP molecule around the nanodisc. For more details about MD simulation of nanodiscs the reader is referred to other references.[200,201]

3.1.4 Micelle and hex phase builder

In CHARMM-GUI, it is also possible to build micelles with the option to choose from more than 20 detergents and to insert proteins into the micelles.[202] The effects of detergents on protein structure are poorly understand. MD simulations of protein–micelle systems can help to elucidate the behavior of membrane proteins in certain detergents.[202] Similarly, the *Hex Phase Builder* can be used to assemble lipids in the hexagonal phase state, in which the polar head groups are located inside and form a water environment in the inverted micelle (Fig. 3C). This state can occur at high temperatures or low water concentration and has been applied in biophysical experiments and MD simulations to obtain information on lipids at high curvature.[203–205] Protein and/or interstitial alkane can be added to the system and all lipids are available for building this phase.

3.1.5 HMMM builder

CHARMM-GUI provides the possibility to build membrane systems with the HMMM model,[64,206] in which the lipid tails are replaced by small organic molecules, e.g., 1,1-dichloroethane (DCLE). This results in acceleration of lipid diffusion inside the membrane by 1–2 orders of magnitude. All available lipids are supported and it can also be chosen at which carbon position the acyl chains will be cut. There is also the possibility to convert the HMMM model back to the full-length lipid system.

3.1.6 MARTINI builder

Different CG models exist that allow to simulate large protein–membrane systems. One of them is MARTINI,[207] which is also available in CHARMM-GUI. *MARTINI Builder* enables the user to build solution, micelle, nanodisc, bilayer, and vesicle systems and also systems with randomly distributed detergent or lipid molecules for subsequent MD simulations with MARTINI. Furthermore, LPS are available and have been successfully applied with *MARTINI Builder* to model realistic bacterial outer membranes.[208] In CHARMM-GUI, the standard MARTINI version,[62,63,177] MARTINI with polarizable water,[209,210] Dry Martini,[211] and ElNeDyn[212] that applies an elastic network to the proteins are supported. However, the generated MD input files are only compatible with the latest GROMACS software.[190] The conversion from the CG MARTINI presentation to the AA level is available in CHARMM-GUI via the *backward.py* script.[213]

3.2 Setting up protein–membrane system with other programs

The CHARMM-GUI server facilitates setting up different kind of systems, but there are certain limitations. The choice of FF is mainly limited to the CHARMM FF. Chemical modifications of proteins or lipids are restricted to the options available in the server and it is not possible to insert several proteins or drug molecules into a membrane at the same time at varying depth. Recently, the server has been updated to provide AMBER FF files for simulations. To overcome the limitations with the CHARMM-GUI sever, we discuss here the set up of protein–membrane systems for other commonly used force fields.

3.2.1 Simulations with AMBER FF

Here, users can make use of CHARMM-GUI to build the initial protein–membrane system. For lipids, simply using Slipids FF files[79,80,142] is sufficient since it follows the same atom naming as CHARMM C36. For proteins, processing the protein PDB file (*pdb2gmx* tool in GROMACS) with the desired AMBER protein FF should work. CHARMM-GUI and PACKMOL-Memgen[214] can be used to generate PDB files compatible with AMBER Lipid17. Many structures, topology and preequilibrated mono- and multicomponent membrane patches for Slipids can be downloaded at: http://www.fos.su.se/~sasha/SLipids/Downloads.html.

3.2.2 Simulations with OPLS-AA FF

There is no freely available tool for setting up protein–membrane systems with OPLS-AA. Also, the atom naming does not follow that of CHARMM C36 lipids or AMBER Slipids, suggesting that converting a CHARMM-GUI output to OPLS-AA is not possible. Instead, the setup of a protein–membrane system can be done in two steps. First, tools such as

MemGen[215] and PACKMOL[216] can be used to build the pure lipid membrane from a PDB file of a single lipid. Second, the protein can be positioned above the membrane surface using VMD[217] or using the GROMACS tool *editconf*. For TM proteins, the protein may be embedded inside the membrane using VMD, *mdrun_hole*,[218] *InflateGRO*,[219] *InflateGRO2*,[220] or *g_membed*.[221] However, these tools remove lipids overlapping with the protein, which is problematic when preparing multicomponent systems with varying concentrations. Addressing the problem, Javanainen et al.[222] developed a universal protocol to insert proteins of various topology inside the membrane without having to remove the lipids. The method is independent of any FF and works by applying high lateral pressure. Thus, for simulations with OPLS-AA a combination of either *MemGen*[215] and PACKMOL[221] for building the initial membrane patch along with the method developed by Javanainen et al.[222] is probably the most efficient way for setting up a protein–membrane system. Topologies, structures, and parameter files for OPLS-AA can be obtained from Kulig et al.[150,151]

3.2.3 Simulations with GROMOS FF

The GROMOS united atom membrane patch can be prepared using *MemGen*,[215] PACKMOL,[221] *MemBuilder*[223] tools or by downloading preequilibrated bilayer patches. The *MemBuilder*[223] tool already includes structure and topology files for few selected lipids. With the method by Javanainen et al.[222], the protein can be placed into the membrane. If the protein has to be positioned above the membrane surface, either VMD[217] or the *editconf* tool of GROMACS can be used. Structures, topologies, and membrane patches can be downloaded from Peter Tieleman's webpage (http://wcm.ucalgary.ca/tieleman/downloads), Jochen Hub's webpage (https://biophys.uni-saarland.de/downloads.html), Mikko Karttunen's webpage (https://www.softsimu.net/downloads.shtml), Andreas Kukol webpage (https://sites.google.com/site/bioherts/home/lipid-topologies), Roland Feller's webpage (https://research.engineering.ucdavis.edu/multiscale/downloads/), and those uploaded on the GROMACS website (http://www.gromacs.org/Downloads/User_contributions/Molecule_topologies). Cholesterol-containing membrane structures are available at Jochen Hub's website at https://biophys.uni-saarland.de/downloads.html.

3.2.4 Simulations with MARTINI FF

The developers of MARTINI (http://cgmartini.nl/) also provide scripts to build protein–membrane systems, along with tutorials for the different applications to set up the desired systems and how to map new molecules from atomistic to CG resolution. Here, we briefly describe the possibilities of building protein–membrane systems with certain scripts. First, the Python script *martinize.py* automatically converts a PDB file of proteins, DNA or RNA from the AA to the CG model, where the user can decide to use standard MARTINI model for proteins, the elastic network model, or the ElNeDyn method. The elastic network ElNeDyn[212] maintains the overall conformation of a protein and limits the capability of changing the tertiary structure (Fig. 7D). Moreover, there is the possibility to change the protonation state of the histidines and to define disulfide bridges. Second, the python script *insane.py*[224] enables the user to setup homogeneous and heterogeneous membranes with the possibility to place and rotate the protein molecules above or on the membrane or move them inside.

3.2.5 Glycosylation

Proteins undergo several posttranslational modifications, such as covalent linkage of N- and O-bound glycans to proteins.[225–227] Similarly, many cell membranes contain glycolipids, which are decorated with sugar head groups, e.g., gangliosides. The software *doGlycans*[228] can be used to glycosylate proteins, or set up glycolipids and cellulose structures. The tool is user friendly and provides files compatible for use with OPLS-AA, AMBER, and CHARMM. CHARMM-GUI also enables users to add glycans to the proteins during system setup.[229]

3.3 MD simulation software packages

Numerous MD software packages have been developed by different research groups, whereby the most popular MD programs are summarized in Table 5. They differ in the availability of implemented algorithms, e.g., for the integration of Newton's equations of motions (see Eq. 2), the available thermostats and barostats, in their computational performance, in their support of various FFs, and in their availability of analysis tools. In GROMACS and NAMD, one can choose from a wide range of standard and custom FFs (e.g., all kinds of CHARMM, OPLS-AA, and AMBER FFs), whereas the MD engines CHARMM and AMBER only support their own FFs. Furthermore, some MD software packages are not freely available, such as AMBER for performing MD simulations but the corresponding analyzing package AmberTools[230] is freely available for academic purpose. Finally, the user has to consider which analysis tools are provided by the MD programs. For example, GROMACS has the big advantage that it comes

Table 5 Common MD software packages.

Software	Interface	License	Website
AMBER[192]	CLI	Proprietary	https://ambermd.org/
CHARMM[189]	CLI and GUI	Proprietary	https://www.charmm.org
Desmond[198]	GUI	Academic	https://www.deshawresearch.com/resources_desmond.html
GROMACS[190]	CLI	Open-source	http://www.gromacs.org/
NAMD[193]	GUI	Academic	https://www.ks.uiuc.edu/Research/namd/
LAMMPS[197]	CLI	Open-source	https://lammps.sandia.gov/

CLI means that the program is based on the command line, while the programs with GUI provides a graphical interface for the users.

with huge and diverse set of analysis tools, covering both analyses of protein and membrane properties, which can be easily modified and redistributed if a given tool should not exactly exhibit the required functionality. NAMD is implemented in VMD,[217] which provides powerful visualization capabilities, a graphical user interface (GUI), dynamic atom selections, and allows the reading of multiple file formats, including those obtained by all common MD packages.

3.4 Analysis tools for studying protein–membrane systems

3.4.1 *Visualization and plotting tools*

The most important output file obtained from an MD simulation is the trajectory file (GROMACS: *.xtc/.trr*, CHARMM/NAMD: *.dcd*, AMBER: *.netcdf*) which contains the coordinates of the atoms as a function of time. Trajectory files can be converted between formats using the *MDTraj* tool.[231] Programs such as VMD,[217] PyMOL,[232] and Chimera[233] visualize trajectories and provide options for measuring important biomolecular properties. In addition, numerical output files from various analyses can be plotted, for example, using Xmgrace, MATLAB,[234] and GnuPlot.[235]

3.4.2 *Analysis tools*

The MD simulations packages are already preloaded with several analysis tools, which can be used to analyze the structure and dynamics of the system. Here, we list several analysis software packages, which are widely used to characterize protein–membrane systems. The LOOS tool[236] supports dynamic atom selection and is compatible with many MD simulation software packages. The *g_lomepro* tool[237] measures local changes of membrane properties due to protein interaction and it is compatible with GROMACS files. *GridMAT-MD*[238] analyzes protein–membrane properties on a 2D grid and reads GROMACS format files. The *Membrainy* tool[239] easily determines several membrane properties, such as the fraction of the gel phase or the selection of annular lipids. *Membrainy* is compatible with GROMACS files and reads CHARMM36, Berger/GROMOS87, and MARTINI v2.0 FF files. The MEMBPLUGIN tool[240] works in combination with VMD. This tool measures membrane properties and accepts input files from all FFs and MD packages. The APL@Voro tool[101] calculates membrane properties based on Voronoi tessellation and is compatible with GROMACS format file. FATSLiM[241] computes properties of both planar and curved membranes and is compatible with GROMACS files. Several tools for analyzing membrane trajectories in GROMACS format are available at Luca Monticelli's website[242] (https://perso.ibcp.fr/luca.monticelli/tools/index.html) to analyze membrane trajectories. In addition, *MDAnalysis*[243] and *MDTraj*[231] libraries also include features for analyzing protein–membrane systems.

4. Case studies for protein–membrane systems

In this section, we will give an overview about different case studies with AA-FFs and three studies for CG-FFs, which are summarized in Table 6.

4.1 Atomistic simulations of integral membrane proteins

4.1.1 G-protein-coupled receptors

G-protein-coupled receptors (GPCRs) form the largest family of cell surface membrane proteins and all share a multipass seven-transmembrane helix (TMH) topology.[244] The activation of GPCRs occurs by extracellular binding of a ligand, which triggers a conformational change in the receptor structure, leading to dissociation of a receptor-bound heterotrimeric G protein subunit (Gα and G$\beta\gamma$). The dissociated subunits interact with intracellular substrates to resume the signal transduction cascade. After dissociation of the G protein, the receptor is available to bind to another heterotrimeric G protein, thereby continuing the signal transduction.[244] Due to their role in several physiological processes, these receptors are major targets for ~35% of the currently approved drugs refer to those available in the market.[245] Thus, understanding how GPCRs function at atomistic level is essential for therapeutic intervention.

Table 6 Summary of the different case studies.

Proteins	FF	Lipids	Water model	MD package	Reference
Transmembrane proteins and receptors					
β-2AR	OPLS-AA	DOPC, CHOL, CHS, Oxysterol	TIP3P	GROMACS 4.6	[253]
$A_{2A}R$	C36, C36c, C27	DPPC, DSPC, DOPC, SDPC, SM CHOL	TIP3P	ACEMD,[a] GROMACS 5	[266]
Opsin	C36	POPC, POPG	TIP3P	NAMD 2.1, ACEMD[a]	[263]
XylE	C36	DOPC, DOPE, DOPG, CL	TIP3P	NAMD 2.12	[277]
hDAT	C27, C36	POPC, POPE, POPS, CHOL, PIP_2	TIP3P	NAMD 2.9, ACEMD[a]	[280]
Kir2.1	C27	POPC	TIP3P	NAMD2	[58]
TLR4	OPLS-AA	POPC, POPE, POPS, SM, GluCer, LPS	TIP3P	GROMACS 4.6.7	[226]
CcO	C36	POPC, POPE, CL	TIP3P	GROMACS 5	[294]
10 different membrane proteins	MARTINI	POPC, POPE, SM, LPC, GM, CER, DAG, PI, PIP, PA, CHOL	MARTINI water	GROMACS 4.6.3	[431]
Amyloids					
$A\beta_{42}$	GROMOS96, G53A6, Kukol lipids	POPC, DPPC, POPG	SPC	GROMACS 4	[319, 320]
$A\beta_{40}$	GROMOS96, G53A6, Tieleman lipids	POPC, POPE, POPS SM, CHOL, GM1	SPC	GROMACS 4	[321]
$A\beta_{42}$	OPLS-AA	POPC, SM, CHOL, GM1	TIP3P	GROMACS 4.6	[322]
$A\beta_{1-28}$, $A\beta_{26-40}$	GAFF, Slipids	DMPC, SDPC, DSPE, DDPE, DPPC, DOPC	TIP3P	GROMACS 4.6.7	[323]
$A\beta_{29-42}$	AMBER99SB*-ILDN, Slipids	POPC, $SAPC_{\omega 6}$, $SDPC_{\omega 3}$	TIP3P	GROMACS 5.1.2	[324]

hIAPP	GROMOS87, Berger lipids	POPC, POPG	SPC	GROMACS 3.3.3	[330–332]
hIAPP	Amber03w, Slipids	DOPC, DOPS	TIP4P/2005	GROMACS 4.6.7	[333]
hIAPP	GROMOS87, Tieleman lipids	POPG	SPC	GROMACS 3.3.3	[334]
hIAPP	C36, C22*	DOPC, DOPS, DVPS, DVPC	cTIP3P[b]	GROMACS 5.0.2	[172]
hIAPP	C27	DOPC	TIP3P	NAMD	[335, 336]
hIAPP	GROMOS96, G53A6	DPPG	SPC	GROMACS 4.0	[338]
aSyn	C22, C36	POPC, POPA	TIP3P	CHARMM	[349]
aSyn	C36	DOPC, SAPC, DPhPC	TIP3P	GROMACS 4	[351]
aSyn	C27, C36	DVPC, DVPS	TIP3P	NAMD 2.8	[171]
aSyn	AMBER99SB-ILDN Slipids	POPC, POPG, DMPC, DMPG	TIP3P	GROMACS 4.6	[352]
Peripheral membrane proteins					
FGF2	C36	POPC, CHOL, PI(4,5)P$_2$	TIP3P	GROMACS 5.1	[365]
GRP1-PHD	C36	POPC, POPS, PIP$_3$	TIP3P	NAMD2	[379]
ABPs	C36	POPC, POPE, POPS, PI(4,5)P$_2$	cTIP3P[b]	GROMACS 5.0.4	[380]
RVFV	AMBER99SB*-ILDN Slipids	DOPC, CHOL	TIP3P	GROMACS 4.6	[408]
Integral membrane proteins					
FAM134B-RHD	C36m, MARTINI	POPC	TIP3P, MARTINI water	GROMACS 4.6,5	[417]
Lipid droplets					
Seipin	SDK	POPC, DOPC, CHOL DPPC, DOPE, DAG	SDK water	LAMMPS	[419]

[a] ACEMD is a high performance MD code specifically designed for NVIDIA GPUs.
[b] cTIP3P refers to the CHARMM-modified TIP3P water model.

Recent technical advances have enabled structural biologists to solve structures of several GPCRs, which in turn has provided a wealth of information on ligand binding pockets, on key residues stabilizing the ligand–receptor interactions, and on functionally important conformational changes of GPRCs, such as the rotation and movement of helices during activation. However, GPCRs are embedded in lipid environment and our understanding on how phospholipids and sterols, which form the major components of cell membrane, modulate the receptor function is still limited. Therefore, insights into the lipid species interacting with the GPCRs is relevant to further understand the GPCRs activation mechanisms. Among the membrane components, the role of cholesterol in GPCR function has been intensively investigated.[246] In vivo studies have indicated cholesterol to be an important modulator of GPCR activity and several functions are attributed to cholesterol in regulating GPCR functions, such as ordering of lipid membrane, stability and oligomerization of receptor and in binding of ligands.[247–250] In addition, cholesterol is also required for crystallization of GPCRs.[37,251] Furthermore, GPCR structures have been resolved with cholesterol and its analogues bound to the receptor, indicating direct interactions with the receptor.

Rhodopsin is one of the best-studied GPCRs. Its interaction with lipids containing PE head group, polyunsaturated acyl chain (e.g, docosahexaenoic acid, DHA, 22:6), and with cholesterol is known to trigger visual processes.[252] To complement experimental findings and to gain further insights into the interactions between GPCRs and lipids, MD simulations of various GPCRs embedded in lipid membrane have been carried out, including β_1 and β_2-adrenergic receptors,[253,254] serotonin 1A and 2A receptors,[255,256] cannabinoid 2 receptor,[257] rhodopsin,[258] A_{2A} adenosine receptor,[259,260] δ opioid receptor,[261] sphingosine 1-phosphate receptor,[262] opsin receptor,[263] and dopamine D2 receptor.[264] Here, we will discuss key findings obtained from atomistic MD simulations for few selected GPCRs.

4.1.1.1 β2-adrenergic receptor (β_2AR)

The human β_2AR is primarily expressed in pulmonary, skeletal, and cardiac muscles. It is a major drug target for treatment of asthma, respiratory diseases and heart failure. Recent structural and biochemical studies suggest that the receptor exists in multiple conformations and that binding of cholesterol affects the conformation and signaling. Cholesterol could induce its effect either by altering the membrane properties or by direct specific interactions with the receptor. Although structures solved with cholesterol bound to

β_2AR indicate the availability of specific cholesterol binding sites on the receptor, the mechanism explaining the modulatory role of cholesterol is still unknown. To clarify the effect of cholesterol on β_2AR, Manna et al.,[253] performed extensive atomistic MD simulations (>100 μs) of β_2AR embedded in 1,2-dioleoyl-*sn*-glycero-3-phosphocholine (DOPC)/CHOL membrane, with cholesterol concentration ranging from 0 to 40 mol%. In addition, simulations were also carried out using the cholesterol analog cholesteryl hemisuccinate, since it is commonly used in experiments to mimic cholesterol. This study reported two binding sites on the intracellular side (IC1 and IC2) and one binding site on the extracellular side (EC1) for cholesterol (Fig. 8A and B). Binding at IC1/EC1 sites are supported by with the crystal structures,[37,251,265] however, the relevance of the additional binding at site IC2 has to be experimentally validated. Cholesteryl hemisuccinate also binds to β_2AR at the same sites as cholesterol, but the binding is weaker in comparison to cholesterol. The study also shows that in the absence of cholesterol, β_2AR adopts multiple conformations, whereas with cholesterol concentration >10 mol% the structural flexibility of β_2AR is reduced to one single conformation. These studies conclude that the modulatory effect of cholesterol functions via specific interactions with the receptor and not via modulating the mechanical membrane properties.

4.1.1.2 Adenosine A2A receptor (A_{2A}R)

The receptor is expressed across several tissues. The highest expression levels are found in brain and intermediate levels in heart, where it regulates blood flow and oxygen consumption. A_{2A}R is a target for drugs in the treatment of Alzheimer's and Parkinson's disease. Similar to β_2AR, cholesterol binding sites have been reported from both experimental (e.g., PDB code: 3EML[267])[265] and MD studies.[259,260] Also, a stabilizing effect of cholesterol on the receptor has been shown.[260] However, the effect of cholesterol on ligand binding has not been explored. To clarify this, Guixà-González et al.[266] combined both experiments and MD simulations to understand how cholesterol depletion influences ligand binding and dynamics of A_{2A}R. The MD simulations revealed that on average 12 cholesterol molecules are bound to the receptor. The cholesterol molecules were found preferentially bound to TMH2-3, 3-4-5 and 7-1 (Fig. 8C). Of the three regions, cholesterol binding to TMH2-3 is supported by with the experimental structure solved in complex with the ligand.[265] The bound cholesterol molecules are required to maintain the stability of the receptor as observed in experiments. Apart from confirming the experimentally known

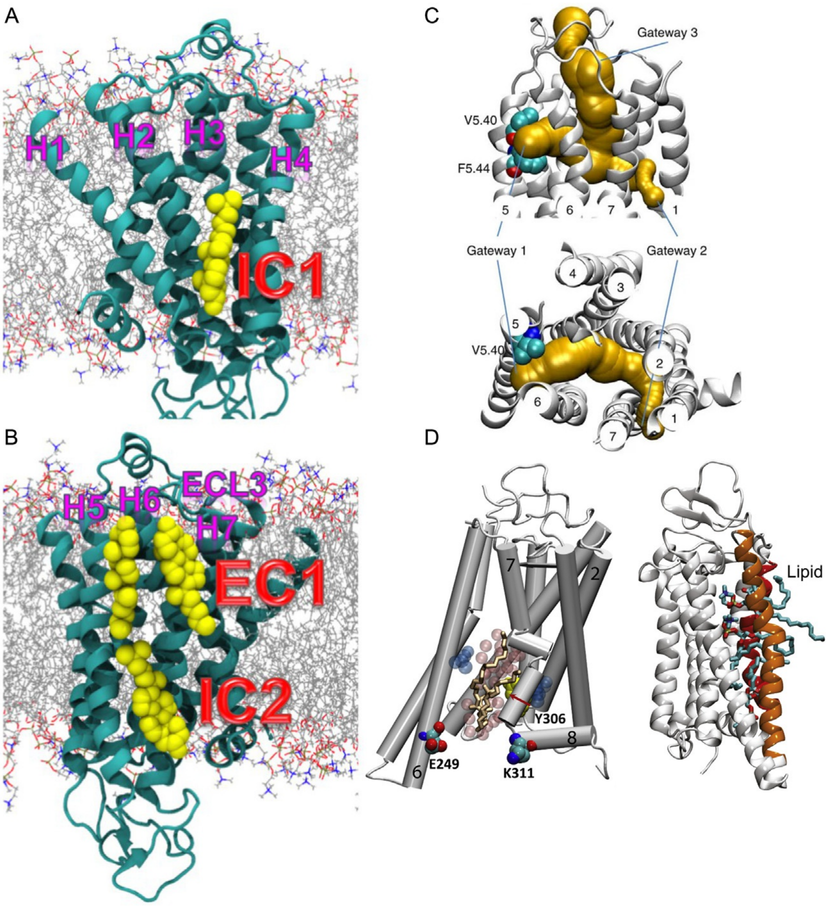

Fig. 8 GPCRs in action. (A) and (B) Cholesterol interactions with β_2AR. β_2AR embedded in a lipid membrane (*line representation*), highlighting two intracellular cholesterol binding sites IC1 (H1–H4) and IC2 (H5–H6) as well as one extracellular binding site EC1 (H5–H6 and H6–ECL3–H7). Cholesterol is rendered as *yellow spheres*. (C) Cholesterol gateways (*yellow surface*) in A_{2A}R. *Top* and *bottom* figures represent views from intracellular and extracellular sides, respectively. TMHs are marked from 1 to 7. (D) Lipid translocation triggered by opening on the intracellular side of the Opsin receptor. In the *left panel*, final snapshot showing disruption of E249–K311 interactions and conformational switch of Y306 inducing water pore (*transparent pink spheres*) and lipid penetration (rendered as *licorice*). In the *right panel*, snapshot showing translocation of lipids as a credit-card mechanism. TMHs involved in conformational rearrangement are labeled (H2/6/7/8). *Panels A and B: Reprinted with permission from Manna M, Niemelä M, Tynkkynen J, et al. Mechanism of allosteric regulation of β_2-adrenergic receptor by cholesterol. eLife. 2016;5:e18432, 10.7554/eLife.18432, eLife Sciences Publications. Copyright © 2016 (https://creativecommons.org/licenses/by/4.0/); Panel C: Reprinted with permission from Guixà-González R, Albasanz JL, Rodriguez-Espigares I, et al. Membrane cholesterol access into a G-protein-coupled receptor. Nat Commun. 2017;8:14505, Springer Nature. Copyright © 2017 Springer Nature (https://creativecommons.org/licenses/by/4.0/); Panel D: Reprinted with permission from Morra G, Razavi AM, Pandey K, Weinstein H, Menon AK, Khelashvili G. Mechanisms of lipid scrambling by the G protein-coupled receptor opsin. Structure. 2018;26(2):356–367, Elsevier. Copyright © 2017 Elsevier Ltd (https://creativecommons.org/licenses/by/4.0/).*

cholesterol binding sites, few additional sites were observed on the surface of the receptor, which could affect ligand binding. The studies also revealed a mechanism in which the cholesterol enters the receptor interior, thus competing with the orthosteric ligand binding site. The path taken by cholesterol to enter the $A_{2A}R$ interior is identical to the retinal pathway in the opsin receptor. These studies indicate that ligand binding to $A_{2A}R$ receptor is regulated by both orthosteric- and allosteric binding of cholesterol to the receptor.

4.1.1.3 Opsin receptor

These receptors are found in the photoreceptor cells of the retina and are involved in vision. Opsins and several other class A GPCRs facilitate trans-bilayer translocation of phospholipids and scramble >10,000 lipids per second when embedded in vesicles.[268–270] When reconstituted in lipid vesicles, opsins are known to accelerate the lipid transfer to a rate of $>10^4$ (i.e., 10,000 lipids per second per protein), which is faster than opsin unassisted lipid transfer occurring at a rate of $\sim 10^{-5}$ s^{-1}.[271] But opsin-mediated lipid transfer is still a rare event taking ∼100 μs per lipid per protein. The lipid flipping or the scramblase activity of GPCRs is not only necessary to maintain the photoreceptor cell homeostasis but also finds importance in various other physiological processes, such as in cell growth, blood clotting and apoptotic cell clearance.[271–274] Recently, the molecular events facilitating the receptor-mediated lipid scrambling were characterized by preinserting opsin into membranes composed of POPC/POPG (ratio of 9:1) and performing extensive AA-MD simulations (>50 μs).[263] The study revealed that TMH6 and TMH7 mediate translocation of a lipid from the intracellular to the extracellular side through three steps (Fig. 8D). First, the intracellular disruption of TMH6-E249–TMH7-K311 interaction and conformational switch of residue TMH7-Y306. Second, the changes observed in the first step lead to the increase of intracellular distance between TMH6 and TMH7 by ∼10 Å which allows influx of water molecules. The created hydrophilic environment favors the lipid to tilt and move toward the membrane center. Third, the distance between TMH6 and TMH7 in the membrane center is increased by ∼5 Å, thereby creating a continuous water channel enabling the lipid to completely flip. The lipid translocation event observed here occurs at a timescale of ∼33 μ, which is consistent with experimental lipid transfer, taking place at ∼100 μs or smaller.[269,275]

4.1.2 Membrane transporters and channels

Cell membranes permit the passage of various molecules such as water, ions, amino acids, sugars, and nucleotides, and most often make use of specialized proteins embedded within membranes for permeation. The membrane transport proteins exhibit both multipass TM topology (e.g., glucose transporters, GPCRs, monoamine transporter) or β-barrel topology (e.g., porin family, amyloid channels), as can been seen in Fig. 4. Most transport proteins are selective, i.e., they are permeated only by a single or a few chemically similar solutes. Membrane transporters and channels are typically grouped into two major classes of membrane proteins: (1) transporters strongly bind to the permeating solute and undergo a structural change to pass the solute across the membrane, leading to a slow permeation rate; (2) in contrast, channel proteins bind to molecules weakly, do not require a conformational change, hence allowing high permeation rates.

Over the last few years, several X-ray structures of transporters and channels have been solved and the rapid growth in the computing power has enabled MD simulations of complex biomolecules at timescales relevant to observe physiological phenomena. Although obtaining the time scale of entire transport process is still a major challenge, MD simulations have been successfully employed to describe the transition steps in various transport cycles. Here, we discuss results of three well documented transporters, lactose permease (LacY), xylose transporter (XylE), and human dopamine transporter (hDAT), and of the channel protein Kir2.1, whose functions are regulated by lipids.[276]

4.1.2.1 XylE/LacY transporters

MD simulations along with hydrogen–deuterium exchange mass spectrometry (HDX-MS) have proven to be robust methods to characterize dynamics of transporters in different membrane systems, such as liposomes, micelles, bicelles, and nanodiscs. Recently, Martens et al.,[277] combined these methods to understand how direct interactions with lipids modulate the conformational dynamics of secondary transporters, such as LacY and XylE. The two transporters (XylE, PDB code: 4JA4[278] and LacY, PDB code: 2CFQ[279]) in their inward-open conformation were embedded into bilayers, composed of DOPE/DOPG/CL (70/20/10 mol%) and DOPC/DOPG/CL (70/20/10 mol%) lipids, and AA-MD simulations were carried out to identify how lipids regulate the conformational switch at the molecular level. The simulations reveal that PE lipids localize between the TMH2 and TMH11, where they interacts with R84 and with the switch residue E153 (Fig. 9A). The interactions stabilize the transporter in the inward-open

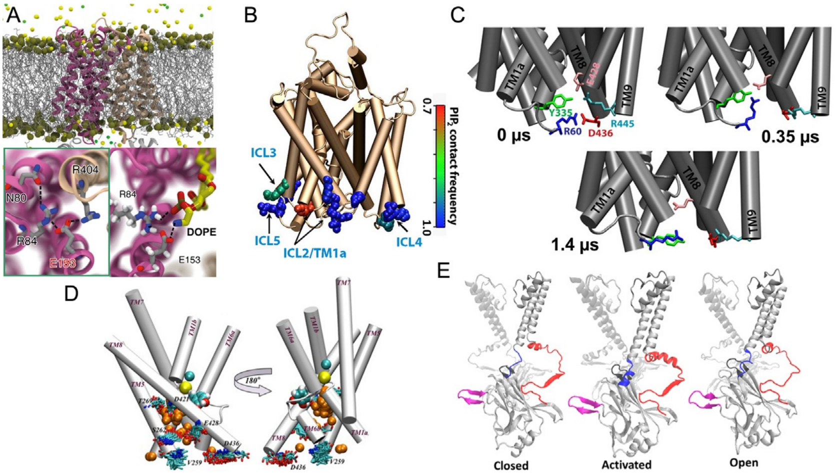

Fig. 9 Transporters and channel proteins. (A) DOPE–XylE interactions disrupt the charge-relay networks. In the *top panel*, snapshot showing XylE (PDB code: 4JA4[278]) in lipid membrane. Lipid acyl chains are shown as *lines*, phosphorus atoms rendered as *ochre spheres*, sodium and chloride ions as *yellow* and *green spheres*, respectively, and protein N- and C-domains colored as *pink* and *tan cartoon*, respectively. In the *bottom left panel*, close-up view of conserved network 1 connecting N- and C-domains stabilizes outward open state of XylE. In the *bottom right panel*, DOPE head group interacting with residues R84 and E153 disrupts network 1 connection and prevents association of TMH2 and 11. (B–D) hDAT undergoes PIP_2 mediated conformational shift to inward-open state. (B) Residues within 3 Å of PIP_2 lipid head group are rendered as *spheres*. TMHs, where PIP_2 aggregation is largest are labeled and shown by *black arrows*. (C) Snapshots showing initial formation of charge network (*top panel*) being disrupted by PIP_2 (*middle* and *bottom panel*) during the course of the MD simulation. (D) Snapshot depicting spontaneous inward release of sodium ion (*yellow sphere*) from its Na2 site and the release pathway is shown as *orange spheres*. The conformation of residues during the release process is displayed as *licorice*. The dopamine ligand and chloride ions are rendered as *VDW* and *cyan sphere*, respectively. The protein TMHs are shown as *white cartoon* and labeled, accordingly. (E) Regulation of Kir2.1 channel activity by PIP_2. PIP_2 mediated change in C-linker structure (*blue*) during conformational change from closed—activated—open states. Also, N-terminal and G-loop regions are displayed as *red* and *black*, respectively. *Panel A: reprinted with permission from Martens C, Shekhar M, Borysik AJ, et al. Direct protein-lipid interactions shape the conformational landscape of secondary transporters. Nat Commun. 2018;9(1):4151. Springer Nature. Copyright © 2018 Springer Nature. https://creativecommons.org/licenses/by/4.0/); Panel B–D: Reprinted with permission from Khelashvili G, Stanley N, Sahai MA, et al. Spontaneous inward opening of the dopamine transporter is triggered by PIP2-regulated dynamics of the N-Terminus. ACS Chem Neurosci. 2015;6(11):1825–1837, https://doi.org/10.1021/acschemneuro.5b00179, American Chemical Society. Copyright © 2015 American Chemical Society (https://pubs.acs.org/doi/10.1021/acschemneuro.5b00179). Further permissions related to the material excerpted should be directed to the ACS; Panel E: Reprinted with permission from Li J, Lü S, Liu Y, et al. Identification of the conformational transition pathway in PIP2 opening Kir channels. Sci Rep. 2015;1858(7, Pt. B):1610–1618, https://doi.org/10.1038/srep11289, Nature Publishing Group. Copyright © 2015, Macmillan Publishers Limited. (https://creativecommons.org/licenses/by/4.0/).*

state, preventing the conformational switch. In contrast, simulations in PC membrane shifts the conformation by closing the intracellular side. This conformation change is initiated by movement of TMH2/3 toward TMH10/11, which reduces the distance to ~9 Å in the PC bilayer, whereas in the PE bilayer it is at ~13 Å. Similar direct interactions between E139 and PE lipids were observed in LacY simulations. This study again highlights the role of lipids in regulating conformational changes.

4.1.2.2 Human dopamine transporter (hDAT)

Belonging to the neurotransmitter transport family, hDAT are responsible for clearance of dopamine neurotransmitter from the synaptic cleft into the cytosol, thereby terminating the dopamine signal. Increased activity or mutations in hDAT are associated with several disorders, such as depression, psychiatric and neurological disorders, and they also effect cognitive functions. To gain insights into the activation mechanism of hDAT, Khelashvili et al.,[280] performed extensive AA-MD simulations (>14 μs) on a full-length hDAT embedded in a lipid membrane composed of phosphatidylinositol 4,5-biphosphate (PIP_2) lipids. The study reveals the molecular details leading to the conformational shift from outward- to inward-open state (Fig. 9B and C). This shift also causes the release of a sodium ion from its Na2 site and the destabilization of dopamine from its S1 binding site (Fig. 9D). Closer examination of the membrane environment shows that PIP_2 mediates the association of the N-terminal segment and the intracellular loop 4 (ICL4) by forming electrostatic interactions with N-terminal residues K3, K5, K27, K35, R51 and with ICL4 residues H442, R443, H444. The N-terminal/ICL4 association stabilizes the inward-open state. To further validate the importance of PIP_2, additional simulations were carried out by replacing PIP_2 with POPE lipids. In absence of PIP_2 the stabilized N-terminal/ICL4 complex dissociates rapidly. The PIP_2-induced conformation shift and the transition mechanism reported for hDAT is similar to the activation mechanism of structurally similar Leucine transporter (LeuT).[281]

4.1.2.3 Inwardly rectifying potassium (Kir2.1) channel

Kir channels are found in several cell types, including neurons, kidney, cardiac, endothelial, blood cells, and they are involved in maintaining the membrane resting potential, cardiac excitability, and insulin release.[282,283] These channels allow more readily influx of potassium ions into the cells than outward-directed flux. The channel function is regulated by a conformational switch between the closed and open states. Moreover, several factors are involved in the process, including proteins and lipids. Among lipids, the negatively charged PIP_2 is required to activate all Kir channels. Apart from PIP_2, cholesterol is another important molecule involved in Kir regulation. Here, we discuss how PIP_2 and cholesterol regulates Kir2.1 activity. Li et al.[58] employed atomistic targeted MD (TMD) method to observe Kir2.1 channel opening from a closed state. By comparing X-ray structures of Kir channels, the authors recognized the conformational change of the C-linker (C-terminus region of the inner helix) loop to a helical conformation, and the structures further revealed PIP_2 binding sites on the C-linker. Guided by the hypothesis that PIP_2 could induce the conformational change of the C-linker, they carried out TMD on the C-linker residues (K185 to T192) with a goal to change the secondary structure from a loop to a helix. The change to the more rigid helical structure, which is stabilized by interactions with PIP_2, pulls the cytoplasmic domain (CD) ~5 Å toward the membrane, which enables contact with the TM domain. The first stage of TMD results in pushing the channel toward an active state. To achieve the fully active state, TMD was again applied to guide the C-linker–PIP_2 complex toward a partial helical conformation. The partially folded C-linker kinks, leading to a ~8 degrees rotation of the N- and C-termini, which shifts the CD downwards, thus, reaching a full open channel. The study reports all the keys necessary for the conformational shift, hence providing a detailed picture into PIP_2-induced opening of Kir channel.

Experimental studies have shown that cholesterol directly regulates the Kir2.1 channel activity by forming a network of specific interactions with the protein. However, the cholesterol binding sites were yet to be located. Avia et al.,[284] combined experimental as well as several computational methods such as docking, atomistic MD simulations and molecular mechanics Poisson–Boltzmann surface area (MM/PBSA) calculations to shed light on the cholesterol binding sites and their role in regulation of channel activity. Initial docking studies showed that cholesterol mainly binds at the TM domain interfaces at three typical binding poses. Two additional poses were located at the cytosolic domain. Subsequent MD simulations of Kir2.1 with bound cholesterol embedded in a lipid membrane revealed a rearrangement of cholesterol into two distinct binding sites. Site 1 corresponds to the center of the TM domain, whereas site 2 is near the cytosolic domain. To gain insights into the binding energies at these two sites, MM/PBSA approach was used, which indicated cholesterol to bind slightly stronger at the site 1.

The study concludes with the identification of two binding sites for cholesterol on Kir2.1 channel with large cholesterol flexibility within the two sites. Furthermore, mutation studies and functional analysis reveal that the identified binding sites may interfere with motion of the inner helix, which is required for keeping the channel in a closed state.

4.1.3 Glycoproteins

Glycosylation is one of the significant posttranslational modifications, during which glycans (oligosaccharides) are covalently added to an amino acid. Glycosylation occurs in all species. More than 50% of eukaryotic proteins undergo glycosylation,[285,286] with implications on various function and on protein activity.[287–291] Furthermore, all cells are covered by glycans necessary for cellular function.[286] Glycosylations are grouped into five classes[292]:

(1) *N-linked glycosylation*: Glycans are covalently linked to amide nitrogen of asparagine in the sequence N–X–S/T. Apart from proline or aspartic residues, X in the sequence can be any amino acid.

(2) *O-linked glycosylation*: Glycans are linked to hydroxyl group of serine or threonine residues, without a consensus sequence for O-glycan addition.

(3) *Phospho-serine glycosylation*: Glycans involves a linkage of sugars GlcNAc, xylose, mannose, and fructose to proteins by a phosphodiester bond.

(4) *C-mannosylation*: As an unusual type of glycosylation, sugar (mannose) is linked to a carbon atom rather than to amide or hydroxyl groups. Here, mannose is added to tryptophan in the sequence W–X–X–W where X can be any amino acid.

(5) *Glypiation*: Glycosylphosphatidylinositol (GPI) is formed, anchored to a lipid by glycan chain.[292]

Here, we focus on the membrane receptor toll-like receptor 4 (TLR4) which is glycosylated with a core N-linked glycan ($GlcNAc_2Man_3$). Mobarak et al.[226] carried out microsecond timescale simulations of LPS bound to glycosylated TLR4 complex, embedded in asymmetric membrane composed of CHOL/SM/GluCer/PC lipids (45/25/10/20 mol%) in the outer leaflet and CHOL/PS/PE/PC lipids (35/20/20/25 mol%) in the inner leaflet. To study the effect of Glucosylceramide (GluCer) on the receptor, additional simulations were performed without GluCer in the outer leaflet and the composition was adjusted to CHOL/SM/PC (45/35/20 mol%) in the outer leaflet and the inner leaflet lipids were unmodified. The simulations showed that LPS induced tilting of the TLR4 extracellular domain, however, tilting was reduced and TLR4 was stabilized in membrane containing GluCer. Quantification of tilt angles showed that the LPS/TLR4 complex tilted by ~33 and 57 degrees in the presence and absence of GluCer, respectively (Fig. 10A). However, in the absence of LPS, TLR4 only tilted by 15 and 19 degrees in the presence and absence GluCer, respectively. It was unlikely that direct interactions between GluCer and TLR4 would reduce tilting since the GluCer head group is small and uncharged, whereas TLR4 is a negatively charged protein. The authors speculated that the reduced tilting could be due to altering of the membrane properties by GluCer. A subsequent analysis revealed that

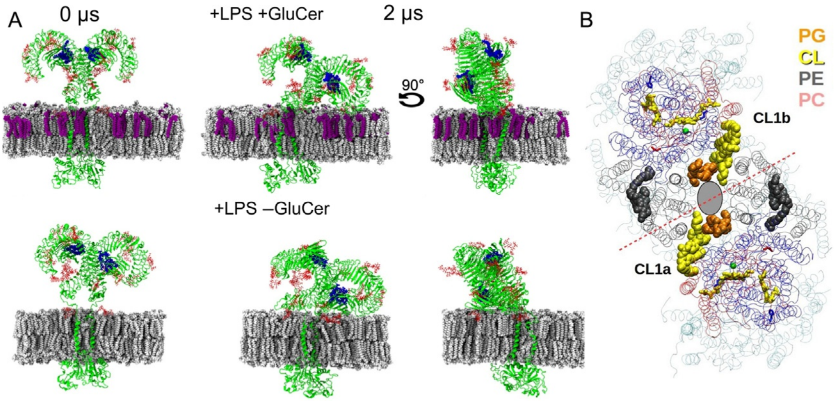

Fig. 10 Glycoprotein and respiratory complex IV. (A) Change in TLR4 dimer orientation. Snapshots show the TLR4 orientation at time 0 μs (*left panels*) and at time 2 μs (*middle* and *right panels*). Presence of GluCer (*purple*) in the membrane causes a change in the orientation of TLR4 extracellular domain (*green*). In the TLR4 dimer structure, LPS and glycans are *colored blue* and *red*, respectively. Rest of the membrane lipids are colored white. (B) X-ray structure of complex IV, Cytochrome c oxidase (PDB ID: 2DYR[293]) bound to PG, CL, PE, PC lipids (VDW representation, see legend for *color code*). Snapshot showing view of dimer structure from inter membrane space and the subunits I, II, and III are displayed as *blue*, *red*, and *gray ribbons*, respectively. The two monomers are separated by *red dotted lines* and the *gray filled circle* indicates empty region between the two monomers. Other structural components such as heme (*yellow licorice*), copper ion (*green spheres*), and some charged/polar residues (*licorice*) are shown as well. *Panel A: Reprinted with permission from Mobarak E, Håversen L, Manna M, et al. Glucosylceramide modifies the LPS-induced inflammatory response in macrophages and the orientation of the LPS/TLR4 complex in silico. Sci Rep. 2018;8(1):13600, Springer Nature. Copyright © 2018 Springer Nature (https://creativecommons.org/licenses/by/4.0/); Panel B: Reprinted with permission from Malkamäki A, Sharma V. Atomistic insights into cardiolipin binding sites of cytochrome c oxidase. Biochim Biophys Acta. 2019; 1860(3):224–232, 10.1016/j.bbabio.2018.11.004. Elsevier. Copyright © 2019, Elsevier (https://creativecommons.org/licenses/by/4.0/).*

the electrostatic potential of the membrane increased by 30% in presence of GluCer. Thus, the authors concluded that repulsive interactions between the LPS/TLR4 complex and the membrane reduced the tilting of LPS/TLR4 in the presence of GluCer. In addition, the authors observed that the effect of tilting on the extracellular side translated to the TM domains, where the conformation of the TM helix was altered in absence of GluCer, further emphasizing the stabilizing effect of GluCer on the LPS/TLR4 complex.

4.1.4 Mitochondrial membrane protein

Mitochondria are referred to as powerhouse of the cell due to synthesis of the energy carrier ATP.[295] Apart from ATP synthesis, mitochondria are required for the production of other molecules, such as NADH (nicotinamide adenine dinucleotide), GTP (guanosine triphosphate), amino acids, and lipids.[296,297] Mitochondria carry out many fundamental process, for instance in cellular respiration, cell and calcium signaling, as well as during stress signaling.[298–300] Thus, dysfunction of mitochondrial activity leads to several human diseases.[301] Mitochondria consist of a porous outer membrane and a tightly regulated inner membrane. At the inner membrane, ATP synthesis and oxidative phosphorylation take place in presence of membrane protein complexes. The complexes are (1) complex I (NADH:ubiquinone oxidoreductase), (2) complex II (succinate dehydrogenase), (3) complex III (cytochrome c reductase), and (4) complex IV (cytochrome c oxidase).[301] The structures of these complexes have been solved experimentally. In combination with computational techniques, the molecular details of electron transport are well-explored. However, how lipids regulate the activity of these complexes at the atomistic level much less understood. CL is one of the key components of the inner mitochondrial membrane, constituting to about 20% of the total lipid composition. CL has a highly charged small head group with four hydrocarbon tails (Fig. 2A).[302,303] All respiratory complex structures reveal CL binding sites.[304] Experiments have shown that the removal of CL reduces the activity of cytochrome c oxidase (CcO) by 50%,[305] whereas the activity is only mildly affected by the removal of PC or PE lipids. Though the effect of lipids on the CcO activity is well established, little is understood on the lipids' modulatory mechanism. Here, we discuss results from a recent study, which provides atomistic insights into the role of the mitochondrial membrane lipid CL in the functioning of the terminal enzyme complex IV, which is essential for the energy metabolism.

Malkamäki et al.[294] performed extensive AA-MD simulations (18 μs in total) of the bovine cytochrome c oxidase (CcO) dimer to gain insights into the dynamics of CL. The monomeric and dimeric structures were embedded into a lipid membrane composed of POPC/POPE/CL (ratio of 5:3:2). The X-ray structure (PDB code: 2DYR[293]) revealed that each CcO monomer has two CL binding sites, where one of the sites (site 2) is located at the interface of the two CcO monomers, suggesting a possible role in stabilizing the dimer structure (Fig. 10B). During MD simulations, CL occupied the crystallographically known site 1 throughout the simulations; however, at the buried site 2, CL was only weakly bound and dissociated within 1 μs. The dissociation of CL on site 2 occurred first by a movement of the CL head group away from the site, and then by tails, suggesting stronger interactions between the CL tails and protein hydrophobic interface. In contrast, CL at site 1, where it binds more strongly, is stabilized by strong ionic interactions. Additional simulations in the absence of CL at buried site 2, but with crystallographic bound PG/PE, revealed no effect on the stability of the dimer structure; however, removal of CL from site 1 not only destabilized the protein structure but also perturbed the strongly bound PG and PE lipids from their respective binding sites. This destabilization would potentially lead to loss of enzyme function. Thus, these simulation results provide an explanation at the atomistic level for the experimentally observed activity loss of CcO upon removal of CL.

4.2 Atomistic simulations of membrane-associated proteins

4.2.1 Amyloids

4.2.1.1 Amyloid β (Aβ) peptide

Alzheimer's disease (AD) characterized by loss of neuronal cells is primarily linked to neurofibrillary tangles and neuritic plaques.[306,307] Neurofibrillary tangles are associated with abnormal accumulation of tau proteins, whereas neuritic plaques (amyloid plaques) are associated with the aggregation of Aβ peptide.[308] So far, no consensus hypothesis of the molecular cause of AD has emerged, however, due to the presence of Aβ peptide in amyloid plaques, Aβ is widely accepted as a key molecule in AD. Aβ exists in two isoforms, Aβ_{40} and Aβ_{42}, with the latter being more prone to aggregation and more toxic.[309] Furthermore, several studies have shown that Aβ oligomers and not the fibrils are the causative agent of AD.[310–312] Since, Aβ peptide is a cleaved product of the transmembrane amyloid precursor protein (APP), it is also widely accepted that Aβ interactions with the membrane could play a role in the formation of toxic oligomers.[313–318] In spite of experimental and computational studies exploring and proposing several possible mechanisms toward Aβ induced cell toxicity, it is still difficult to draw any conclusion on the neurotoxicity mechanism. Here, we discuss findings from computational studies of Aβ-membrane interactions with a focus on lipids.

Poojari et al.[319,320] using atomistic MD simulations (>6 μs) have extensively investigated the behavior of monomeric Aβ_{42} in helical and β-sheet conformations and tetrameric Aβ_{42} in β-sheet conformations in POPC, DPPC, and POPG bilayers. In addition, it was investigated how various Aβ_{42} mutants (K16M, E22G, D23G, and K28M) affect membrane stability. These simulations showed that the stability of the peptide inside the membrane is influenced by the degree of lipid acyl chain unsaturation and by the head group charge. Peptides were most stable in POPC bilayers, whereas pronounced peptide instability was observed in DPPC and POPG bilayers. Simulations also revealed that the β-sheet tetrameric structure increases water permeation into membranes (Fig. 11A), indicating that, indeed, Aβ_{42} oligomers and not monomers are the toxic species. Mutation studies revealed that the "Arctic-type" D23G mutant exhibits an increased ability to disrupt membranes as compared to other studied mutants. However, neither wild type nor mutant monomers leave the membrane interior in the simulated time.

In order to understand how Aβ gets released from the membrane, Lemkul et al.[321] carried out atomistic MD simulations of Aβ_{40} partially embedded (residues 29–40 inside the membrane) in POPC, POPS, POPC/POPE, POPC/SM/CHOL/GM1, and POPC/SM/CHOL membranes. The partially inserted Aβ_{40} peptide anchors itself to the membrane through hydrogen bonding and electrostatic interactions with the lipid head groups. The interactions stabilize the peptide at the initial inserted depth in POPC, POPS, POPC/POPE, and POPC/SM/CHOL membranes.

In membranes containing GM1 lipid, Aβ_{40} C-terminal residues (29–40) lose their α-helix structure and become more disordered (Fig. 11B). The C-terminal residues approach the polar interface were they form stable interactions with the GM1 sugars, glucose (Glc) and N-Acetylneuraminic acid (Neu5Ac). The interactions would eventually promote release of the peptide from the membrane interior, thereby exposing aggregation-prone hydrophobic regions of the peptide. The results provide mechanistic insights into the GM1-mediated release of membrane inserted Aβ_{40}.

Membrane mediated aggregation and disruption of cell membrane is one of the hypotheses linked to Aβ_{42} induced toxicity. Neuronal cell membranes are complex with several lipid species and vary in head group charge, size and saturation/unsaturation level of acyl tails. To resolve how different lipids

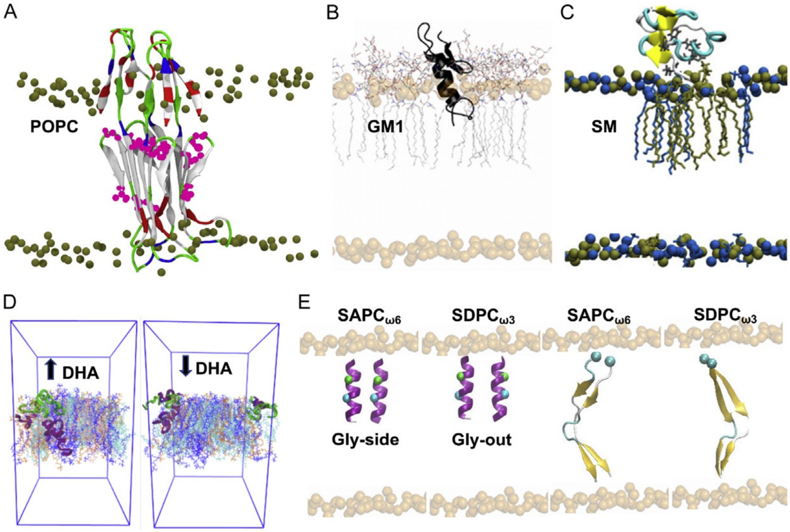

Fig. 11 Amyloid beta ($A\beta$) peptide. (A) $A\beta_{42}$ β-sheet tetramer increasing water translocation by perturbing the POPC head group arrangement. *Pink spheres* refer to peptide residues involved in HB formation with water molecules. POPC phosphorous atoms are shown as *tan spheres* and lipid tails not shown for clarity. (B) GM1 lipids inducing the release of $A\beta_{40}$ peptide from the membrane interior. GM1 lipids are rendered as *lines*, phosphorous atoms as *transparent orange spheres* and rest of the lipids are not shown for clarity. (C) SM mediated β-sheet formation in the $A\beta_{42}$ peptide termini. SM lipids below the peptide are shown as *blue licorice*. For SM lipids further away, only the phosphorus atoms as *blue sphere* is displayed. POPC lipids are shown in tan. Rest of the lipids are not shown for clarity. (D) High DHA (healthy brain) content in the membrane favors deeper absorption of both $A\beta_{1\text{–}28}$ (*green*) and $A\beta_{26\text{–}40}$ (*purple*) peptides, whereas as low DHA content (AD brain) prevents deep absorption and promotes aggregation of the peptides into toxic oligomers on the membrane surface. (E) SAPC$_{\omega6}$ and SDPC$_{\omega3}$ membranes stabilize the helical dimer structure of $A\beta_{29\text{–}42}$ with Gly-side and Gly-out orientations, respectively. However, with β-sheet dimer structures, SDPC$_{\omega3}$ reduces the β-sheet content. The change in orientation and secondary structure observed here is not sufficient to explain the SAPC$_{\omega6}$ triggered increase in $A\beta$ production. *Panel A: Reprinted with permission from Poojari C, Kukol A, Strodel B. How the amyloid-β peptide and membranes affect each other: an extensive simulation study. Biochim Biophys Acta Biomembr. 2013;1828(2):327–339, https://doi.org/10.1016/j.bbamem.2012.09.001, Elsevier. Copyright © 2012 Elsevier B.V. All rights reserved, Elsevier. (https://creativecommons.org/licenses/by/4.0/); Panel B: Reprinted with permission from Lemkul JA, Bevan DR. Lipid composition influences the release of Alzheimers amyloid* β*-peptide from membranes. Protein Sci. 2011;20(9):1530–1545, https://doi.org/10.1002/pro.678. Copyright 2011* The Protein Society *(https://creativecommons.org/licenses/by/4.0/); Panel C: Reprinted with permission from Owen MC, Kulig W, Poojari C, Rog T, Strodel B. Physiologically-relevant levels of sphingomyelin, but not GM1, induces a* β*-sheet-rich structure in the amyloid-*β*(1-42) monomer. Biochim Biophys Acta Biomembr. 2018;1860(9):1709–1720, https://doi.org/10.1016/j.bbamem.2018.03.026, Elsevier. Copyright © 2018 Elsevier B.V. (https://creativecommons.org/licenses/by/4.0/); Panel D: Reprinted with permission from Ntarakas N, Ermilova I, Lyubartsev AP. Effect of lipid saturation on amyloid-beta peptide partitioning and aggregation in neuronal membranes: molecular dynamics simulations. Eur Biophys J. 2019;48(8):813–824, https://doi.org/10.1007/s00249-019-01407-x, Springer Nature. Copyright © 2019 The Author(s). (https://creativecommons.org/licenses/by/4.0/); Panel E: Reprinted with permission from Lu Y, Shi XF, Nguyen PH, Sterpone F, Salsbury FR, Derreumaux P. Amyloid-*β*(29-42) dimeric conformations in membranes rich in omega-3 and omega-6 polyunsaturated fatty acids. J Phys Chem B. 2019;123(12):2687–2696, https://doi.org/10.1021/acs.jpcb.9b00431, American Chemical Society. Copyright (2019) American Chemical Society.*

affect Aβ_{42} structure, Owen et al.[322] carried out AA-MD simulations of Aβ_{42} on membranes composed of POPC/CHOL (70/30 mol%), POPC/CHOL/SM (30/40/30 mol%) and POPC/CHOL/GM1 (70/25/5 mol%). The simulations provide molecular insights into the role of cholesterol (CHOL), sphingomyelin (SM) and ganglioside (GM1) lipids in conversion of Aβ_{42} structure to toxic oligomers. The presence of SM, renders membrane highly rigid, which in turn reduces interactions between highly disordered N-terminus residues of Aβ_{42} and the membrane. The only interaction observed is between residue R5 and SM, which prevents Aβ_{42} from bouncing back to the aqueous solution. The lack of interactions promotes β-sheet formation in the N-terminus, thus, the final topology is a conformation with central loop connecting N- and C-terminal β-sheets (Fig. 11C). This final structure resembles experimentally known Aβ fibril structure. In comparison, GM1 has small effect on the membrane property but does not induce secondary structure change. The membranes with or without GM1 had no effect on the structure of the Aβ_{42}. Thus, the results provide new insight into the role of SM ceramide in altering membrane property and in formation of toxic Aβ_{42} oligomers.

Apart from the lipids discussed above, neuronal membranes also contain large amount of polyunsaturated fatty acids (PUFAs) such as docosahexaenoic acid (DHA, 22:6). AD has been associated with reduction of DHA lipids from 23% in normal brain to 12% in AD brain.[325–327] In vitro studies have shown that DHA inhibits Aβ_{42} fibril formation.[328] To better understand the inhibitory role of DHA, Ntarakas et al.,[323] carried out MD simulations of Aβ peptide fragments Aβ_{1-28} and A$\beta_{26\text{-}40}$ in single component bilayers (DMPC– 14:0,14:0 or SDPC– 18:0,22:6) and in mixed bilayers (DSPE– 18:0,18:0, DDPE– 22:6,22:6, DPPC– 16:0,16:0, DOPC– 18:1,18:1) with varying composition. The mixed bilayer is divided into two types based on lipid composition. The mixed bilayer with high fraction of DHA is referred to as "normal bilayer" and the other bilayer with low fraction of DHA and high fraction of saturated lipids is referred to as "AD bilayer" (Fig. 11D). The simulation results from single component bilayer show that in DMPC bilayer, both the Aβ fragments prefer to stay on the membrane surface. In contrast, in presence of 18:0–22:6 PC, Aβ_{1-28} partially enters the membrane and the Aβ_{26-40} fragment even fully inserts into the membrane. The behavior of the Aβ fragments in DMPC bilayer is consistent with the experimental data.[329] Similar trends were observed for Aβ interaction when studied in mixed bilayer. The Aβ_{1-28} fragment fully enters the normal bilayer with high fraction of DHA and stays on the membrane surface of an AD bilayer. However, the A$\beta_{26\text{–}40}$ fragment penetrates both the normal and AD bilayers. The authors next looked into the aggregation propensity of these peptides, and they observed that both Aβ fragments clustered on the membrane surface in DMPC and AD bilayer, but they were more dispersed in normal bilayer. Thus, the study suggests the presence of DHA to favor internalization of Aβ peptide, which in turn prevents aggregation and formation of toxic oligomers on the membrane surface.

In another related study using PUFAs, Lu et al.[324] looked into the role of omega-3 (ω3) and omega-6 (ω6) PUFAs in stabilizing A$\beta_{29\text{–}42}$ dimer structures by performing extensive AA-MD simulations (~7 μs). The A$\beta_{29\text{–}42}$ dimers in both helical and β-sheet conformations were fully preinserted into a bilayer of POPC, 1-stearoyl-2-arachidonoyl-*sn*-glycero-3-phosphocholine (SAPC$_{\omega 6}$ 18:0,20:4) and 1-stearoyl-2-docosahexaenoyl-*sn*-glycero-3-phosphocholine (SDPC$_{\omega 3}$ 18:0,22:6). For the β-sheet conformation, an additional simulation was carried with the peptide fully inserted into a mixed bilayer composed of POPC/SAPC/SDPC lipids. The simulations show both SDPC$_{\omega 3}$ and SAPC$_{\omega 6}$ to stabilize the helical dimer structure (80% α-helix) with a parallel orientation and reorient the G33–X–X–X–G37 motif with SDPC$_{\omega 3}$ favoring Gly-out and SAPC$_{\omega 6}$ favoring Gly-side orientation (Fig. 11E). However, SAPC$_{\omega 6}$ disorders the β-sheet dimer by reducing its β-sheet content from 59% to 44% and inducing α-helix conformation by 7% (Fig. 11E). SDPC$_{\omega 3}$ and POPC bilayers behave similarly with no large effect on the β-sheet dimer. However, in a mixed membrane, the β-sheet dimer is stabilized with high β-sheet content (~63%), thus SDPC$_{\omega 3}$ and POPC lipids suppress the individual effect of SAPC$_{\omega 6}$ on the peptide. The study demonstrates how variation in PUFAs influence oligomerization of Aβ inside membranes.

4.2.1.2 The human islet amyloid polypeptide (hIAPP)

The hIAPP or amylin is a small 37 residue peptide secreted by the pancreatic β-cells. hIAPP deposits are seen in 90% of the patients with type 2 diabetes (T2D) and are known to induce cytotoxicity and β-cell death. hIAPP monomers are not toxic to cells, however, they aggregate into toxic oligomers which disrupt the cell membrane. Several mechanisms have been proposed to explain hIAPP-induced cell toxicity, namely, (1) by the formation of channel structures, (2) by extraction of lipids, and (3) by membrane thinning. However, the exact membrane disruption mechanism is still not clear. Here, we present results from AA-MD simulations of hIAPP-membrane interactions and focus mainly on how different lipids affect hIAPP binding, orientation, aggregation, and insertion into membranes which provide insight into the membrane disruption mechanism.

Jia et al. and Qian et al.[330–332] investigated the initial binding of hIAPP monomers to zwitterionic POPC and anionic POPG bilayers using AA-MD simulations. As a starting structure, they used hIAPP peptide in α-helical conformation and placed the peptide 1.4 nm above the POPC or POPG membrane surface. Simulations show that hIAPP adopts four different orientations in POPC membrane. N-terminal residues localize at the hydrophilic head group region of the lipid, whereas the C-terminal residues penetrate deep into the membrane (Fig. 12A). In case of simulations with POPG membrane, the peptide adopts a single, surface-bound orientation. The lack of membrane penetration exposes the aggregation-prone C-terminal residues 20–37 to peptide–peptide interactions. Analysis of membrane properties revealed that the hIAPP monomer has a negligible effect on the membrane, indicating that the experimentally observed membrane disruption is caused by oligomeric structures and not by monomers.

Similarly, Dignon et al.,[333] carried out AA-MD simulations of hIAPP monomers with DOPC, DOPS and DOPC/DOPS membranes using the parallel tempering method. This study also allows a comparison with simulations in POPC or POPG membranes described above. The simulations generated a large ensemble of structures differing between the three membranes. The α-helical content is reduced and changed in DOPS and DOPC membranes, respectively, whereas in mixed membrane the α-helical content is increased (Fig. 12B). Also, the insertion of the residues 15–28 was same in DOPC membranes but deeper in DOPC/DOPS membranes. Here, the shallow insertion in the DOPS membrane was observed possibly due to a loss of secondary structure. No details were provided regarding the membrane structure, probably due to negligible effect of the peptide on the membrane property.

The above studies present case studies of effects of oligomeric structures on membrane properties. The formation of hIAPP dimers is the first step toward the formation of large oligomers. Zhang et al.[334] carried out AA-MD simulations of hIAPP dimers preinserted into POPG bilayer. During simulation, the dimers inserted deep into the membrane with residues K1 anchoring to the lipid head group (Fig. 12C). The interaction perturbs the phosphorous atoms around the dimer in both, the upper and the lower leaflets, which results in a reduction of membrane thickness in close proximity to the dimer. Analysis of the lipid order parameters revealed that

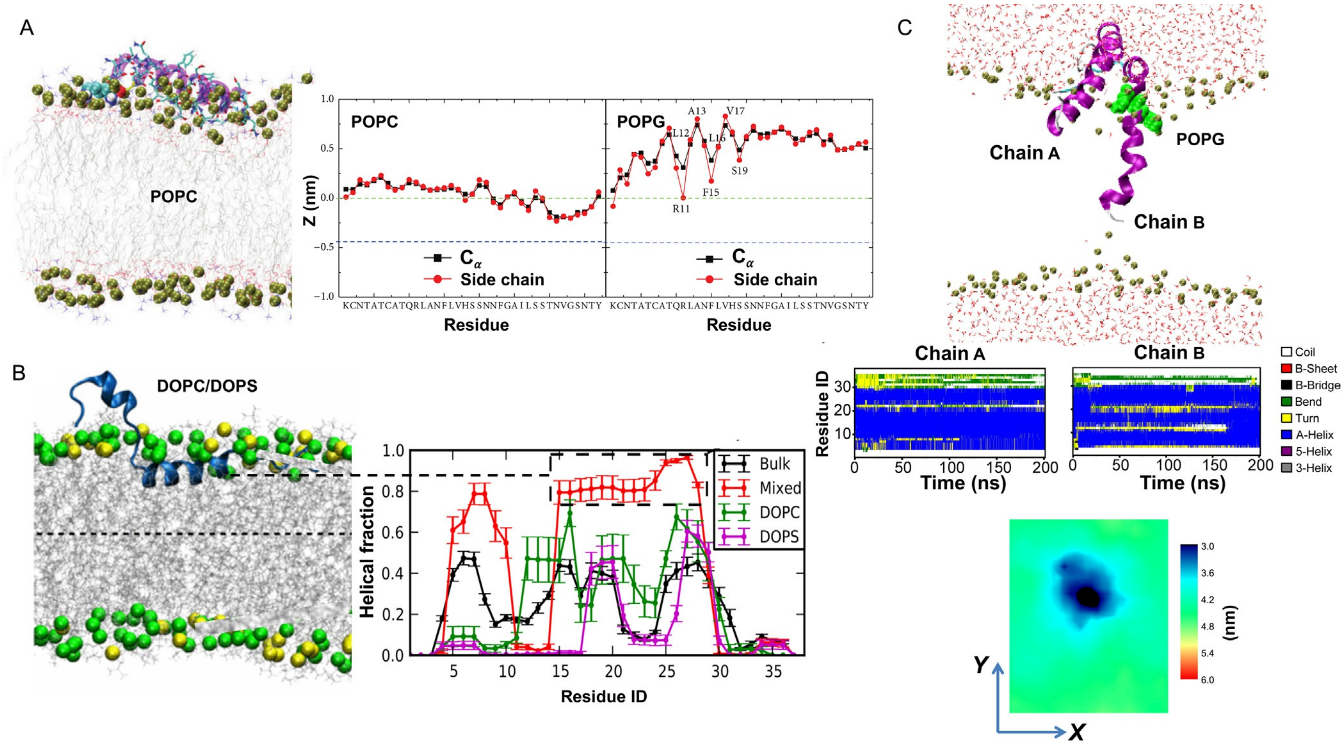

Fig. 12 See legend on next page.

the hIAPP dimer also decreases the ordering of carbon atoms close to the head group. During an additional simulation, the order parameters were also decreased at carbon atoms 5–12, close to the membrane center. These results provide evidence for a membrane disruption ability of hIAPP, and they also suggest dimers as the minimal aggregate required to alter membrane properties.

To understand how hIAPP monomers aggregate into toxic oligomers, Christensen et al.[172] carried out AA-MD simulations starting from a monomer already bound to the membrane surface. The monomeric system was multiplied to have four peptides on a membrane composed of divalerylphosphatidylserine (DVPS, 30%) and zwitterionic divalerylphosphatidylcholine (DVPC, 70%) lipids. To enhance the diffusion of lipids and peptides, the highly mobile membrane mimetic (HMMM) model was utilized. The simulations suggested that self-assembly takes place in the following order (Fig. 13A): (1) the monomers diffuse on the membrane surface with N-terminal residues (K1 and R11) anchoring the peptide to the membrane; (2) the aromatic residues (F15 and F23) in the central region of the peptide initiate peptide–peptide interactions. For the self-assembly to start, the interactions between peptide and membrane observed in step 1 must break, leading

Fig. 12 The human islet amyloid polypeptide (hIAPP). (A) Snapshot showing side view of hIAPP monomer interacting with POPC bilayer. The plot shows insertion depths for hIAPP Cα and side chain atoms in POPC and POPG bilayers. (B) Mixed bilayer containing DOPC/DOPS lipids allow deeper insertion of the peptide and stabilizes the helical structure from residues 15–28 of hIAPP. The plot shows reduction in helical content in pure DOPC and pure DOPS bilayers. (C) Final snapshot of hIAPP dimer in POPG bilayer. *Top*: The dimers (chain A and chain B) penetrate deeper into the bilayer with helical content preserved. Residues from 18 to 20 are rendered as *green VDW spheres* and lipid tails are not shown for clarity. *Center*: Plot showing secondary structure content for chain A and B peptides. α-helical content is preserved in both the peptides. *Bottom*: Plot showing reduced bilayer thickness in vicinity of the dimer. *Panel A: Reprinted with permission from Qian Z, Jia Y, Wei G. Binding orientations and lipid interactions of human amylin at zwitterionic and anionic lipid bilayers. J Diabetes Res. 2016;2016:1–13, Hindawi Publishing Corporation. Copyright © 2016 Zhenyu Qian et al. (https://creativecommons.org/licenses/by/3.0/); Panel B: Reprinted with permission from Dignon GL, Zerze GH, Mittal J. Interplay between membrane composition and structural stability of membrane-bound hIAPP. J Phys Chem B. 2017;121(37):8661–8668, https://doi.org/10.1021/acs.jpcb.7b05689, American Chemical Society. Copyright (2017) American Chemical Society; Panel C: Reprinted with permission from Zhang Y, Luo Y, Deng Y, Mu Y, Wei G. Lipid interaction and membrane perturbation of human islet amyloid polypeptide monomer and dimer by molecular dynamics simulations. PLoS ONE. 2012;7(5):1–10, https://doi.org/10.1371/journal.pone.0038191, Public Library of Science. Copyright © 2012 Zhang et al. (https://creativecommons.org/licenses/by/4.0/).*

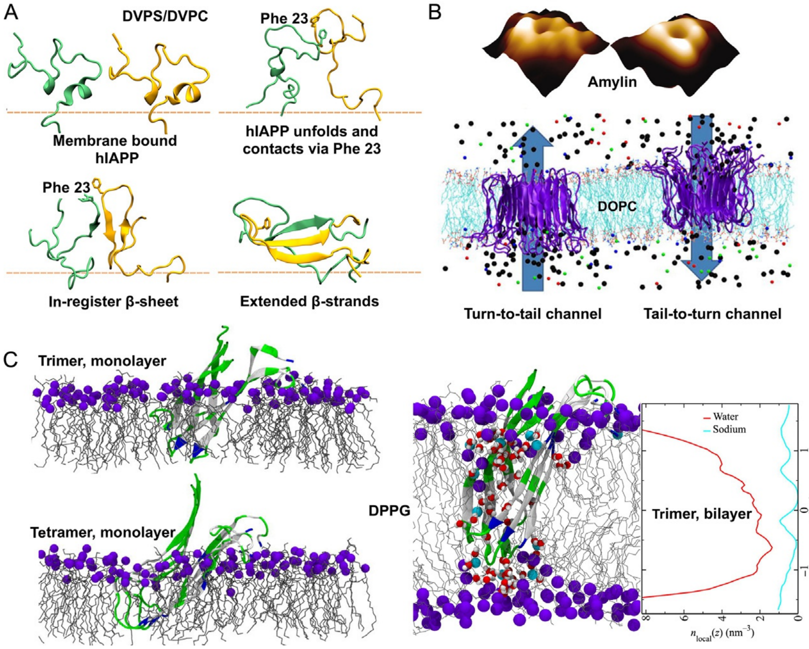

Fig. 13 Conventional MD and HMMM simulations of hIAPP. (A) Snapshots 1–4 represent various structural changes the peptides undergo in the formation of stable β-sheet dimers on the DVPS/DVPC membrane surface. The *orange dashed lines* indicate phosphorus atoms of the lipids. (B) Oligomerization of hIAPP into toxic ion channel structures. *Top*: Atomic force microscopy (AFM) image of amylin showing channel-like structures. *Bottom*: Double-annular-like ion channels (resembling AFM images) with β-strand-turn-β-strand topology embedded into DOPC bilayer. MD simulations show unregulated conductance of ions across the ion channels. (C) hIAPP protofibril structures in DPPG membrane. *Left*: Most populated central cluster structure of hIAPP trimer and tetramer in DPPG monolayer. *Right*: hIAPP trimer in fully membrane inserted state adopts a β-sandwich structure which allows influx of water and sodium ions (*cyan spheres*). The plot indicates the density of water and sodium ions inside the membrane. *Panel A: Reprinted with permission from Christensen M, Skeby KK, Schiøtt B. Identification of key interactions in the initial self-assembly of amylin in a membrane environment. Biochemistry. 2017;56(36):4884–4894, https://doi.org/10.1021/acs.biochem.7b00344, American Chemical Society. Copyright (2017) American Chemical Society; Panel B (Top): Reprinted with permission from Quist A, Doudevski I, Lin H, et al. Amyloid ion channels: a common structural link for protein-misfolding disease. Proc Natl Acad Sci. 2005;102 (30):10427–10432, https://doi.org/10.1073/pnas.0502066102, United States National Academy of Sciences. Copyright (2005) National Academy of Sciences, USA; Panel B (Bottom): Reproduced from Zhao J, Hu R, Sciacca MFM, et al. Non-selective ion channel activity of polymorphic human islet amyloid polypeptide (amylin) double channels. Phys Chem Chem Phys. 2014;16:2368–2377, https://doi.org/10.1039/C3CP53345J, with permission from the PCCP Owner Societies 2014. Royal Society of Chemistry (United Kingdom). Permission conveyed through Copyright Clearance Center, Inc.; Panel C: Reprinted with permission from Poojari C, Xiao D, Batista VS, Strodel B. Membrane permeation induced by aggregates of human islet amyloid polypeptides. Biophys J. 2013;105(10):2323–2332, https://doi.org/10.1016/j.bpj.2013.09.045, Elsevier. Copyright © 2013 Biophysical Society. Published by Elsevier Inc. All rights reserved. (https://creativecommons.org/licenses/by/4.0/).*

to a partial unfolding of the secondary structure; (3) the initial aromatic interactions allow the peptide segment 22-NFGAIL-27 to form stable interactions; (4) self-assembly induces β-sheet formation in segments 14-NFLVH-18 and 25-AILSST-30, which are involved in intra- and inter-peptide interactions. In these simulations, the H18 residue was modeled as electroneutral during the self-assembly process, since a charged H18 residue would have increased the interaction with the PS lipid head group, thereby stabilizing the secondary structure and repelling the peptides, which would inhibit the self-assembly process. This study highlights the role of lipids in aggregation and provides atomistic insight into the formation of oligomer structures.

The membrane-dependent self-assembly of hIAPP to oligomers is hypothesized to allow the formation of ion channel/pores in membranes thereby inducing cell toxicity. It is computationally challenging to simulate the spontaneous hIAPP oligomerization and ion channel formation in a membrane. However, to understand the mechanism of how oligomers transfer ion across the membrane, Zhao et al.[335,336] used the β-strand-turn-β-strand (U-turn) motif as starting topology and modeled several single and double annular-like ion channels resembling the channel morphology observed with atomic force microscopy (AFM)[337] (Fig. 13B). The channels were fully inserted into DOPC bilayer for studying the ion conductivity. MD simulations revealed a loss of the β-sheet secondary structure, which destabilized the channels into unstable loosely packed subunits. The unstable channel structures allowed unregulated flow of ions across the bilayer which would lead to ion imbalance and toxicity. These studies provided a first view of channel structures and their role in toxicity.

The unstructured toxic oligomers are dynamic and can transform to more ordered, fibril-like β-sheet rich structures called protofibrils, which are also toxic to cells. The structure of a mature fibril in its β-strand-turn-β-strand topology has been solved using solid-state NMR by Tycko's[339] and Langen's[340] groups. The structure provides the basis to construct and study protofibrils in a membrane environment. To study how protofibrils orient in a membrane, Xiao et al.[341] combined surface-selective sum frequency generation (SFG) spectroscopy and quantum chemistry techniques. These authors noticed that the protofibril is partially inserted into dipalmitoylphosphatidylglycerol (DPPG) monolayer with an tilt angle of 48 degrees. To check for the stability of protofibrils in lipid membranes, Poojari et al.,[338] carried out atomistic simulations of protofibrils (trimer and tetramer structures) partially inserted into DPPG monolayers and bilayers at an tilt angle of 48 degrees (Fig. 13C). The simulations show protofibrils to adopt a tilt angle of 40 degrees in DPPG monolayers, which is close to 48 degrees measured in experiments. However, in bilayers the protofibrils penetrate deep into the membrane with an angle of 60 degrees. The protofibril inside the membrane is stabilized by close interactions with the lipid head groups. Furthermore, trimer structures in both monolayer and bilayer were structurally less stable when compared to tetramer due to increased flexibility of the outer β-strands. The flexible trimer structure distorts into a β-sandwich structure which further perturbs the membrane integrity, thereby allowing the permeation of water and sodium ions. This study revealed for the first time key details of protofibril structures, such as the stability and the orientation of protofibril in lipid membranes, the formation of β-sandwich structure by protofibrils, membrane disruption, and conductance of water and ions.

4.2.1.3 α-synuclein (aSyn)

aSyn is a presynaptic neuronal protein linked to Parkinson's disease (PD).[342] The 140-residue protein is divided into three domains based on their function: (1) residues from M1–K60 are rich in lysine residues and are required for binding to membrane; (2) residues E61–V95 form the central "nonamyloid-β component" (NAC) segment of the protein and also contains the hydrophobic motif necessary for protein aggregation, and (3) residues K96–Ala140 involved in interactions with proteins, metal ions, small molecules, etc.[343–345] So far, two monomeric structures of aSyn (PDB code: 1XQ8,[346] 2KKW[347]) have been solved in sodium dodecyl sulfate (SDS) and sodium lauroyl sarcosine (SLAS) micelles. Recently, using cryoEM, Li et al.,[348] solved the structure of aSyn fibril in rod and twister polymorphs (PDB code: 6CU8[348]) at 3.7 Å resolution. Unlike Aβ and hIAPP, computational studies of aSyn–membrane interactions are limited. Nevertheless, we aim to discuss the key results from AA simulations of aSyn in membrane environment.

Experiments and AA simulations were initiated to probe the membrane-penetrating ability of the N-terminal residues.[349] Here, a short-length aSyn$_{1-15}$ was used for simulations in a POPA/POPC membrane, and the studies showed that residues M1, W4, L8 penetrate deep into the membrane, whereas residues D2, K6, S9, K10, and E13 remain solvent-exposed (Fig. 14A). These studies confirm that the N-terminal residues bind to the membrane. Further, aSyn–membrane interactions were investigated in

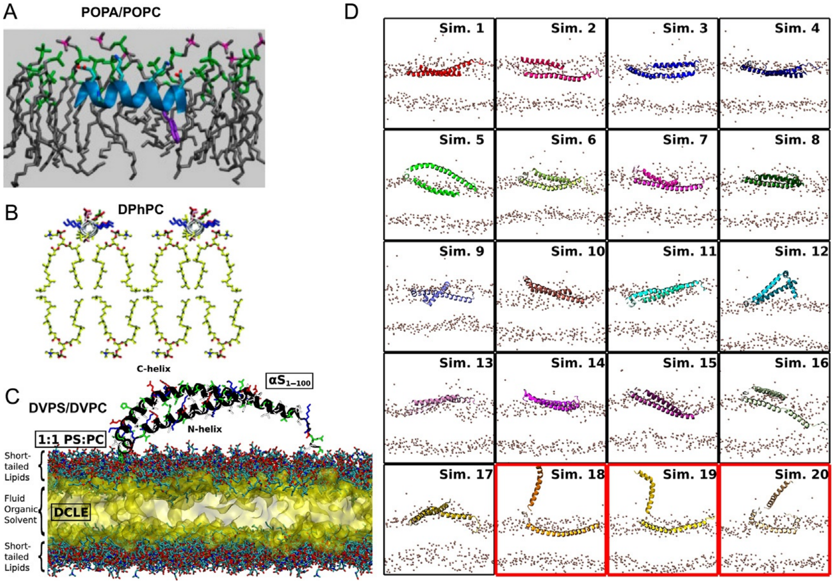

Fig. 14 *Conventional MD and HMMM simulations of* α-Synuclein (aSyn). (A) Peptide to penetrate POPA:POPC membrane and position below the phosphorus atoms of the lipids. The peptide orients such that hydrophilic residues face toward the head group-water region. Lipids tails are rendered as *gray licorice* and protein is displayed as *cartoon*. (B) In DPhPC membrane, peptide is surface bound and makes a shallow defect in the membrane. DPhPC lipids are rendered as *yellow licorice* and protein as *cartoon*. (C) and (D) Using HMMM to study aSyn dynamics on DVPS/DVPC membrane surface. (C) Initial snapshot showing aSyn above the HMMM surface and rendered as *black cartoon*. (D) Final snapshots from 20 simulations showing aSyn to adopt various conformations from extended helical conformation to broken-helix conformation. The structures in *red box* indicate the peptide interacting across the periodic boundary. Lipid phosphorus atoms are shown as *pink spheres* and lipid tails removed for clarity. *Panel A: Reprinted with permission from Pfefferkorn CM, Heinrich F, Sodt AJ, et al. Depth of α-synuclein in a bilayer determined by fluorescence, neutron reflectometry, and computation. Biophys J. 2012;102(3):613–621, https://doi.org/10.1016/j.bpj.2011.12.051, Elsevier. Copyright © 2012 Biophysical Society. Published by Elsevier Inc. All rights reserved (https://creativecommons.org/licenses/by/4.0/); Panel B: Reproduced from reference Garten M, Prévost C, Cadart C, et al. Methyl-branched lipids promote the membrane adsorption of α-synuclein by enhancing shallow lipid-packing defects. Phys Chem Chem Phys. 2015;17:15589–15597, https://doi.org/10.1039/C5CP00244C, with permission from the PCCP Owner Societies 2015. Royal Society of Chemistry (United Kingdom). Permission conveyed through Copyright Clearance Center, Inc.; Panels C and D: Reprinted with permission from Vermaas JV, Tajkhorshid E. Conformational heterogeneity of α-synuclein in membrane. Biochim Biophys Acta Biomembr. 2014;1838(12):3107–3117, https://doi.org/10.1016/j.bbamem.2014.08.012, Elsevier. Copyright © 2014 Elsevier B.V. All rights reserved (https://creativecommons.org/licenses/by/4.0/).*

different lipid bilayers such as DOPS, SAPC, DOPC and DPPC. Studies with DOPS[350] bilayer shows aSyn to localize below the lipid head group region and the protein orients such that the hydrophilic side of the protein faces the lipid head group/water. The peptide had no effect on the DOPS membrane structure. Garten et al.,[351] carried out atomistic simulations to understand how aSyn packs and alters mechanical properties of DOPC, DPhPC and SAPC bilayers. The simulations revealed that aSyn was absorbed into all the bilayers, and shallow packing defects were observed in both SAPC and DPhPC bilayers. In addition, major packing defects were observed in a DPhPC bilayer.

It is also important to understand the effect of lipids on aSyn structure and dynamics, since any change in aSyn conformation will affect protein function. Vermaas et al.[171] performed atomistic simulations to investigate the dynamics of aSyn on DVPS/DVPC membrane. Simulations revealed aSyn to adopt two conformations, one with a broken-helix conformation similar to the NMR structure solved in micelle and second a semiextended helix conformation. A lipid density analysis revealed that a semi-extended helix conformation increases the density of the PS head groups along its edge. Such lipid-mediated transition of protein conformation might be physiologically important for aSyn.

aSyn-membrane interactions are well documented by a study carried out from Viennet et al.[352], who combined several experimental and computational technique to characterize various properties of the membrane and of aSyn (Fig. 15). The atomistic simulations were carried out to investigate how aSyn_{1-61} orients on membranes composed of POPC/POPG (50/50 mol%, fluid phase) and DMPG/DMPC (50/50 mol%, gel phase). The simulations confirm that lysine residues in the N-terminus interact strongly with the POPG head groups rather than with the DMPG head groups. Analysis of lipid order parameter reveal that aSyn has a small effect on the gel phase membrane (DMPC/DMPG), whereas the lipid order parameter is increased in fluid phase membranes (POPC/POPG). The increase in order parameter results in an increased bilayer thickness and a reduced area per lipid.

4.2.2 Peripheral membrane proteins

4.2.2.1 Fibroblast growth factor (FGFs)

FGFs are multifunctional mitogens involved in cell growth, tissue regeneration, wound repair, embryonic development, etc.[353] There are 22 structurally similar FGF members in the human family, and involved in signaling.[353]

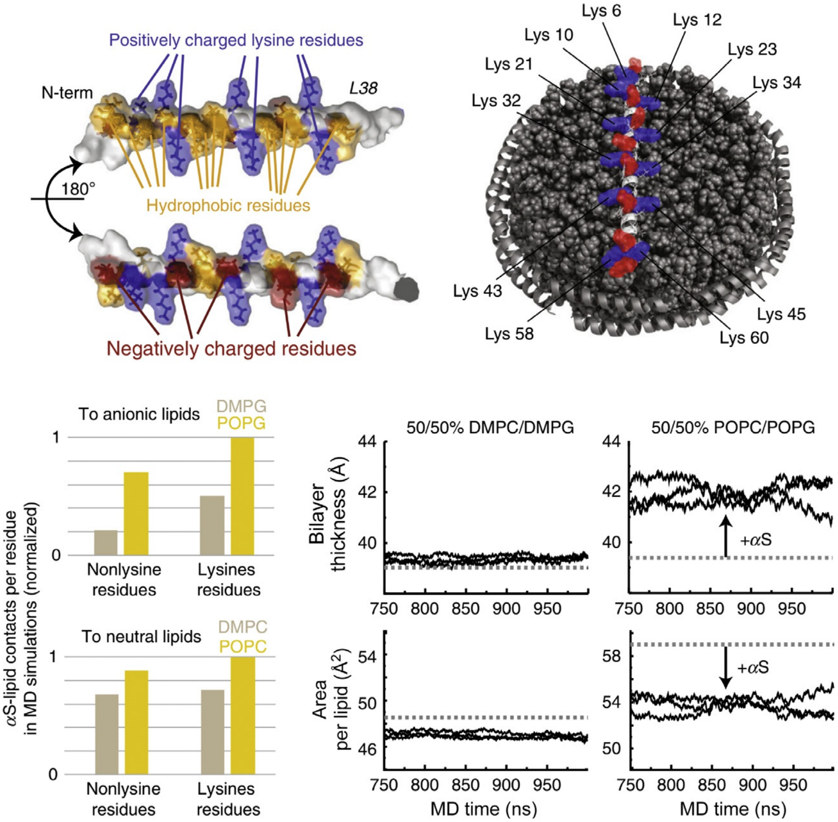

Fig. 15 Peptide–lipid interactions of aSyn in HMMM model. aSyn-DMPC/DMPG and POPC/POPG interactions are depicted. *Top left*: Surface representation of aSyn showing negative, positive, and hydrophobic residues as *licorice*. *Top right*: aSyn on nanodisc surface showing all the lysine residues (*blue*) and negatively charged residues (*red*). *Bottom left*: aSyn–PG/PC contacts within <4 Å are shown. Though both the lipid membranes contain same head group, aSyn makes more contacts with the fluid phase POPC/POPG membrane rather than gel phase DMPC/DMPG membrane. *Bottom right*: In gel phase membrane, aSyn has no or little effect on the membrane properties. But in fluid phase, aSyn increases the bilayer thickness and reduces the area per lipid. *Dashed lines* in the plots indicate membrane only system without aSyn. *Reprinted with permission from Viennet T, Wördehoff MM, Uluca B, et al. Structural insights from lipid-bilayer nanodiscs link α-synuclein membrane-binding modes to amyloid fibril formation. Commun Biol. 2018;1(1):44, Springer Nature. Copyright © 2018 Springer Nature (https://creativecommons.org/licenses/by/4.0/).*

Among them, the basic fibroblast growth factor 2 (FGF2), apart from carrying out its normal functions, also mediates tumor-induced angiogenesis and inhibits tumor cell apoptosis.[354–356] Further, the lack of a signal peptide makes FGF2 unique among its family members, and it is secreted into the extracellular space by an unconventional route, independent of ER/Golgi pathway.[357–359] In vitro studies suggest that the unconventional FGF2 translocation takes place through initial interactions with the inner leaflet PI(4,5)P_2 lipids.[358–361] The FGF2–PI(4,5)P_2 interactions trigger formation of large oligomeric structures on the membrane surface which induce pore formation. The membrane translocated FGF2 monomers are caught by the outer leaflet heparan sulfate proteoglycans.[357,362,363] Moreover, biochemical studies have pointed out that the residues K127, R128, and K133 are important for initial PI(4,5)P_2 binding, residues C77/C95 for oligomerization, and residue K133 for interacting with heparan sulfates.[357,364] Further, there is no structural data describing dimer and trimer interfaces that are a minimal requirement for oligomerization process.

Recently, Steringer et al.[365] tested the key predictions from biochemical studies using AA-MD simulations. To observe the spontaneous interaction of FGF2 monomers with PI(4,5)P_2, the protein was placed 1.5 nm above the mixed membrane composed of POPC/CHOL (70/30 mol%) in the outer leaflet and POPC/CHOL/PIP_2 (65/29.5/5.5 mol%) in the inner leaflet. The simulations revealed FGF2 to spontaneously bind to PI(4,5)P_2 through the known binding pocket residues K127, R128, and K133, thus, confirming with the biochemical studies (Fig. 16A). In addition, simulations showed that FGF2 adopts two different orientations on the membrane surface, called (1) high-affinity orientation evident by strong interaction energies and (2) low-affinity orientation evident by weak interactions. In the high-affinity orientation, FGF2 orients with C95 being accessible to form a disulfide bridge with the second monomer. Whereas in low-affinity, both C95 and C77 are available to form a disulfide bridge with the second monomer, but the interaction with PI(4,5)P_2 is weakened with only R128 making contact with PI(4,5)P_2. The weak interaction with the PI(4,5)P_2 might be a transient state and formation of stable dimers or higher ordered structures with such orientation might not be possible. To test the dependence of PI(4,5)P_2 on FGF2 orientation, the authors also simulated in presence of a single PI(4,5)P_2 in the membrane. The simulations showed a specificity of FGF2 for binding PI(4,5)P_2 with its known binding pocket residues, however, the protein orientation was never stable but instead continuously fluctuating between high- and low-affinity orientations. These results indicate that more than a single PI(4,5)P_2 is required to stabilize the protein on the membrane surface and to promote oligomerization. Having established the binding and orientation for a single FGF2, the next step was to identify the dimeric interface required for oligomer formation. Since trimer

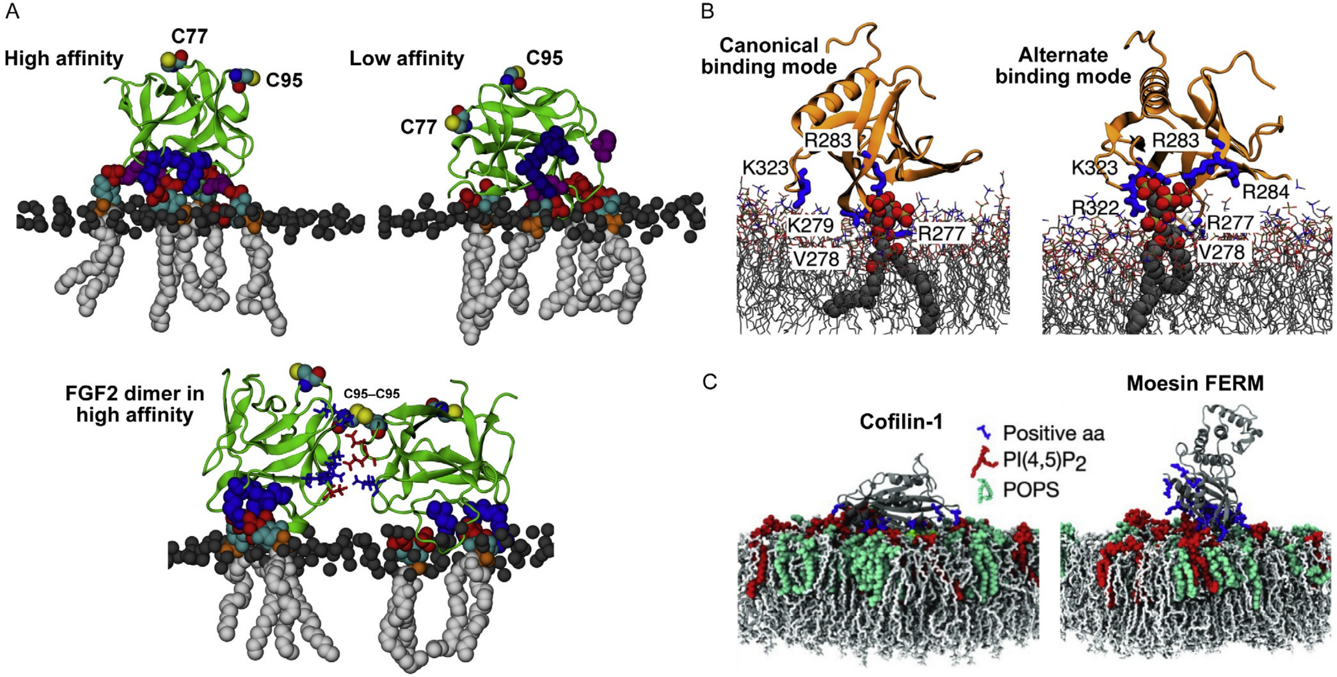

Fig. 16 See legend on opposite page.

structures were the minimal oligomer size observed in experiments, simulations were initiated with three monomers placed 0.5 nm above the membrane surface and arranged such that two monomers faced each other at 0.7 nm and a third monomer faced the other monomers at 1.5 nm distance. During simulations, all three monomers formed stable interactions with PI(4,5)P_2 and adopt the high-affinity orientation. The two nearby monomers dimerized with C95–C95 interactions at the interface, and the structure was further stabilized by four salt bridges formed by two pairs of E86–K118 and E99–K85. The third monomer approached the dimer with the C77–C77 residues at the interface and further stabilized by salt bridges R47–D49, D45–R41, and R80–E53. The dimer interfaces involving residues C95–C95 (interface 1) and C77–C77 (interface 2) observed in MD simulations are consistent with the in vitro studies. Thus, this study

---

Fig. 16 Peripheral membrane proteins in the case studies. (A) FGF2 orientation on the membrane surface. FGF2 binds to PI(4,5)P_2 in high-affinity and low-affinity orientations. High-affinity binding includes all the experimentally known binding pocket residues K127, R128, K133 (rendered as *blue spheres*), whereas in low-affinity, FGF2 loses contact with PI(4,5)P_2. Additional binding residues are rendered as *purple spheres*. High-affinity binding favors FGF2 dimerization via C95–C95 disulfide bridge, which is unavailable with low-affinity orientation. PI(4,5)P_2 tails are rendered as *white spheres*, PI(4,5)P_2 bisphosphates as *red spheres*, inositol ring as *cyan spheres*, phosphate linking PI(4,5) P_2 tails and the inositol ring as *orange spheres*, POPC phosphorous atom as *black sphere*, C95/C77 are shown as *yellow spheres* and protein as *green cartoon*. Rest of the lipids, water, and ions are not shown for clarity. (B) GRP1-PH domain binds to PI(3,4,5)P_3 in both canonical (C site) and alternate (A site) binding modes. In C site mode, PH domain $\beta 1/\beta 2$ loops bind to PI(3,4,5)P_3, whereas in A site mode, binding takes place with $\beta 5/\beta 6$ loops. PI(3,4,5)P_3 is rendered as *spheres*, rest of the lipids as *lines*, protein as *orange cartoon* and key residues are shown as *blue licorice*. (C) Conformation of Cofilin-1 and moesin FERM domain on membrane surface. Positively charged amino acids interacting with the lipids are shown as *blue licorice*, PI(4,5)P_2 and POPS lipids are displayed as *red* and *cyan spheres*, respectively. *Panel A: Reprinted with permission from Steringer JP, Lange S, Čujová S, Sinning I, Tews I, and Nickel W. Key steps in unconventional secretion of fibroblast growth factor 2 reconstituted with purified components. eLife. 2017;6:e28985, https://doi.org/10.7554/eLife.28985, eLife Sciences Publications. Copyright 2017 Steringer et al. (https://creativecommons.org/licenses/by/4.0/); Panel B: Reprinted with permission from Pant S, Tajkhorshid E. Microscopic characterization of GRP1 PH domain interaction with anionic membranes. J Comput Chem. 2019;9999:1–11, https://doi.org/10.1002/jcc.26109, John Wiley and Sons. Copyright © 2019 Wiley Periodicals, Inc. (https://creativecommons.org/licenses/by/4.0/); Panel C: Reprinted with permission from Senju Y, Kalimeri M, Koskela EV, et al. Mechanistic principles underlying regulation of the actin cytoskeleton by phosphoinositides. Proc Natl Acad Sci. 2017;114(43):E8977–E8986, https://doi.org/10.1073/pnas.1705032114, United States National Academy of Sciences.*

establishes a minimal molecular basis required for FGF2 to initially bind PI(4,5)P_2 and to aggregate to large oligomers, which would eventually create membrane pores and escape into extracellular space. The molecular mechanism described here for FGF2 could be related to other PI(4,5)P_2-dependent unconventionally secreting molecules, such as HIV-Tat[366–368] and Interleukin 1β.[369]

4.2.2.2 Pleckstrin homology (PH) domain

Cell signaling is predominantly initiated by the recruitment of peripheral membrane proteins (PMPs) to the cytosolic side of the membrane where they make specific interactions with negatively charged signaling lipids such as PIPs.[370,371] PIPs exist in various isoforms depending on the head group phosphorylation, PI(4,5)P_2, PI(3,5)P_2, PI(3,4)P_2, and PI(3,4,5)P_3.[372,373] The pleckstrin homology (PH) domains are a small important class of PMPs that recognize and bind to only specific PIPs on the cytosolic side of the membrane.[374–376] The PDB currently contains ~177 solved structures of PH domains, some of them solved with a PIP head group (inositol phosphates). All PH domains fold into a β-barrel topology with open ends capped by α-helix on one side and PIP binding motif on the opposite side. The domains comprise about 120 amino acids. The positively charged motif K–X–K/R–X–R in the loop connecting the β1 and β2 strands forms the binding site for the negatively charged PIP head group. However, not all PH domains have the canonical binding motif (K–X–K/R–X–R) for PIPs; for example, the (noncanonical) binding motif of β-spectrin is situated at the opposite face of the β1 and β2 strands,[377] and the ASAP1 PH domain was reported to bind PIP at both canonical and noncanonical binding sites.[378] Here, we present recent results for the general receptor for phosphoinositides isoform 1 (GRP1) PH domain, which has a canonical PIP binding site.

GRP1 is one of the well characterized PI(3,4,5)P_3 recognizing protein belonging to guanine nucleotide exchange factor (GEFs) family.[381] GRP1 is involved in insulin signaling,[382,383] receptor endocytosis[384] and actin dynamics.[385,386] Pant et al.[379] carried out several AA-MD simulations to investigate the spontaneous binding of the GRP1 PH domain to PI(3,4,5) P_3. The simulations were initiated by placing the PH domain 1.5 nm above a mixed membrane composed of PC, PS, and PI(3,4,5)P_3 lipids in varying concentrations. In a neutral pure PC membrane, the PH domain bounced back to the aqueous solution after initial contacts, demonstrating only weak interactions with the PC head groups. However, upon the addition of 20%

negatively charged PS lipid to the membrane, the PH domain was found to strongly interact with the membrane throughout the simulations. The interactions were mainly mediated through the loop connecting $\beta 1$ and $\beta 2$ strands, where the canonical binding motif is located. The side chains of the key residues R277, V278, and K279 stabilizing the interactions were localized to the phosphate head groups, and no deeper insertion was observed. On addition of highly negatively charged PI(3,4,5)P_3 lipids to the membrane, PI(3,4,5)P_3 recognized their canonical binding motif and PH domain orient at an angle of 36.9 ± 9.1 degrees relative to the membrane normal. The key residues at the canonical binding site forming hydrogen bonds with the phosphate head groups are K273, R277, K282, R284, and Y298. Simulations also revealed that PI(3,4,5)P_3 may recognize the loop connecting $\beta 5$ and $\beta 6$ strands, a new binding site previously not reported for the GRP1 PH domain. At this new site, the PH domain orients an angle of 29 ± 11.9 degrees with respect to the membrane normal (Fig. 16B). The key residues at the alternate new site forming hydrogen bonds with the phosphate head groups are R283, R322, and K323. Inspection of the local lipid density revealed that the orientation is influenced by the local concentration of PS lipids, which is higher when PI(3,4,5)P_3 binds to the PH domain at its canonical binding site. Furthermore, in presence of PI(3,4,5)P_3 V278 was observed to penetrate deep into the membrane. Additional free energy calculations suggested that both binding modes are favorable with higher affinity for binding at canonical binding site. The results from this study provide evidence for lipid-dependent binding and activity of PH domains.

4.2.2.3 Actin-binding proteins (ABPs)

Actin, the most abundant and dynamic protein in eukaryotic cells, participates in several cellular functions including the polymerization of filaments, preservation of membrane integrity, contraction of muscle cells, etc.[387] Polymerization of actin filaments leads to cell movement and morphogenesis.[388] The stability, dynamics, length of filaments are controlled by actin-binding proteins (ABPs), which are in turn regulated by PIPs.[389,390] Thus, membrane binding of ABPs, such as cofilin, vinculin, formins, and N-WASP are critical for their activity.[391–395] Among the PIPs, PI(4,5)P_2 interacts with ABPs and serves several functions, including the prevention of actin filament disassembly and capping of filament ends,[396–398] the activation of actin filament assembly. Hence, PI(4,5)P_2 serves as a link between the plasma membrane and actin filaments.[399–401] The presence of PI(4,5)P_2

is central in filament assembly, and any loss in membrane $PI(4,5)P_2$ triggers disassembly of actin filaments.[402–405] Despite the importance of ABPs interaction with $PI(4,5)P_2$, molecular insights into ABPs association and dissociation with lipid membranes has been largely unexplored. To gain molecular insights into dynamics of ABPs on interaction with $PI(4,5)P_2$, we discuss results for cofilin-1 and for the FERM domain of moesin.

Senju et al.[380] performed unbiased AA-MD simulations, initiated by placing the protein 0.5 nm above the membrane surface. During the simulations, both proteins interact with the $PI(4,5)P_2$-enriched membrane via their large positively charged surface (Fig. 16C). Cofilin-1 equilibrates within 50–60 ns with no change in the number of hydrogen bonds formed with the lipids, whereas moesin, due to its large size and slower diffusion, equilibrates within 150 ns. The large and highly negatively charged $PI(4,5)P_2$ head groups readily bind to experimentally identified binding sites on Cofilin-1 and moesin. Cofilin-1 and moesin is stabilized on the membrane surface by several lysine and arginine residues. In addition to $PI(4,5)P_2$ binding to the known binding site for moesin, binding to an additional site was identified, formed by a patch of nine cationic residues: K3, K35, R40, K72, R246, K254, K258, K262, and K26. On average, Cofilin-1 and moesin bind to 3.0 ± 0.1 and 6.0 ± 0.3 $PI(4,5)P_2$ head groups, respectively. The $PI(4,5)P_2$ binding specificity was not hindered by a large concentration of PS lipids in the membrane. None of the residues identified were able to penetrate deep into the membrane but they were instead localized near phosphate atoms. To estimate the binding free energy difference between these two proteins, umbrella sampling simulations were performed. The calculations estimated that cofilin-1 binds with 12 ± 2 kcal/mol and moesin wtih 33 ± 2 kcal/mol, further highlighting the weak interactions of cofilin-1 with the membrane. Thus, the study reveals that despite the interactions to be mainly electrostatic, the dynamics and affinities of ABPs are different which relates to their differential function.

4.2.3 Viral fusion proteins

The genetic material (DNA/RNA) of enveloped viruses is confined within a lipid bilayer, termed virus envelope. The release of the viral genome into host cells requires fusion of the virus envelope with the host cell membrane. However, membrane fusion is opposed by a high kinetic barrier. First, a repulsive dehydration barrier is developed as the distance between the two membranes is within ~30 Å. Second, during the fusion process, membrane strongly deform during fusion, which requires considerable free energy.[406] These kinetic barriers are overcome by the action of membrane fusion glycoproteins that are located at the surface of viruses, where they undergo series of conformational changes during fusion. Membrane fusion begins with the proteins in a high-energy, metastable, compacted state. Upon change in pH or upon sensing receptors on the host membrane, the fusion proteins open up and interact with the host membranes through fusion loops or fusion peptides. The protein releases its stored energy by collapsing, thereby forcing the two membranes into close proximity, hence favoring the formation a hemifused state (Fig. 17A). Finally, a stable low-energy fusion pore is formed, allowing the release of viral genome.

Based on structural differences, fusion proteins can be grouped into three classes, namely, class I, class II, and class III. Class I proteins are characterized by a central trimeric α-helical coiled-coil structure and contain hydrophobic fusion peptides on the N-terminal side (found in retrovirus, filovirus, coronavirus). A typical example is haemagglutinin from influenza A. Class II proteins exhibit β-sheets-rich domains that also contain the fusion loops (found in alphavirus, flavivirus, rubivirus, phlebovirus). Similar to class I proteins, class III proteins contain a central trimeric α-helical coiled-coil structure, while the fusion loops extend β-sheet domains, which is similar to class II (vesicular stomatitis virus, herpes simplex virus, Epstein–Barr virus, baculovirus). Here, we discuss recent work on a class II fusion protein from Rift Valley fever virus (RVFV), which revealed a previously unknown lipid recognition site.

RVFV is transmitted by mosquitos affecting both livestock and humans. The virus enters the host cell through membrane interactions mediated by glycoprotein Gc. However, little was known about the lipid specificity of protein–membrane interactions. Thus, Guardado-Calvo et al. solved a new X-ray structure of glycoprotein Gc that adopts a typical class II conformation.[408] Remarkably, electron density from a lipid mimic was detected in the crystal, at a site that is expected to be in contact with the host membrane during fusion. The structure was next subjected to MD simulations in DOPC/CHOL membranes to investigate specific lipid binding sites at the fusion loops. In agreement with biochemical studies, MD simulations showed that increase of cholesterol concentration resulted in deep insertion of the fusion loops and, hence, stronger binding to the membrane. The cholesterol-dependent stability was attributed to the ability of cholesterol to occupy space between the DOPC lipids, thereby preventing close

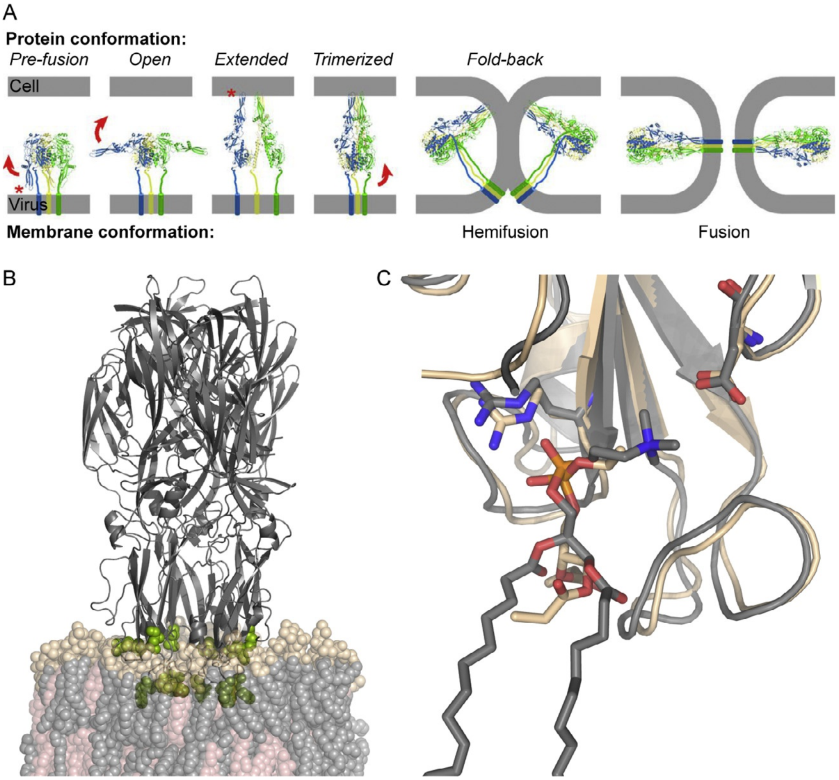

Fig. 17 Viral fusion proteins. (A) Sequential change in protein conformation during membrane fusion.[407] (B) Simulation system of the class II fusion protein Gc of Rift Valley fever virus in contact with a DOPC/CHOL membrane. (C) Closeup view of a DOPC lipid bound to the PC lipid recognition site of Gc. *Gray*: MD simulation. *Brown*: crystal structure with a short-tailed lipid mimic.[408] *Panel A: Reprinted with permission from Kim IS, Jenni S, Stanifer ML, et al. Mechanism of membrane fusion induced by vesicular stomatitis virus G protein. Proc Natl Acad Sci. 2017;114(1):E28–E36, https://doi.org/10.1073/pnas.1618883114, United States National Academy of Sciences.*

packing of DOPC head groups. The loosely packed DOPC head groups allowed the fusion loops to penetrate the membrane, thus forming stable interactions. Further, during the simulations DOPC was seen to bind to the same contact site as also observed in the crystal (Fig. 17B and C). Comparison of the RVFV structure with other class II family members (flavivirus E and alphavirus E1) revealed that the DOPC binding site is largely conserved, suggesting that the site may be widely used by viruses with class II proteins to sense the lipid composition of their host cells.

4.3 Coarse-grained simulations of membrane proteins

4.3.1 Curvature induction and membrane remodeling by FAM134B reticulon homology domain assist selective ER-phagy

The endoplasmic reticulum (ER) is an important cellular structure found in eukaryotic cells and composed of phospholipid bilayer delimited tubules and sheets. The ER is associated with different cellular functions depending on tissue location in the body.[409] It is major site of proteins synthesis and transport, protein folding, lipid and steroid synthesis, carbohydrate metabolism, and storage. Newly synthesized polypeptides are folded inside the ER lumen by chaperones, where also postsynthesis glycosylation takes place. Loss of ER function can result in the accumulation of wrongly folded proteins and other stress factors, resulting a major cellular response to deal with this is through an autophagy receptor-mediated degradative ER-autophagy process (ER-phagy).[410] The specific mechanism involved in ER-autophagy has been the subject of different research investigations and it is believed to involve membrane-modulated protein interactions, including the reticulon-homology-domain (RHD) of the ER. The RHD contains the FAM134 protein family (FAM134A, FAM134B, FAM134C) and two autophagy-related proteins, the microtubule associated light chain 3 (LC3) and GATE16/GABARAP.[411]

FAM134B interacts with LC3 using an LC3-interacting region (the LIR motif, sequence DDFELL) that is highly conserved across the FAM134 protein family. For instance, downregulation of the FAM134B[412] or substitution of the LIR motif with alanine residues prevented interaction with LC3 and ER autophagosomes. A number of diseases have been attributed to the loss of FAM134B function, including neuropathy which is associated with the truncation of the protein sequence. The function of the FAM134 family in the ER-phagy is believed to have a relationship with the membrane-shaping RHD structural motif that is conserved throughout the family and shared with other membrane shaping proteins.[413–416] The underlying mechanism, however, remains unsolved as a result of lack of atomic-level insight into its structural and dynamical processes.

FAM134 presents an exciting possibility to interrogate the initial sequence of events, deriving from protein–lipid interactions, that affect membrane structural integrity and drive ER-phagy. To understand these separate processes, Bhaskara et al. employed a multiscale simulation approach that generated structural models for CG-MD simulations from multiple μs-long explicit solvent AA-MD sampling.[417] The model protein consists of two TM helical hairpins that are connected to another two helical segments composed of amphipathic amino acids. The FAM134B-RHD model structures generated from the AA-MD were embedded in MARTINI lipids using both POPC and mixed lipid bilayers (to model the ER membrane) as well as bicelle model systems. Intracellular aqueous and ionic conditions of the physiological membrane were mimicked with MARTINI water, Na^+ and Cl^- models. In total, 95 × 1 μs independent FAM134B-RHD-lipid simulations were performed. As reference simulations, 97 × 1 μs with empty bicelles (no protein present) and 96 × 1 μs membrane systems with inserted $KALP_{15}$ protein were also performed. KALP proteins contain an alternating A/L sequence, flanked by lysine residues and serve as TM model. They exhibit a TM helical structure with different length, depending on the number of repeating A/L residues. The large-scale CG simulations with the MARTINI FF allowed the detection of very interesting structural phenomena which identified the detailed mechanism by which FAM134B (and by extrapolation other RHD proteins) induces membrane curvature in ER-phagy. First, the overall mechanism was found to proceed via an initial FAM134B RHD domain interaction with the membrane, followed by embedding events facilitated by the amphipathic nature of the RHD. The membrane insertion of the RHD motif perturbed the local symmetry of the membrane and created uneven and extensive asymmetric patches around the amphipathic protein segment. This was observed to directly stretch the lipid layer accompanied by increased area per lipid (curvature induction). This structural remodeling was observed in 97% of all independent FAM134B-RHD membrane simulations. And the membrane curvature was eventually observed to result in complete shape transition from an initial bicellar structure to vesicle formation (Fig. 18). In contrast, $KALP_{15}$ only marginally perturbed the membrane as seen in slight reduction in bilayer thickness in 5 out of total 96 independent CG-MD simulations. The dramatic and complete vesiculation observed in the CG simulations involving FAM134B-RHD shed some light on the role of FAM134B-RHD in provoking structural changes in ER membranes. The vesicles formation facilitates autophagosome clearance and firmly establishes the involvement of specific protein–membrane interactions in ER-phagy. The fact that membrane curvature was not observed with $KALP_{15}$ further highlights the high specificity of the process for the amphipathic motif of RHD proteins, which in the FAM134 protein family is structurally coupled to LIR motifs that serve as recognition site for autophagosomes.

In summary, the FAM134 family expressed in ER membranes actively induces formation of smaller vesicles from the ER membrane through their

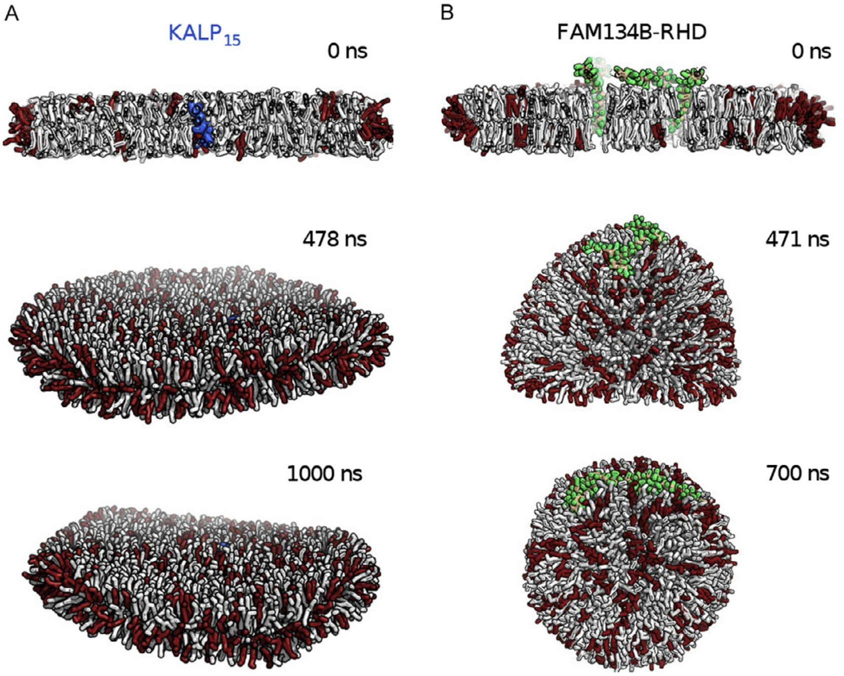

Fig. 18 Membrane remodeling induced by the FAM134B-RHD protein. Snapshots taken from different time points of CG-MD simulations of membrane systems with (A) KALP_{15}, which was unable to induce membrane vesiculation within 1 μs, and (B) FAM134B-RHD, which induced vesicle formation within 700 ns. *Panels A and B: Reprinted with the permission from Bhaskara RM, Grumati P, Garcia-Pardo J, et al. Curvature induction and membrane remodeling by FAM134B reticulon homology domain assist selective ER-phagy. Nat Commun. 2019;10(1):2370. Copyright 2019* Springer Nature Limited.

RHD motifs; the protein then employs its LIR motif for interacting with autophagosomes to facilitate ER clearance. This study demonstrates how MD simulations can serve as *molecular microscope* and help to elucidate mechanism of protein–membrane system, in this case the bilayer-to-vesicle transition via induced membrane curvature by the highly conserved amphipathic RHD.

4.3.2 Lipid droplet biogenesis is a liquid phase separation spatially regulated by seipin and membrane curvature

Lipid droplets (LD) are organelles and highly dynamic structurally and in terms of their composition. They are vesicular assemblies generated in the ER and contain neutral lipids, such as triglycerides (TGs) and sterol esters at their core. The neutral lipids are surrounded by a single phospholipid layer with protein molecules (integral and peripheral) decorating the phospholipid monolayer.[418] LDs are associated with functional roles, which include their role as energy storage compartments for excess neutral lipids from where they can be later mobilized for energy generation via enzymatic lipolysis. Moreover, LDs also provide a buffer area where otherwise toxic endogenous fatty acids are stored and prevented from triggering cell death. The biogenesis of LDs has recently been understood to proceed within the two ER membrane leaflets with an initial lens formation resulting from lipid demixing. For this, integral ER membrane proteins are believed to play a critical role. In addition, a critical concentration of neutral lipids within the ER membrane bilayer is crucial for lipid lens formation to get started, while differences in surface tension between the ER lumenal (the ER interior) and cytoplasmic (the ER exterior) lipid layers as well as the ER membrane protein seipin are important to ensure that nascent LDs bud off the ER membrane from the cytoplasmic lipid monolayer. However, the detailed mechanism of LD formation, including the specific contribution of membrane and protein interactions, remains poorly understood.

In the case study presented here, Zoni et al. employed two CG models and several μs-long MD simulations to provide insight into LD biogenesis.[419] In their simulation setups featuring only lipids, i.e., in the absence of proteins they employed the SDK model.[92],[420–422] The SDK model is a CG-FF originally developed by Shinoda, DeVane, and Klein (SDK), which has been demonstrated to correctly model the interfacial interaction of lipids and water.[92,93,423] This model was also shown to reliably reproduce the energy barrier for diacylglycerol-water flip-flop and interfacial tensions. For the system setups with the membrane protein seipin, the MARTINI parameter sets were used. Seipin is mostly expressed in the ER and in its functional form, it is assembled into a homo-oligomeric barrel-shaped integral membrane protein with a central pore. It is mostly found concentrated at membrane junctions and in contact with LDs.

Multiple system setups were designed to investigate different structural involvements in LD biogenesis. First, the process of lens formation was examined by inserting variable amounts of triglyceride molecules (between 2% and 10%) randomly between the two leaflets of a bilayer membrane and simulated the systems for 3 × 1.5 μs or until spontaneous triglyceride lens formation occurred. The effect of different lipid types on lens formation dynamics was additionally examined using various binary combinations of DOPC (18:1) with either of DOPE (18:1), POPC (16:0,18:1), POPE (16:0,18:1), DPPC (16:0), CHOL, or diacylglycerol added to it, while an

ER-like membrane system was modeled using a constant composition of DOPC, DOPE, CHOL, and diacylglycerol. The simulation investigating the role of seipin-membrane interaction was initiated from a model, in which seipin was fitted into the available cryo-EM model of human seipin arranged into a ring shape[424] (PDB code: 6DS5). This was inserted into a DOPC membrane containing 2% triglyceride molecules. Three replicas of this setup were simulated for 4 μs. In total, about 75 different simulation systems were investigated with most of them simulated in three replicas, and each replica lasting for 0.5–9.5 μs depending on the particular setup.

In the first CG case study, the role of the RHD motif-containing FAM1343B protein in ER-phagy was examined. It was shown that RHD interaction with the ER bilayer induces membrane curvature and complete membrane remodeling into vesicles for presentation for degradation by autophagosomes. In the present case study, the ER integral protein seipin was also shown to induce membrane curvature in cytoplasmic ER membrane layer as part of the structural events in LD formation. Furthermore, interaction of triglycerides with seipin resulted in the reduction of the diffusion of the neutral lipids within the membrane bilayer, which was found to encourage the accumulation of triglycerides in the vicinity of the membrane protein. The concentration of triglycerides was observed to double around seipin. Interestingly, experimental studies reported seipin to preferentially localize at ER membrane sites that have been reported to be associated with LD formation. In the absence of seipin, LD biogenesis was significantly impaired.[425,426] LD lens formation occurred in the absence of seipin, but at a much reduced rate. Moreover, lens formation was seen to strongly depend on the concentration of free triglycerides, showing the involvement of a liquid–liquid phase separation process that is principally driven by the equilibrium concentration of triglycerides. By increasing the surface tension of the membrane lipids, an effect that was accomplished via a gradual scaling of the box size in *xy*-dimension, lens formation was inhibited. In effect, a lower membrane tension was found to favor lens formation, and thus LD generation. This agrees well with the observation that LDs are formed by the cytoplasmic monolayer of the ER membrane, characterized by a surface tension much lower than that of the lumenal ER membrane monolayer. Other factors found to promote liquid–liquid phase separation include the presence of precursor molecules for neutral lipids in the membrane, especially diacylglycerol, cholesterol, as well as unsaturated lipids. ER-like membrane systems were observed to form TG lenses at solute concentrations much lower than membrane systems without cholesterol and diacylglycerol. This was believed to be an adaptive protection mechanism that allows the ER to spontaneous mop up neutral lipids to prevent toxic aggregation.

Taken together, the use of CG-MD simulations allowed the sampling of critical structural events in LD biogenesis, showing that liquid–liquid phase separation initiated by demixing of neutral lipids within the ER bilayer is accentuated by interaction with the ER membrane protein seipin and the presence of neutral lipid precursor molecules, like cholesterol and diacylglycerol in the membrane. Differential ER-membrane surface tension caused by a higher osmotic pressure within the ER lumen ensures that following the formation of critical intra-ER membrane neutral lipid lenses, LDs are budded off the cytoplasmic monolayer, where a lower surface tension operates. For more detailed information about LD biogenesis, we recommend reading the review article.[427]

4.3.3 Lipid–protein interactions are unique fingerprints for membrane proteins

The emergence of CG-MD simulation in recent years has not just made access to longer timescales feasible, simulating more complex biophysical phenomena has increasingly become possible. In the first CG case study, protein–membrane interaction was investigated using a multiscale simulation approach that clearly demonstrated the influential roles played by a TM protein in membrane vesiculation. The use of a CG-FF made it possible to follow the entire structural process, starting with the interaction of lipid molecules with FAM134B-RHD, to curvature induction in the membrane architecture, and ultimately to vesicle formation. The fact that membrane remodeling was not observed with another TM protein, $KALP_{15}$, indicates that there exists a degree of specificity in the protein–membrane interaction. In other words, rather than merely providing a structurally dynamic matrix for membrane proteins, lipid membranes are capable of establishing specific binding interactions with proteins, both integral and peripheral. This realization suggests that biological membranes are active participants in biochemical processes rather than functioning as a passive bystander in cellular processes. With an average cell membrane containing many different membrane proteins of diverse structural families (constituting up to 30% of the membrane area), a highly complex interaction pattern is expected between the proteins and the membrane lipids.[27,428,429]

One class of membrane proteins are the peripheral proteins that interact with the polar head groups of the membrane lipid or with integral membrane proteins.[430] Peripheral proteins have no contact with the hydrophobic core of the membrane and are located both on the cytosolic surface of the cell membrane, where they are often involved in structural functions (e.g., actin) or in signal transduction (e.g., protein kinase C), and on the extracellular surface of the membrane (e.g., extracellular matrix proteins such as collagen). The integral membrane proteins directly interact with the hydrophobic membrane either via a TM protein domain traversing the membrane, or by covalent tethering through a membrane fatty acid. Interaction with the different protein classes allows the cell membrane to perform its varied biological functions and knowledge of the specific details of these interactions is crucial to understanding the basis of life at the subcellular level.

In the case study reviewed here, Corradi et al. developed a CG-based MD simulation strategy to probe how 10 structurally diverse plasma membrane proteins interact with a membrane[431]; these include glucose transporter 1 (GLUT1), aquaporin-1 (AQP1), AMPA-sensitive glutamate receptor 2 (GluA2), the dopamine transporter (DAT), the epidermal growth factor receptor (EGFR), the voltage-dependent Shaker potassium channel 1.2 (Kv1.2), the sodium/potassium pump (Na^+K^+-ATPase), the P-glycoprotein (Pgp), the delta opioid receptor (δ-OPR), and the prostaglandin H2 synthase (COX1). In this work, lipids of 63 different types were distributed asymmetrically between the two membrane leaflets to provide a realistical model of a plasma membrane.[33,224] In the extracellular membrane leaflet, the incorporated lipids feature a higher degree of lipid chain saturation and include gangliosides and PC, but also to some extent cholesterol, SM, ceramide, and diacylglycerol. The cytosolic membrane leaflet, on the other hand, included most of the charged lipids PA, PE, PS, PI, PIP, PIP_2, and PIP_3 and a higher content of unsaturated fatty acid chains. The inner leaflet further contained lysophosphatidylcholine (LPC) lipids. Using the MARTINI FFs, patches of the membrane model were set up, one patch for each of the 10 proteins. Each patch measured 42 nm in both *x*- and *y*-dimensions and contained about 6000 mixed lipids as described above. Four copies of each membrane protein were inserted in the membrane patch with each protein copy separated by a distance of about ~20 nm from the directly neighbored ones, all four of which were arranged in a square formation (Fig. 19). Simulating four copies of the same protein per membrane patch allows for improved statistics. Ten such assemblies were established for the ten protein–membrane assemblies, each of them was simulated for 30 μs. With the aid of weak position restraints, the protein

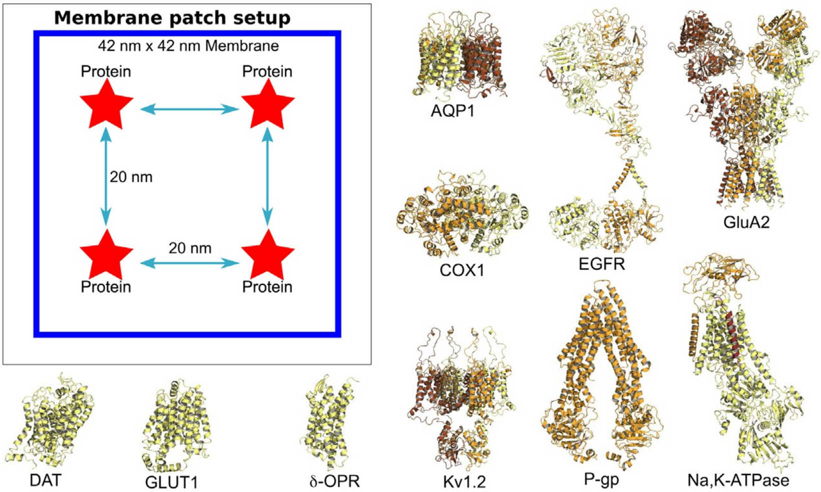

Fig. 19 Protein–membrane simulation setup for probing the lipid–protein interaction *fingerprints*. In the *inset panel*, the *red stars* mark the positions of the protein molecules held in place with a weak position restraining force of 1 kJ mol^{-1} nm^{-2}. Each protein molecule is separated from the other ones by a distance of at least 20 nm. The four protein molecules are embedded in the membrane system (*white background*), which was modeled as a mixture of 63 different lipid types. The assembly is replicated for each of the 10 protein molecules studied, which are shown one the right and below. These proteins are structurally diverse, ranging from single domain globular proteins like DAT, GLUT1, δ-OPR, AQP1, COX1, to more complex multidomain TM protein assemblies like Kv1.2, EGFR, P-gp, GluA2, and Na^{+}K^{+}-ATPase. *Reprinted with permission from Corradi V, Mendez-Villuendas E, Ingólfsson HI, et al. Lipid-protein interactions are unique fingerprints for membrane proteins. ACS Cent Sci. 2018;4(6):709–717, https://doi.org/10.1021/acscentsci.8b00143, American Chemical Society. Copyright 2015 American Chemical Society. Further permissions related to the material excerpted should be directed to the ACS.*

molecules were kept in place, preventing them from aggregating. In reality, protein aggregation within the membrane matrix remains a possibility. The use of protein position restraints allows for the lateral diffusion of lipid molecules to be studied; by decoupling this from protein aggregation, it becomes easy to observe how each lipid molecule interacts with the protein molecules.

Each system was then analyzed for any discernible pattern in protein–membrane interactions that is essentially unique to each protein (called *fingerprint*). For each protein, selective interactions with distinct lipid types were observed, resulting in a lipid enrichment pattern in the immediate vicinity of the protein molecules. With different protein macromolecules being present in the cell membrane, it immediately becomes apparent how such nonuniform interaction with the lipids might contribute toward influencing the global properties of the membrane. For this reason, it is also expected that membrane properties will vary with protein composition of the cell membranes, from a particular cell type to another, as well as between individual organisms based on the internal constitution. In other words, the *matrix experience* presented by the membrane continuum is not as uniform as it might first appear but in actual fact is dictated by specific structural phenomena, resulting from each protein and other membrane constituents. A radius of 0.7 nm was used in describing interaction shells around each protein molecule and the reported behavior represents average over four copies of each protein (Fig. 19).

From the complex array of interactions between membrane protein and lipids, the most glaring observations include a generalized depletion of SM, PCs, LPC (except for COX1), and ceramides (with the exception of COX1 and EGFR) in the immediate vicinity of all 10 protein molecules. On the other hand, diacylglycerol, PIP_2, PIP_3, gangliosides, and polyunsaturated lipids were specifically attracted to the local interaction shell around all 10 proteins. The lipid enrichment-depletion behavior was, however, not always symmetrical between the two membrane leaflets. This was most striking with respect to the gangliosides, PIP_2 and PIP_3, which are important lipids involved in cell signaling function. For instance, gangliosides play an active role in protein sorting, while PIP_2 and PIP_3 are crucial in modulating protein–protein interactions within the membrane matrix (e.g., in Kir2.1 channels, see Section 4.1.2). The enrichment of gangliosides around the proteins was most striking in the outer membrane leaflet, while the PIP_2 and PIP_3 lipids were selectively enriched in the membrane inner leaflet.

These results represent a necessary simplification of an extremely complex interaction behavior, especially considering that each protein represents a structural architecture that deviates from a uniform cylindrical geometry. Considering the no irregular shapes of the biological proteins and the varied composition of amino acids, each set of protein–membrane interaction constituted an interaction fingerprint, which strongly influences the lateral organization of lipids in the cell membrane. Since the model employed in this case study investigated each protein molecule in isolation, a more complex membrane with attendant further complication of membrane properties is likely to occur in biological membranes, where different protein molecules simultaneously colocalize in close proximity.

5. Conclusions and future directions

In this chapter, we provide molecular level insights into protein–membrane interactions in various cellular processes. For each case study, we have given a general overview of the system, followed by the most relevant findings from MD simulations. In Section 1, we provide a short introduction to prokaryotic and eukaryotic cells and then discussed in detail the structures of various lipid species which are basic elements of cell membranes. Next, we have introduced membrane proteins, which along with lipids are essential to carry out different cellular functions. We concluded the section discussing various experimental techniques used in the studies of protein–membrane interactions and the role of computational methods, such as MD simulations in further advancing our knowledge in the field. In Section 2, we have reviewed various FFs used to describe the lipids in MD simulations. The section includes a discussion on the availability of lipid species for each FF and explains the membrane properties commonly used to validate the lipid FFs against experimental data. For a more detailed background on FFs, readers are requested to refer to chapters "Pairwise-additive and polarizable atomistic force fields for molecular dynamics simulations of proteins" by Lemkul and "Scale-consistent approach to the derivation of coarse-grained force fields for simulating structure, dynamics, and thermodynamics of biopolymers" by Liwo of this book. In Section 3, we have provided some practical information on how to build protein–membrane systems, a list of MD simulation packages and tools available to analyze the output the data from MD simulations. The section begins with a detailed review on CHARMM-GUI functionalities to build various protein–membrane systems for use with the CHARMM FF, followed by methods to set up systems for use with AMBER, OPLS-AA, GROMOS, and MARTINI FFs. In addition, we have also covered the tools available to build glycoproteins and glycolipids for MD simulations. We have concluded this section listing the tools available to analyze the trajectory files created by protein–membrane MD simulations. Finally, in Section 4, we have reviewed MD studies of protein–membrane systems. The section is split into three subsections: first, we have presented case studies of integral membrane proteins elucidated by atomistic simulations; second, we have reported atomistic simulations of peripheral membrane proteins: third, we selected a few case studies that employed CG MD simulations to study biological process of large protein–membrane systems, which are computationally too demanding for an atomistic approach. The reviewed topics include protein-induced bicelle-to-vesicle transformation, spontaneous triglyceride lens formation in lipid droplet biogenesis, and identifying unique lipid fingerprints for membrane proteins of various topology.

The diverse cases reviewed in Section 4 provided key molecular insights into how specific lipids regulate protein activity, impressively demonstrating that MD simulations are a vital technique for studying protein–membrane systems. As seen in the presented cases, the recent advancements in the supercomputing facilities along with methodological developments regarding the MD codes has already enabled MD simulations at the microsecond timescale. With regular improvements of FFs to increase their accuracy along with developments of advanced algorithms to speed up MD simulations, the efficacy of the MD studies will further increase in the future. In addition, sustained improvement in experimental techniques, particularly in lipidomic studies, has benefited MD studies immensely in narrowing down from a large pool of lipid species to few specific lipids of interest.

In spite of MD simulations being able to complement experimental results, there are few limitations to be addressed. There are several FFs available for both proteins and lipids, but all have their own shortcomings in reproducing experimental data. Moreover, the simulation of protein–membrane systems requires protein and lipid FFs that are compatible with each other and reproduce the properties of both the protein and the lipid bilayer. The FF benchmarks to date are mostly limited to either proteins or to lipids, while their compatibility and ability to provide a balanced description of protein–lipid interactions has not yet been systematically checked. In terms of application challenges, it should be considered that biological membranes are complex with asymmetric distributions of different lipid species between the two leaflets. Thus, even in the absence of proteins, membranes can undergo curvature and separate into specialized lipid domains. However, most MD simulations are carried out with planar lipid membranes composed of a few selected lipids, rendering them incapable to mimicking the lipid complexity of biological membranes or the observed membrane curvature. Moreover, the traditional way of setting up infinite membrane simulations with periodic boundary conditions further hinders any stabilization of membrane curvature. While mimicking biological membrane composition would be a challenge, spontaneous membrane curvature or protein-induced curvature can be studied using discontinuous finite membranes, such as bicelles, an ideal system to study membrane curvature. Proteins undergo several posttranslational modifications before being transferred into the plasma membrane, and one of the modifications is the covalent attachment of sugar residues or glycans to the proteins. More than 50% of all the eukaryotic proteins are glycosylated, however, only few MD studies have considered protein glycosylation. With the availability of tools to identify glycan sites and build glycoproteins, future MD studies should increase the system complexity by considering glycosylation when required. Such studies would lead to several discussions in the glycobiology field in terms of structure, function and composition of glycans. Experimentally observed conformational changes in protein structure on ligand binding or observing spontaneous lipid-mediated protein structural change is still a challenge with conventional MD simulations. There are several enhanced sampling methods to overcome the limitations, but the systems have to be treated with several biases which would further influence the end results.

In spite of these limitations, MD simulations of protein-membrane systems have rapidly progressed over the last few years and complemented experimental studies in providing molecular and dynamic details at atomistic resolution for protein–lipid interactions.

Acknowledgments

B.S. and J.L. received funding for this project from the Deutsche Forschungsgemeinschaft (DFG, German Research Foundation, http://www.dfg.de/) through grant number 267205415 (CRC 1208, project A07). B.S. and O.O.O. acknowledge support through the Initiative and Networking Fund of the Helmholtz Association, grant number ERC-RA-0034. J.S.H. and C.P. acknowledge support through the Deutsche Forschungsgemeinschaft (SFB 1027/B7). We thank Kalina Atkovska for preparing parts of Fig. 17.

References

1. Bakheet TM, Doig AJ. Properties and identification of human protein drug targets. *Bioinformatics*. 2009;25(4):451–457. https://doi.org/10.1093/bioinformatics/btp002.
2. Yildirim MA, Goh KI, Cusick ME, Barabsi AL, Vidal M. Drug-target network. *Nat Biotechnol*. 2007;25:1119–1126. https://doi.org/10.1038/nbt1338. (a) Berg C, Engels I, Rothbart A, et al. Human mature red blood cells express caspase-3 and caspase-8, but are devoid of mitochondrial regulators of apoptosis. *Cell Death Differ*. 2001;8:1197–1206. https://doi.org/10.1038/sj.cdd.4400905. (b) Ji P, Murata-Hori M, Lodish HF. Formation of mammalian erythrocytes: chromatin condensation and enucleation. *Trends Cell Biol*. 2011;21(7):409–415. issn: 0962–8924. https://doi.org/10.1016/j.tcb.2011.04.003.
3. Lyman E, Hsieh CL, Eggeling C. From dynamics to membrane organization: experimental breakthroughs occasion a "modeling manifesto". *Biophys J*. 2018;115(4): 595–604. https://doi.org/10.1016/j.bpj.2018.07.012.
4. Singer SJ, Nicolson GL. The fluid mosaic model of the structure of cell membranes. *Science*. 1972;175(4023):720–731. https://doi.org/10.1126/science.175.4023.720.
5. Engelman D. Membranes are more mosaic than fluid. *Nature*. 2014;438:578–580. https://doi.org/10.1016/j.bbamem.2014.01.006.

6. Nicolson GL. The fluid-mosaic model of membrane structure: still relevant to understanding the structure, function and dynamics of biological membranes after more than 40 years. *Biochim Biophys Acta Biomembr*. 2014;1838(6):1451–1466. https://doi.org/10.1016/j.bbamem.2013.10.019.
7. Goñi FM. The basic structure and dynamics of cell membranes: an update of the Singer-Nicolson model. *Biochim Biophys Acta Biomembr*. 2014;1838(6):1467–1476. https://doi.org/10.1016/j.bbamem.2014.01.006.
8. Tanford C. The hydrophobic effect and the organization of living matter. *Science*. 1978;200(4345):1012–1018. https://doi.org/10.1126/science.653353.
9. Yeagle PL. Chapter 2—The lipids of biological membranes. In: Yeagle PL, ed. *The Membranes of Cells*. 3rd ed. Boston: Academic Press; 2016:27–56. https://doi.org/10.1016/B978-0-12-800047-2.00002-4.
10. Marventano S, Kolacz P, Castellano S, et al. A review of recent evidence in human studies of n-3 and n-6 PUFA intake on cardiovascular disease, cancer, and depressive disorders: does the ratio really matter? *Int J Food Sci Nutr*. 2015;66(6):611–622. https://doi.org/10.3109/09637486.2015.1077790.
11. Spector AA. Essentiality of fatty acids. *Lipids*. 1999;34(Pt. 1):S1–S3. https://doi.org/10.1007/BF02562220.
12. Harayama T, Riezman H. Understanding the diversity of membrane lipid composition. *Nat Rev Mol Cell Biol*. 2018;19(5):281–296. https://doi.org/10.1038/nrm.2017.138.
13. Yamashita A, Hayashi H, Nemoto-Sasaki Y, et al. Acyltransferases and transacylases that determine the fatty acid composition of glycerolipids and the metabolism of bioactive lipid mediators in mammalian cells and model organisms. *Prog Lipid Res*. 2014;53:18–81. https://doi.org/10.1016/j.plipres.2013.10.001.
14. Krauß M, Haucke V. Phosphoinositides: Regulators of membrane traffic and protein function. *FEBS Lett*. 2007;581(11):2105–2111. https://doi.org/10.1016/j.febslet.2007.01.089.
15. Viaud J, Mansour R, Antkowiak A, et al. Phosphoinositides: important lipids in the coordination of cell dynamics. *Biochimie*. 2016;125:250–258. https://doi.org/10.1016/j.biochi.2015.09.005.
16. Dowhan W, Bogdanov M, Mileykovskaya E. Chapter 1—Functional roles of lipids in membranes. In: Ridgway ND, McLeod RS, eds. *Biochemistry of Lipids, Lipoproteins and Membranes*. 6th ed. Boston: Elsevier; 2016:1–40. https://doi.org/10.1016/B978-0-444-63438-2.00001-8.
17. Vance JE. Phospholipid synthesis and transport in mammalian cells. *Traffic*. 2015;16(1):1–18. https://doi.org/10.1111/tra.12230.
18. Chitraju C, Trötzmüller M, Hartler J, et al. Lipidomic analysis of lipid droplets from murine hepatocytes reveals distinct signatures for nutritional stress. *J Lipid Res*. 2012;53(10):2141–2152. https://doi.org/10.1194/jlr.M028902.
19. Raetz CR, Dowhan W. Biosynthesis and function of phospholipids in Escherichia coli. *J Biol Chem*. 1990;265(3):1235–1238.
20. Ramstedt B, Slotte JP. Membrane properties of sphingomyelins. *FEBS Lett*. 2002;531(1):33–37. https://doi.org/10.1016/S0014-5793(02)03406-3.
21. Sezgin E, Levental I, Mayor S, Eggeling C. The mystery of membrane organization: composition, regulation and roles of lipid rafts. *Nat Rev Mol Cell Biol*. 2017; 18:361–374. https://doi.org/10.1038/nrm.2017.16.
22. Tan RX, Chen JH. The cerebrosides. *Nat Prod Rep*. 2003;20:509–534. https://doi.org/10.1039/B307243F.
23. López CA, Rzepiela AJ, de Vries AH, et al. Martini coarse-grained force field: extension to carbohydrates. *J Chem Theory Comput*. 2009;5(12):3195–3210. https://doi.org/10.1021/ct900313w.

24. Yanagisawa K. Role of gangliosides in Alzheimer's disease. *Biochim Biophys Acta Biomembr*. 2007;1768(8):1943–1951. https://doi.org/10.1016/j.bbamem.2007.01.018.
25. Matsuzaki K, Kato K, Yanagisawa K. Aβ polymerization through interaction with membrane gangliosides. *Biochim Biophys Acta*. 2010;1801(8):868–877. https://doi.org/10.1016/j.bbalip.2010.01.008.
26. Benvegnu T, Lemiègre L, Cammas-Marion S. Archaeal lipids: innovative materials for biotechnological applications. *Eur J Org Chem*. 2008;2008(28):4725–4744. https://doi.org/10.1002/ejoc.200800452.
27. van Meer G, Voelker DR, Feigenson GW. Membrane lipids: where they are and how they behave. *Nat Rev Mol Cell Biol*. 2008;9(2):112–124. https://doi.org/10.1038/nrm2330.
28. van Meer G, de Kroon AIPM. Lipid map of the mammalian cell. *J Cell Sci*. 2011;124(1):5–8. https://doi.org/10.1242/jcs.071233.
29. Simons K, Ikonen E. Functional rafts in cell membranes. *Nature*. 1977;387(43): 569–572. https://doi.org/10.1038/42408.
30. Baumgart T, Hammond AT, Sengupta P, et al. Large-scale fluid/fluid phase separation of proteins and lipids in giant plasma membrane vesicles. *Proc Natl Acad Sci*. 2007;104(9):3165–3170. https://doi.org/10.1073/pnas.0611357104.
31. Levental KR, Levental I. Chapter Two–Giant plasma membrane vesicles: models for understanding membrane organization. In: Kenworthy AK, ed. *Lipid Domains. Current Topics in Membranes*. vol. 75. Academic Press; 2015:25–57. https://doi.org/10.1016/bs.ctm.2015.03.009.
32. Risselada HJ, Marrink SJ. The molecular face of lipid rafts in model membranes. *Proc Natl Acad Sci*. 2008;105(45):17367–17372. https://doi.org/10.1073/pnas.0807527105.
33. Ingólfsson HI, Melo MN, van Eerden FJ, et al. Lipid organization of the plasma membrane. *J Am Chem Soc*. 2014;136(41):14554–14559. https://doi.org/10.1021/ja507832e.
34. Lingwood D, Simons K. Lipid rafts as a membrane-organizing principle. *Science*. 2010;327(5961):46–50. https://doi.org/10.1126/science.1174621.
35. Muller MP, Jiang T, Sun C, et al. Characterization of lipid-protein interactions and lipid-mediated modulation of membrane protein function through molecular simulation. *Chem Rev*. 2019;119(9):6086–6161. https://doi.org/10.1021/acs.chemrev.8b00608.
36. Laursen M, Yatime L, Nissen P, Fedosova NU. Crystal structure of the high-affinity Na+, K+-ATPase-ouabain complex with Mg2+ bound in the cation binding site. *Proc Natl Acad Sci USA*. 2013;110(27):10958–10963. https://doi.org/10.1073/pnas.1222308110.
37. Hanson MA, Cherezov V, Griffith MT, et al. A specific cholesterol binding site is established by the 2.8 Å structure of the human β2-adrenergic receptor. *Structure*. 2008;16(6):897–905. https://doi.org/10.1016/j.str.2008.05.001.
38. Efremov RG, Sazanov LA. Structure of Escherichia coli OmpF porin from lipidic mesophase. *J Struct Biol*. 2012;178(3):311–318. https://doi.org/10.1016/j.jsb.2012.03.005.
39. Strandberg E, Esteban-Martín S, Ulrich AS, Salgado J. Hydrophobic mismatch of mobile transmembrane helices: merging theory and experiments. *Biochim Biophys Acta Biomembr*. 2012;1818(5):1242–1249. https://doi.org/10.1016/j.bbamem.2012.01.023.
40. Marinko JT, Huang H, Penn WD, Capra JA, Schlebach JP, Sanders CR. Folding and misfolding of human membrane proteins in health and disease: from single molecules to cellular proteostasis. *Chem Rev*. 2019;119(9):5537–5606. https://doi.org/10.1021/acs.chemrev.8b00532.
41. Murata K, Wolf M. Cryo-electron microscopy for structural analysis of dynamic biological macromolecules. *Biochim Biophys Acta Gen Subj*. 2018;1862(2):324–334. https://doi.org/10.1016/j.bbagen.2017.07.020.

42. Berman HM, Westbrook J, Feng Z, et al. The protein data bank. *Nucleic Acids Res*. 2000;28(1):235–242. https://doi.org/10.1093/nar/28.1.235.
43. Burley SK, Berman HM, Bhikadiya C, et al. RCSB protein data bank: biological macromolecular structures enabling research and education in fundamental biology, biomedicine, biotechnology and energy. *Nucleic Acids Res*. 2018;47(D1):D464–D474. https://doi.org/10.1093/nar/gky1004.
44. Lomize MA, Lomize AL, Pogozheva ID, Mosberg HI. OPM: orientations of proteins in membranes database. *Bioinformatics*. 2006;22(5):623–625. https://doi.org/10.1093/bioinformatics/btk023.
45. Kox A, Michels J, Wiegel F. Simulation of a lipid monolayer using molecular dynamics. *Nature*. 1980;287:317–319. https://doi.org/10.1038/287317a0.
46. van der Ploeg P, Berendsen HJC. Molecular dynamics simulation of a bilayer membrane. *J Chem Phys*. 1982;76(6):3271–3276. https://doi.org/10.1063/1.443321.
47. van der Ploeg P, Berendsen HJC. Molecular dynamics of a bilayer membrane. *Mol Phys*. 1983;49(1):233–248. https://doi.org/10.1080/00268978300101131.
48. Marrink SJ, Berendsen HJC. Simulation of water transport through a lipid membrane. *J Phys Chem*. 1994;98(15):4155–4168. https://doi.org/10.1021/j100066a040.
49. Tieleman DP, Berendsen HJC. Molecular dynamics simulations of a fully hydrated dipalmitoylphosphatidylcholine bilayer with different macroscopic boundary conditions and parameters. *J Chem Phys*. 1996;105(11):4871–4880. https://doi.org/10.1063/1.472323.
50. Heller H, Schaefer M, Schulten K. Molecular dynamics simulation of a bilayer of 200 lipids in the gel and in the liquid crystal phase. *J Phys Chem*. 1993;97(31):8343–8360. https://doi.org/10.1021/j100133a034.
51. Damodaran KV, Merz Jr KM, Gaber BP. Structure and dynamics of the dilauroylphosphatidylethanolamine lipid bilayer. *Biochemistry*. 1992;31(33):7656–7664. https://doi.org/10.1021/bi00148a029.
52. Damodaran KV, Merz Jr KM. Head group-water interactions in lipid bilayers: a comparison between DMPC- and DLPE-based lipid bilayers. *Langmuir*. 1993;9(5):1179–1183. https://doi.org/10.1021/la00029a005.
53. Edholm O, Johansson J. Lipid bilayer polypeptide interactions studied by molecular dynamics simulation. *Eur Biophys J*. 1987;14(4):203–209. https://doi.org/10.1007/BF00256353.
54. Zhou F, Schulten K. Molecular dynamics study of phospholipase A2 on a membrane surface. *Proteins*. 1996;25(1):12–27. https://doi.org/10.1002/(SICI)1097-0134(199605)25:13.0.CO;2-M.
55. Woolf TB, Roux B. Molecular dynamics simulation of the gramicidin channel in a phospholipid bilayer. *Proc Natl Acad Sci*. 1994;91(24):11631–11635. https://doi.org/10.1073/pnas.91.24.11631.
56. Zhong Q, Jiang Q, Moore PB, Newns DM, Klein ML. Molecular dynamics simulation of a synthetic ion channel. *Biophys J*. 1998;74(1):3–10. https://doi.org/10.1016/S0006-3495(98)77761-6.
57. Perilla JR, Goh BC, Cassidy CK, et al. Molecular dynamics simulations of large macromolecular complexes. *Curr Opin Struct Biol*. 2015;31:64–74. https://doi.org/10.1016/j.sbi.2015.03.007.
58. Li J, Lü S, Liu Y, et al. Identification of the conformational transition pathway in PIP$_2$ opening Kir channels. *Sci Rep*. 2015;1858(7, Pt. B):1610–1618. https://doi.org/10.1038/srep11289.
59. Kirsch SA, Böckmann RA. Membrane pore formation in atomistic and coarse-grained simulations. *Biochim Biophys Acta Biomembr*. 2016;1858(10):2266–2277. https://doi.org/10.1016/j.bbamem.2015.12.031.

60. Reddy T, Sansom MSP. Computational virology: from the inside out. *Biochim Biophys Acta Biomembr*. 2016;1858(7, Part B):1610–1618. https://doi.org/10.1016/j.bbamem.2016.02.007.
61. Marrink SJ, Corradi V, Souza PCT, et al. Computational modeling of realistic cell membranes. *Chem Rev*. 2019;119(9):6184–6226. https://doi.org/10.1021/acs.chemrev.8b00460.
62. Marrink SJ, de Vries AH, Mark AE. Coarse grained model for semiquantitative lipid simulations. *J Phys Chem B*. 2004;108(2):750–760. https://doi.org/10.1021/jp036508g.
63. Marrink SJ, Risselada HJ, Yefimov S, Tieleman DP, de Vries AH. The MARTINI force field: coarse grained model for biomolecular simulations. *J Phys Chem B*. 2007;111(27):7812–7824. https://doi.org/10.1021/jp071097f.
64. Ohkubo YZ, Pogorelov TV, Arcario MJ, Christensen GA, Tajkhorshid E. Accelerating membrane insertion of peripheral proteins with a novel membrane mimetic model. *Biophys J*. 2012;102(9):2130–2139. https://doi.org/10.1016/j.bpj.2012.03.015.
65. Kmiecik S, Gront D, Kolinski M, Wieteska L, Dawid AE, Kolinski A. Coarse-grained protein models and their applications. *Chem Rev*. 2016;116(14):7898–7936. https://doi.org/10.1021/acs.chemrev.6b00163.
66. Dutzler R, Campbell EB, MacKinnon R. Gating the selectivity filter in ClC chloride channels. *Science*. 2003;300(5616):108–112. https://doi.org/10.1126/science.1082708.
67. Schlenkrich M, Brickmann J, MacKerell Jr AD, Karplus M. An empirical potential energy function for phospholipids: criteria for parameter optimization and applications. In: Merz Jr. KM, Roux B, eds. *Biological Membranes: A Molecular Perspective From Computation and Experiment*. Boston, MA: Birkhäuser Boston; 1996:31–81. https://doi.org/10.1007/978-1-4684-8580-6_2.
68. Feller SE, Yin D, Pastor RW, MacKerell Jr AD. Molecular dynamics simulation of unsaturated lipid bilayers at low hydration: parameterization and comparison with diffraction studies. *Biophys J*. 1997;73(5):2269–2279. https://doi.org/10.1016/S0006-3495(97)78259-6.
69. Feller SE, MacKerell Jr AD. An improved empirical potential energy function for molecular simulations of phospholipids. *J Phys Chem B*. 2000;104(31):7510–7515. https://doi.org/10.1021/jp0007843.
70. Klauda JB, Brooks BR, MacKerell Jr AD, Venable RM, Pastor RW. An ab initio study on the torsional surface of alkanes and its effect on molecular simulations of alkanes and a DPPC bilayer. *J Phys Chem B*. 2005;109(11):5300–5311. https://doi.org/10.1021/jp0468096.
71. Klauda JB, Pastor RW, Brooks BR. Adjacent gauche stabilization in linear alkanes: implications for polymer models and conformational analysis. *J Phys Chem B*. 2005;109(33):15684–15686. https://doi.org/10.1021/jp0527608.
72. Zhuang X, Dávila-Contreras EM, Beaven AH, Beaven AH, Im W, Klauda JB. An extensive simulation study of lipid bilayer properties with different head groups, acyl chain lengths, and chain saturations. *Biochim Biophys Acta Biomembr*. 2016;1858(12):3093–3104. https://doi.org/10.1016/j.bbamem.2016.09.016.
73. Klauda JB, Venable RM, Freites JA, et al. Update of the CHARMM all-atom additive force field for lipids: validation on six lipid types. *J Phys Chem B*. 2010;114(23):7830–7843. https://doi.org/10.1021/jp101759q.
74. Lee S, Tran A, Allsopp M, Lim JB, Hnin J, Klauda JB. CHARMM36 united atom chain model for lipids and surfactants. *J Phys Chem B*. 2014;118(2):547–556. https://doi.org/10.1021/jp410344g.

75. Jójárt B, Martinek TA. Performance of the general amber force field in modeling aqueous POPC membrane bilayers. *J Comput Chem*. 2007;28(12):2051–2058. https://doi.org/10.1002/jcc.20748.
76. Rosso L, Gould IR. Structure and dynamics of phospholipid bilayers using recently developed general all-atom force fields. *J Comput Chem*. 2008;29(1):24–37. https://doi.org/10.1002/jcc.20675.
77. Skjevik ÅA, Madej BD, Walker RC, Teigen K. Lipid11: a modular framework for lipid simulations using amber. *J Phys Chem B*. 2012;116(36):11124–11136. https://doi.org/10.1021/jp3059992.
78. Dickson CJ, Madej BD, Skjevik ÅA, et al. Lipid14: the amber lipid force field. *J Chem Theory Comput*. 2014;10(2):865–879. https://doi.org/10.1021/ct4010307.
79. Jämbeck JPM, Lyubartsev AP. An extension and further validation of an all-atomistic force field for biological membranes. *J Chem Theory Comput*. 2012;8(8):2938–2948. https://doi.org/10.1021/ct300342n.
80. Jämbeck JPM, Lyubartsev AP. Another piece of the membrane puzzle: extending slipids further. *J Chem Theory Comput*. 2013;9(1):774–784. https://doi.org/10.1021/ct300777p.
81. Pasenkiewicz-Gierula M, Takaoka Y, Miyagawa H, Kitamura K, Kusumi A. Charge pairing of headgroups in phosphatidylcholine membranes: a molecular dynamics simulation study. *Biophys J*. 1999;76(3):1228–1240. https://doi.org/10.1016/S0006-3495(99)77286-3.
82. Pasenkiewicz-Gierula M, Róg T, Kitamura K, Kusumi A. Cholesterol effects on the phosphatidylcholine bilayer polar region: a molecular simulation study. *Biophys J*. 2000;78(3):1376–1389. https://doi.org/10.1016/S0006-3495(00)76691-4.
83. Maciejewski A, Pasenkiewicz-Gierula M, Cramariuc O, Vattulainen I, Rog T. Refined OPLS all-atom force field for saturated phosphatidylcholine bilayers at full hydration. *J Phys Chem B*. 2014;118(17):4571–4581. https://doi.org/10.1021/jp5016627.
84. Berger O, Edholm O, Jähnig F. Molecular dynamics simulations of a fluid bilayer of dipalmitoylphosphatidylcholine at full hydration, constant pressure, and constant temperature. *Biophys J*. 1997;72(5):2002–2013. https://doi.org/10.1016/S0006-3495(97)78845-3.
85. Chiu SW, Clark MM, Jakobsson E, Subramaniam S, Scott HL. Optimization of hydrocarbon chain interaction parameters: application to the simulation of fluid phase lipid bilayers. *J Phys Chem B*. 1999;103(30):6323–6327. https://doi.org/10.1021/jp983219x.
86. Chandrasekhar I, Kastenholz M, Lins RD, et al. A consistent potential energy parameter set for lipids: dipalmitoylphosphatidylcholine as a benchmark of the GROMOS96 45A3 force field. *Eur Biophys J*. 2003;32(1):67–77.
87. Oostenbrink C, Villa A, Mark AE, Van Gunsteren WF. A biomolecular force field based on the free enthalpy of hydration and solvation: the GROMOS force-field parameter sets 53A5 and 53A6. *J Comput Chem*. 2004;25(13):1656–1676. https://doi.org/10.1002/jcc.20090.
88. Kukol A. Lipid models for united-atom molecular dynamics simulations of proteins. *J Chem Theory Comput*. 2009;5(3):615–626. https://doi.org/10.1021/ct8003468.
89. Piggot TJ, Holdbrook DA, Khalid S. Electroporation of the E. coli and S. Aureus membranes: molecular dynamics simulations of complex bacterial membranes. *J Phys Chem B*. 2011;115(45):13381–13388. https://doi.org/10.1021/jp207013v.
90. Piggot TJ, Piñeiro A, Khalid S. Molecular dynamics simulations of phosphatidylcholine membranes: a comparative force field study. *J Chem Theory Comput*. 2012;8(11):4593–4609. https://doi.org/10.1021/ct3003157.

91. Schmid N, Eichenberger AP, Choutko A, et al. Definition and testing of the GROMOS force-field versions 54A7 and 54B7. *Eur Biophys J*. 2011;40(7):843. https://doi.org/10.1007/s00249-011-0700-9.
92. Shinoda W, DeVane R, Klein ML. Multi-property fitting and parameterization of a coarse grained model for aqueous surfactants. *Mol Simul*. 2007;33(1–2):27–36. https://doi.org/10.1080/08927020601054050.
93. Shinoda W, DeVane R, Klein ML. Zwitterionic lipid assemblies: molecular dynamics studies of monolayers, bilayers, and vesicles using a new coarse grain force field. *J Phys Chem B*. 2010;114(20):6836–6849. https://doi.org/10.1021/jp9107206.
94. T Darden DY, Pedersen L. Particle mesh Ewald: an N·Log(N) method for Ewald sums in large systems. *J Chem Phys*. 1993;98(12):10089–10092.
95. Essmann U, Perera L, Berkowitz ML. A smooth particle mesh Ewald method. *J Chem Phys*. 1995;103(19):8577–8593.
96. Poger D, Caron B, Mark AE. Validating lipid force fields against experimental data: progress, challenges and perspectives. *Biochim Biophys Acta Biomembr*. 2016;1858 (7, Pt. B):1556–1565. https://doi.org/10.1016/j.bbamem.2016.01.029.
97. Leonard AN, Wang E, Monje-Galvan V, Klauda JB. Developing and testing of lipid force fields with applications to modeling cellular membranes. *Chem Rev*. 2019;119(9):6227–6269. https://doi.org/10.1021/acs.chemrev.8b00384.
98. Moradi S, Nowroozi A, Shahlaei M. Shedding light on the structural properties of lipid bilayers using molecular dynamics simulation: a review study. *RSC Adv*. 2019;9(8):4644–4658. https://doi.org/10.1039/C8RA08441F.
99. Falck E, Patra M, Karttunen M, Hyvönen MT, Vattulainen I. Lessons of slicing membranes: interplay of packing, free area, and lateral diffusion in phospholipid/cholesterol bilayers. *Biophys J*. 2004;87(2):1076–1091. https://doi.org/10.1529/biophysj.104.041368.
100. Mori T, Ogushi F, Sugita Y. Analysis of lipid surface area in protein-membrane systems combining Voronoi tessellation and Monte Carlo integration methods. *J Comput Chem*. 2012;33(3):286–293. https://doi.org/10.1002/jcc.21973.
101. Lukat G, Krüger J, Sommer B. APL@Voro: a voronoi-based membrane analysis tool for GROMACS trajectories. *J Chem Inf Model*. 2013;53(11):2908–2925. https://doi.org/10.1021/ci400172g.
102. Poger D, Mark AE. The relative effect of sterols and hopanoids on lipid bilayers: when comparable is not identical. *J Phys Chem B*. 2013;117(50):16129–16140. https://doi.org/10.1021/jp409748d.
103. Petrache HI, Tristram-Nagle S, Nagle JF. Fluid phase structure of EPC and DMPC bilayers. *Chem Phys Lipids*. 1998;95(1):83–94. https://doi.org/10.1016/S0009-3084(98)00068-1.
104. Kučerka N, Gallová J, Uhríková D, et al. Areas of monounsaturated diacylphosphatidylcholines. *Biophys J*. 2009;97(7):1926–1932. https://doi.org/10.1016/j.bpj.2009.06.050.
105. Leftin A, Brown MF. An NMR database for simulations of membrane dynamics. *Biochim Biophys Acta Biomembr*. 2011;1808(3):818–839. https://doi.org/10.1016/j.bbamem.2010.11.027.
106. Vaz WL, Almeida PF. Microscopic versus macroscopic diffusion in one-component fluid phase lipid bilayer membranes. *Biophys J*. 1991;60(6):1553–1554. https://doi.org/10.1016/S0006-3495(91)82190-7.
107. Raman EP, Guvench O, MacKerell Jr AD. CHARMM additive all-atom force field for glycosidic linkages in carbohydrates involving furanoses. *J Phys Chem B*. 2010;114(40):12981–12994. https://doi.org/10.1021/jp105758h.
108. Guvench O, Hatcher E, Venable RM, Pastor RW, MacKerell Jr AD. CHARMM additive all-atom force field for glycosidic linkages between hexopyranoses. *J Chem Theory Comput*. 2009;5(9):2353–2370. https://doi.org/10.1021/ct900242e.

109. Guvench O, Mallajosyula SS, Raman EP, et al. Charmm additive all-atom force field for carbohydrate derivatives and its utility in polysaccharide and carbohydrate-protein modeling. *J Chem Theory Comput*. 2011;7(10):3162–3180. https://doi.org/10.1021/ct200328p.
110. Mallajosyula SS, Guvench O, Hatcher E, MacKerell Jr AD. CHARMM additive all-atom force field for phosphate and sulfate linked to carbohydrates. *J Chem Theory Comput*. 2012;8(2):759–776. https://doi.org/10.1021/ct200792v.
111. Hart K, Foloppe N, Baker CM, Denning EJ, Nilsson L, MacKerell Jr AD. Optimization of the CHARMM additive force field for DNA: improved treatment of the BI/BII conformational equilibrium. *J Chem Theory Comput*. 2012;8(1):348–362. https://doi.org/10.1021/ct200723y.
112. Denning EJ, Priyakumar UD, Nilsson L, Mackerell Jr AD. Impact of 2′-hydroxyl sampling on the conformational properties of RNA: update of the CHARMM all-atom additive force field for RNA. *J Comput Chem*. 2011;32(9):1929–1943. https://doi.org/10.1002/jcc.21777.
113. Huang J, MacKerell Jr AD. CHARMM36 all-atom additive protein force field: validation based on comparison to NMR data. *J Comput Chem*. 2013;34(25):2135–2145. https://doi.org/10.1002/jcc.23354.
114. Huang J, Rauscher S, Nawrocki G, et al. Charmm36m: an improved force field for folded and intrinsically disordered proteins. *Nat Methods*. 2017;14(1):71.
115. Vanommeslaeghe K, Hatcher E, Acharya C, et al. CHARMM general force field: a force field for drug-like molecules compatible with the CHARMM all-atom additive biological force fields. *J Comput Chem*. 2010;31(4):671–690. https://doi.org/10.1002/jcc.21367.
116. Benz RW, Castro-Román F, Tobias DJ, White SH. Experimental validation of molecular dynamics simulations of lipid bilayers: a new approach. *Biophys J*. 2005;88(2):805–817. https://doi.org/10.1529/biophysj.104.046821.
117. Strader ML, Feller SE. A flexible all-atom model of dimethyl sulfoxide for molecular dynamics simulations. *J Phys Chem A*. 2002;106(6):1074–1080. https://doi.org/10.1021/jp013658n.
118. Jensen MØ, Mouritsen OG, Peters GH. Simulations of a membrane-anchored peptide: structure, dynamics, and influence on bilayer properties. *Biophys J*. 2004;86(6):3556–3575. https://doi.org/10.1529/biophysj.103.029140.
119. Prakash P, Sankararamakrishnan R. Force field dependence of phospholipid headgroup and acyl chain properties: comparative molecular dynamics simulations of DMPC bilayers. *J Comput Chem*. 2010;31(2):266–277. https://doi.org/10.1002/jcc.21313.
120. Högberg CJ, Nikitin AM, Lyubartsev AP. Modification of the CHARMM force field for DMPC lipid bilayer. *J Comput Chem*. 2008;29(14):2359–2369. https://doi.org/10.1002/jcc.20974.
121. Klauda JB, Kučerka N, Brooks BR, Pastor RW, Nagle JF. Simulation-based methods for interpreting X-ray data from lipid bilayers. *Biophys J*. 2006;90(8):2796–2807. https://doi.org/10.1529/biophysj.105.075697.
122. Sonne J, Jensen MØ, Hansen FY, Hemmingsen L, Peters GH. Reparameterization of all-atom dipalmitoylphosphatidylcholine lipid parameters enables simulation of fluid bilayers at zero tension. *Biophys J*. 2007;92(12):4157–4167. https://doi.org/10.1529/biophysj.106.087130.
123. Klauda JB, Monje V, Kim T, Im W. Improving the CHARMM force field for polyunsaturated fatty acid chains. *J Phys Chem B*. 2012;116(31):9424–9431. https://doi.org/10.1021/jp304056p.
124. Lim JB, Klauda JB. Lipid chain branching at the iso- and anteiso-positions in complex chlamydia membranes: a molecular dynamics study. *Biochim Biophys Acta Biomembr*. 2011;1808(1):323–331. https://doi.org/10.1016/j.bbamem.2010.07.036.

125. Pandit KR, Klauda JB. Membrane models of E. coli containing cyclic moieties in the aliphatic lipid chain. *Biochim Biophys Acta Biomembr*. 2012;1818(5):1205–1210. https://doi.org/10.1016/j.bbamem.2012.01.009.
126. Wu EL, Fleming PJ, Yeom MS, et al. E. coli outer membrane and interactions with OmpLA. *Biophys J*. 2014;106(11):2493–2502. https://doi.org/10.1016/j.bpj.2014.04.024.
127. Kang H, Klauda JB. Molecular dynamics simulations of palmitoyloleoylphosphatidylglycerol bilayers. *Mol Simul*. 2015;41(10–12):948–954. https://doi.org/10.1080/08927022.2014.926548.
128. Lim JB, Rogaski B, Klauda JB. Update of the cholesterol force field parameters in CHARMM. *J Phys Chem B*. 2012;116(1):203–210. https://doi.org/10.1021/jp207925m.
129. Monje-Galvan V, Klauda JB. Modeling yeast organelle membranes and how lipid diversity influences bilayer properties. *Biochemistry*. 2015;54(45):6852–6861. https://doi.org/10.1021/acs.biochem.5b00718.
130. Zhuang X, Ou A, Klauda JB. Simulations of simple linoleic acid-containing lipid membranes and models for the soybean plasma membranes. *J Chem Phys*. 2017;146(21):215103. https://doi.org/10.1063/1.4983655.
131. Venable RM, Sodt AJ, Rogaski B, et al. CHARMM all-atom additive force field for sphingomyelin: elucidation of hydrogen bonding and of positive curvature. *Biophys J*. 2014;107(1):134–145. https://doi.org/10.1016/j.bpj.2014.05.034.
132. Wang E, Klauda JB. Molecular dynamics simulations of ceramide and ceramide-phosphatidylcholine bilayers. *J Phys Chem B*. 2017;121(43):10091–10104. https://doi.org/10.1021/acs.jpcb.7b08967.
133. Patel DS, Park S, Wu EL, et al. Influence of ganglioside GM1 concentration on lipid clustering and membrane properties and curvature. *Biophys J*. 2016;111(9):1987–1999. https://doi.org/10.1016/j.bpj.2016.09.021.
134. Kim S, Patel DS, Park S, et al. Bilayer properties of lipid A from various gram-negative bacteria. *Biophys J*. 2016;111(8):1750–1760. https://doi.org/10.1016/j.bpj.2016.09.001.
135. Wang J, Wolf RM, Caldwell JW, Kollman PA, Case DA. Development and testing of a general amber force field. *J Comput Chem*. 2004;25(9):1157–1174. https://doi.org/10.1002/jcc.20035.
136. Bayly CI, Cieplak P, Cornell WD, Kollman PA. A well-behaved electrostatic potential based method using charge restraints for deriving atomic charges: the RESP model. *J Phys Chem*. 1993;97(2):10269–10280.
137. Cornell WD, Cieplak P, Bayly CI, Kollman PA. Application of RESP charges to calculate conformational energies, hydrogen bond energies, and free energies of solvation. *J Phys Chem*. 1993;115(21):9620–9631.
138. Dickson CJ, Rosso L, Betz RM, Walker RC, Gould IR. GAFFlipid: a general amber force field for the accurate molecular dynamics simulation of phospholipid. *Soft Matter*. 2012;8:9617–9627. https://doi.org/10.1039/C2SM26007G.
139. Kirschner KN, Yongye AB, Tschampel SM, et al. GLYCAM06: a generalizable biomolecular force field. Carbohydrates. *J Comput Chem*. 2008;29(4):622–655. https://doi.org/10.1002/jcc.20820.
140. Madej BD, Gould IR, Walker RC. A parameterization of cholesterol for mixed lipid bilayer simulation within the amber Lipid14 force field. *J Phys Chem B*. 2015;119(38):12424–12435. https://doi.org/10.1021/acs.jpcb.5b04924.
141. Gould I, Skjevik A, Dickson C, et al. Lipid17: a comprehensive AMBER Force field for the simulation of zwitterionic and anionic lipids; 2018. [in prep.].
142. Jämbeck JPM, Lyubartsev AP. Derivation and systematic validation of a refined all-atom force field for phosphatidylcholine lipids. *J Phys Chem B*. 2012;116(10):3164–3179. https://doi.org/10.1021/jp212503e.

143. Jämbeck JPM, Lyubartsev AP. Exploring the free energy landscape of solutes embedded in lipid bilayers. *J Phys Chem Lett.* 2013;4(11):1781–1787. https://doi.org/10.1021/jz4007993.
144. Paloncýová M, Fabre G, DeVane RH, Trouillas P, Berka K, Otyepka M. Benchmarking of force fields for molecule-membrane interactions. *J Chem Theory Comput.* 2014;10(9):4143–4151. https://doi.org/10.1021/ct500419b.
145. Jorgensen WL, Maxwell DS, Tirado-Rives J. Development and testing of the OPLS all-atom force field on conformational energetics and properties of organic liquids. *J Am Chem Soc.* 1996;118(45):11225–11236. https://doi.org/10.1021/ja9621760.
146. Jorgensen WL, Tirado-Rives J. The OPLS [optimized potentials for liquid simulations] potential functions for proteins, energy minimizations for crystals of cyclic peptides and crambin. *J Am Chem Soc.* 1988;110(6):1657–1666. https://doi.org/10.1021/ja00214a001.
147. Damm W, Frontera A, Tirado-Rives J, Jorgensen WL. Opls all-atom force field for carbohydrates. *J Comput Chem.* 1997;18(16):1955–1970. https://doi.org/10.1002/(SICI)1096-987X(199712)18:163.0.CO;2-L.
148. Kaminski GA, Friesner RA, Tirado-Rives J, Jorgensen WL. Evaluation and reparametrization of the OPLS-AA force field for proteins via comparison with accurate quantum chemical calculations on peptides. *J Phys Chem B.* 2001;105(28): 6474–6487. https://doi.org/10.1021/jp003919d.
149. Ulmschneider JP, Jorgensen WL. Monte Carlo backbone sampling for nucleic acids using concerted rotations including variable bond angles. *J Phys Chem B.* 2004;108(43):16883–16892. https://doi.org/10.1021/jp047796z.
150. Kulig W, Pasenkiewicz-Gierula M, Róg T. Cis and trans unsaturated phosphatidylcholine bilayers: a molecular dynamics simulation study. *Chem Phys Lipids.* 2016;195:12–20. https://doi.org/10.1016/j.chemphyslip.2015.07.002.
151. Kulig W, Pasenkiewicz-Gierula M, Róg T. Topologies, structures and parameter files for lipid simulations in GROMACS with the OPLS-aa force field: DPPC, POPC, DOPC, PEPC, and cholesterol. *Data Brief.* 2015;5:333–336. https://doi.org/10.1016/j.dib.2015.09.013.
152. Rog T, Koivuniemi A. The biophysical properties of ethanolamine plasmalogens revealed by atomistic molecular dynamics simulations. *Biochim Biophys Acta Biomembr.* 2016;1858(1):97–103. https://doi.org/10.1016/j.bbamem.2015.10.023. (a) Róg T, Orłowski A, Llorente A, et al. Data including GROMACS input files for atomistic molecular dynamics simulations of mixed, asymmetric bilayers including molecular topologies, equilibrated structures, and force field for lipids compatible with OPLS-AA parameters. *Data in Brief.* 2016;7:1171–1174. issn: 2352-3409. https://doi.org/10.1016/j.dib.2016.03.067. (b) Grabon A, Orłowski A, Tripathi A, et al. Dynamics and energetics of the mammalian phosphatidylinositol transfer protein phospholipid exchange cycle. *J Biol Chem.* 2017;292(35):14438–14455. https://doi.org/10.1074/jbc.M117.791467. (c) Manna M, Javanainen M, Martinez-Seara Monne H, et al. Long-chain GM1 gangliosides alter transmembrane domain registration through interdigitation. *Biochim Biophys Acta Biomembr.* 2017;1859(5):870–878. issn: 0005-2736. https://doi.org/10.1016/j.bbamem.2017.01.033. (d) 152d Owen MC, Kulig W, Rog T, et al. Cholesterol protects the oxidized lipid bilayer from water injury: an all-atom molecular dynamics study. *J Membr Biol.* 2018;251(3):521–534.
153. Róg T, Pasenkiewicz-Gierula M. Effects of epicholesterol on the phosphatidylcholine bilayer: a molecular simulation study. *Biophys J.* 2003;84(3):1818–1826. https://doi.org/10.1016/S0006-3495(03)74989-3.
154. Poger D, Van Gunsteren WF, Mark AE. A new force field for simulating phosphatidylcholine bilayers. *J Comput Chem.* 2010;31(6):1117–1125. https://doi.org/10.1002/jcc.21396.

155. Anézo C, de Vries AH, Höltje HD, Tieleman DP, Marrink SJ. Methodological issues in lipid bilayer simulations. *J Phys Chem B*. 2003;107(35):9424–9433. https://doi.org/10.1021/jp0348981.
156. Siu SWI, Vácha R, Jungwirth P, Böckmann RA. Biomolecular simulations of membranes: physical properties from different force fields. *J Chem Phys*. 2008;128(12):125103. https://doi.org/10.1063/1.2897760.
157. Tjörnhammar R, Edholm O. Reparameterized united atom model for molecular dynamics simulations of gel and fluid phosphatidylcholine bilayers. *J Chem Theory Comput*. 2014;10(12):5706–5715. https://doi.org/10.1021/ct500589z.
158. Chiu SW, Pandit SA, Scott HL, Jakobsson E. An improved united atom force field for simulation of mixed lipid bilayers. *J Phys Chem B*. 2009;113(9):2748–2763. https://doi.org/10.1021/jp807056c.
159. Poger D, Mark AE. On the validation of molecular dynamics simulations of saturated and cis-monounsaturated phosphatidylcholine lipid bilayers: a comparison with experiment. *J Chem Theory Comput*. 2010;6(1):325–336. https://doi.org/10.1021/ct900487a.
160. Poger D, Caron B, Mark AE. Effect of methyl-branched fatty acids on the structure of lipid bilayers. *J Phys Chem B*. 2014;118(48):13838–13848. https://doi.org/10.1021/jp503910r.
161. Poger D, Mark AE. A ring to rule them all: the effect of cyclopropane fatty acids on the fluidity of lipid bilayers. *J Phys Chem B*. 2015;119(17):5487–5495. https://doi.org/10.1021/acs.jpcb.5b00958.
162. Caron B, Mark AE, Poger D. Some like it hot: the effect of sterols and hopanoids on lipid ordering at high temperature. *J Phys Chem Lett*. 2014;5(22):3953–3957. https://doi.org/10.1021/jz5020778.
163. Mori T, Jung J, Sugita Y. Surface-tension replica-exchange molecular dynamics method for enhanced sampling of biological membrane systems. *J Chem Theory Comput*. 2013;9(12):5629–5640. https://doi.org/10.1021/ct400445k.
164. Lee CT, Comer J, Herndon C, et al. Simulation-based approaches for determining membrane permeability of small compounds. *J Chem Inf Model*. 2016;56(4):721–733. https://doi.org/10.1021/acs.jcim.6b00022.
165. Cao Z, Bian Y, Hu G, et al. Bias-exchange metadynamics simulation of membrane permeation of 20 amino acids. *Int J Mol Sci*. 2018;19(3). https://doi.org/10.3390/ijms19030885. https://www.mdpi.com/1422-0067/19/3/885.
166. Ohkubo YZ, Tajkhorshid E. Distinct structural and adhesive roles of Ca^{2+} in membrane binding of blood coagulation factors. *Structure*. 2008;16(1):72–81. https://doi.org/10.1016/j.str.2007.10.021.
167. Muller MP, Wang Y, Morrissey JH, Tajkhorshid E. Lipid specificity of the membrane binding domain of coagulation factor x. *J Thromb Haemost*. 2017;15(10):2005–2016. https://doi.org/10.1111/jth.13788.
168. Baylon JL, Lenov IL, Sligar SG, Tajkhorshid E. Characterizing the membrane-bound state of cytochrome P450 3A4: structure, depth of insertion, and orientation. *J Am Chem Soc*. 2013;135(23):8542–8551. https://doi.org/10.1021/ja4003525.
169. Blanchard AE, Arcario MJ, Schulten K, et al. A highly tilted membrane configuration for the prefusion state of synaptobrevin. *Biophys J*. 2014;107(9):2112–2121. https://doi.org/10.1016/j.bpj.2014.09.013.
170. Pogorelov TV, Vermaas JV, Arcario MJ, Tajkhorshid E. Partitioning of amino acids into a model membrane: capturing the interface. *J Phys Chem B*. 2014;118(6):1481–1492. https://doi.org/10.1021/jp4089113.
171. Vermaas JV, Tajkhorshid E. Conformational heterogeneity of α-synuclein in membrane. *Biochim Biophys Acta Biomembr*. 2014;1838(12):3107–3117. https://doi.org/10.1016/j.bbamem.2014.08.012.

172. Christensen M, Skeby KK, Schiøtt B. Identification of key interactions in the initial self-assembly of amylin in a membrane environment. *Biochemistry*. 2017;56(36): 4884–4894. https://doi.org/10.1021/acs.biochem.7b00344.
173. Vermaas JV, Pogorelov TV, Tajkhorshid E. Extension of the highly mobile membrane mimetic to transmembrane systems through customized in silico solvents. *J Phys Chem B*. 2017;121(15):3764–3776. https://doi.org/10.1021/acs.jpcb.6b11378.
174. Lyubartsev AP, Rabinovich AL. Force field development for lipid membrane simulations. *Biochim Biophys Acta Biomembr*. 2016;1858(10):2483–2497. https://doi.org/10.1016/j.bbamem.2015.12.033.
175. Skjevik ÅA, Madej BD, Dickson CJ, Teigen K, Walker RC, Gould IR. All-atom lipid bilayer self-assembly with the AMBER and CHARMM lipid force fields. *Chem Commun*. 2015;51:4402–4405. https://doi.org/10.1039/C4CC09584G.
176. Marrink SJ, Mark AE. Molecular dynamics simulation of the formation, structure, and dynamics of small phospholipid vesicles. *J Am Chem Soc*. 2003;125(49):15233–15242. https://doi.org/10.1021/ja0352092.
177. Monticelli L, Kandasamy SK, Periole X, Larson RG, Tieleman DP, Marrink SJ. The MARTINI coarse-grained force field: extension to proteins. *J Chem Theory Comput*. 2008;4(5):819–834. https://doi.org/10.1021/ct700324x.
178. Uusitalo JJ, Ingólfsson HI, Akhshi P, Tieleman DP, Marrink SJ. Martini coarse-grained force field: extension to DNA. *J Chem Theory Comput*. 2015;11(8):3932–3945. https://doi.org/10.1021/acs.jctc.5b00286.
179. Uusitalo JJ, Ingólfsson HI, Marrink SJ, Faustino I. Martini coarse-grained force field: extension to RNA. *Biophys J*. 2017;113(2):246–256. https://doi.org/10.1016/j.bpj.2017.05.043.
180. Marrink, S. J. Martini parameter for lipids. Accessed 05.11.10, http://cgmartini.nl/index.php/force-field-parameters/lipids.
181. Periole X. Interplay of G protein-coupled receptors with the membrane: insights from supra-atomic coarse grain molecular dynamics simulations. *Chem Rev*. 2017;117(1):156–185. https://doi.org/10.1021/acs.chemrev.6b00344.
182. Alessandri R, Souza PCT, Thallmair S, Melo MN, de Vries AH, Marrink SJ. Pitfalls of the martini model. *J Chem Theory Comput*. 2019;15(10):5448–5460. https://doi.org/10.1021/acs.jctc.9b00473.
183. Seo S, Shinoda W. SPICA force field for lipid membranes: domain formation induced by cholesterol. *J Chem Theory Comput*. 2018;15(1):762–774.
184. Orsi M, Essex JW. The ELBA force field for coarse-grain modeling of lipid membranes. *PLoS ONE*. 2011;6(12):e28637.
185. Barrera EE, Frigini EN, Porasso RD, Pantano S. Modeling DMPC lipid membranes with SIRAH force-field. *J Mol Model*. 2017;23(9):259. https://doi.org/10.1007/s00894-017-3426-5.
186. Liwo A, Baranowski M, Czaplewski C, et al. A unified coarse-grained model of biological macromolecules based on mean-field multipole-multipole interactions. *J Mol Model*. 2014;20(8):2306.
187. Jo S, Kim T, Iyer VG, Im W. CHARMM-GUI: a web-based graphical user interface for CHARMM. *J Comput Chem*. 2008;29(11):1859–1865. https://doi.org/10.1002/jcc.20945.
188. Jo S, Cheng X, Lee J, et al. CHARMM-GUI 10 years for biomolecular modeling and simulation. *J Comput Chem*. 2017;38(15):1114–1124. https://doi.org/10.1002/jcc.24660.
189. Brooks BR, Brooks IIICL, Mackerell Jr AD, et al. Charmm: the biomolecular simulation program. *J Comput Chem*. 2009;30(10):1545–1614. https://doi.org/10.1002/jcc.21287.

190. Abraham MJ, Murtola T, Schulz R, et al. GROMACS: high performance molecular simulations through multi-level parallelism from laptops to supercomputers. *SoftwareX*. 2015;1–2:19–25. https://doi.org/10.1016/j.softx.2015.06.001.
191. Pronk S, Páll S, Schulz R, et al. GROMACS 4.5: a high-throughput and highly parallel open source molecular simulation toolkit. *Bioinformatics*. 2013;29(7):845–854. https://doi.org/10.1093/bioinformatics/btt055.
192. Case DA, Cheatham IIITE, Darden T, et al. The Amber biomolecular simulation programs. *J Comput Chem*. 2005;26(16):1668–1688. https://doi.org/10.1002/jcc.20290.
193. Phillips JC, Braun R, Wang W, et al. Scalable molecular dynamics with NAMD. *J Comput Chem*. 2005;26(16):1781–1802. https://doi.org/10.1002/jcc.20289.
194. Jung J, Mori T, Kobayashi C, et al. Genesis: a hybrid-parallel and multi-scale molecular dynamics simulator with enhanced sampling algorithms for biomolecular and cellular simulations. *WIREs Comput Mol Sci*. 2015;5(4):310–323. https://doi.org/10.1002/wcms.1220.
195. Eastman P, Friedrichs MS, Chodera JD, et al. OpenMM 4: a reusable, extensible, hardware independent library for high performance molecular simulation. *J Chem Theory Comput*. 2013;9(1):461–469. https://doi.org/10.1021/ct300857j.
196. Arthur EJ, Brooks IIICL. Parallelization and improvements of the generalized born model with a simple switching function for modern graphics processors. *J Comput Chem*. 2016;37(10):927–939. https://doi.org/10.1002/jcc.24280.
197. Plimpton S. Fast parallel algorithms for short-range molecular dynamics. *J Comput Phys*. 1995;117(1):1–19. https://doi.org/10.1006/jcph.1995.1039.
198. Bowers KJ, Chow E, Xu H, et al. Scalable algorithms for molecular dynamics simulations on commodity clusters. In: *Proceedings of the 2006 ACM/IEEE Conference on Supercomputing*. New York, NY: ACM; 2006. https://doi.org/10.1145/1188455.1188544.
199. Lomize MA, Pogozheva ID, Joo H, Mosberg HI, Lomize AL. OPM database and PPM web server: resources for positioning of proteins in membranes. *Nucleic Acids Res*. 2011;40(D1):D370–D376. https://doi.org/10.1093/nar/gkr703.
200. Pourmousa M, Pastor RW. Molecular dynamics simulations of lipid nanodiscs. *Biochim Biophys Acta Biomembr*. 2018;1860(10):2094–2107. https://doi.org/10.1016/j.bbamem.2018.04.015.
201. Qi Y, Lee J, Klauda JB, Im W. CHARMM-GUI nanodisc builder for modeling and simulation of various nanodisc systems. *J Comput Chem*. 2019;40(7):893–899. https://doi.org/10.1002/jcc.25773.
202. Cheng X, Jo S, Lee HS, Klauda JB, Im W. CHARMM-GUI micelle builder for pure/mixed micelle and protein/micelle complex systems. *J Chem Inf Model*. 2013;53(8):2171–2180. https://doi.org/10.1021/ci4002684.
203. Rand RP, Fuller NL, Gruner SM, Parsegian VA. Membrane curvature, lipid segregation, and structural transitions for phospholipids under dual-solvent stress. *Biochemistry*. 1990;29(1):76–87. https://doi.org/10.1021/bi00453a010.
204. Chen Z, Rand RP. Comparative study of the effects of several n-alkanes on phospholipid hexagonal phases. *Biophys J*. 1998;74(2):944–952. https://doi.org/10.1016/S0006-3495(98)74017-2.
205. Sodt AJ, Pastor RW. Bending free energy from simulation: correspondence of planar and inverse hexagonal lipid phases. *Biophys J*. 2013;104(10):2202–2211. https://doi.org/10.1016/j.bpj.2013.03.048.
206. Qi Y, Cheng X, Lee J, Marrink SJ, Im W. CHARMM-GUI HMMM builder for membrane simulations with the highly mobile membrane-mimetic model. *Biophys J*. 2015;109(10):2012–2022.
207. Qi Y, Ingólfsson HI, Cheng X, Marrink SJ, Im W. CHARMM-GUI martini maker for coarse-grained simulations with the martini force field. *J Chem Theory Comput*. 2015;11(9):4486–4494. https://doi.org/10.1021/acs.jctc.5b00513.

208. Hsu PC, Bruininks BMH, Jefferies D, et al. CHARMM-GUI Martini maker for modeling and simulation of complex bacterial membranes with lipopolysaccharides. *J Comput Chem*. 2017;38(27):2354–2363. https://doi.org/10.1002/jcc.24895.
209. de Jong DH, Singh G, Bennett WFD, et al. Improved parameters for the martini coarse-grained protein force field. *J Chem Theory Comput*. 2013;9(1):687–697. https://doi.org/10.1021/ct300646g.
210. Yesylevskyy SO, Schäfer LV, Sengupta D, Marrink SJ. Polarizable water model for the coarse-grained MARTINI force field. *PLoS Comput Biol*. 2010;6(6):1–17. https://doi.org/10.1371/journal.pcbi.1000810.
211. Arnarez C, Uusitalo JJ, Masman MF, et al. Dry martini, a coarse-grained force field for lipid membrane simulations with implicit solvent. *J Chem Theory Comput*. 2015;11(1):260–275. https://doi.org/10.1021/ct500477k.
212. Periole X, Cavalli M, Marrink SJ, Ceruso MA. Combining an elastic network with a coarse-grained molecular force field: structure, dynamics, and intermolecular recognition. *J Chem Theory Comput*. 2009;5(9):2531–2543. https://doi.org/10.1021/ct9002114.
213. Wassenaar TA, Pluhackova K, Böckmann RA, Marrink SJ, Tieleman DP. Going backward: a flexible geometric approach to reverse transformation from coarse grained to atomistic models. *J Chem Theory Comput*. 2014;10(2):676–690. https://doi.org/10.1021/ct400617g.
214. Schott-Verdugo S, Gohlke H. PACKMOL-memgen: a simple-to-use, generalized workflow for membrane-protein-lipid-bilayer system building. *J Chem Inf Model*. 2019;59(6):2522–2528. https://doi.org/10.1021/acs.jcim.9b00269.
215. Knight CJ, Hub JS. MemGen: a general web server for the setup of lipid membrane simulation systems. *Bioinformatics*. 2015;31(17):2897–2899. https://doi.org/10.1093/bioinformatics/btv292.
216. Martínez L, Andrade R, Birgin EG, Martínez JM. PACKMOL: a package for building initial configurations for molecular dynamics simulations. *J Comput Chem*. 2009;30(13):2157–2164. https://doi.org/10.1002/jcc.21224.
217. Humphrey W, Dalke A, Schulten K. VMD: visual molecular dynamics. *J Mol Graph*. 1996;14(1):33–38. https://doi.org/10.1016/0263-7855(96)00018-5.
218. Faraldo-Gómez JD, Smith GR, Sansom MS. Setting up and optimization of membrane protein simulations. *Eur Biophys J*. 2002;31(3):217–227. https://doi.org/10.1007/s00249-002-0207-5.
219. Kandt C, Ash WL, Tieleman DP. Setting up and running molecular dynamics simulations of membrane proteins. *Methods*. 2007;41(4):475–488. https://doi.org/10.1016/j.ymeth.2006.08.006.
220. Schmidt TH, Kandt C. LAMBADA and InflateGRO2: efficient membrane alignment and insertion of membrane proteins for molecular dynamics simulations. *J Chem Inf Model*. 2012;52(10):2657–2669. https://doi.org/10.1021/ci3000453.
221. Wolf MG, Hoefling M, Aponte-Santamaría C, Grubmller H, Groenhof G. g_membed: efficient insertion of a membrane protein into an equilibrated lipid bilayer with minimal perturbation. *J Comput Chem*. 2010;31(11):2169–2174. https://doi.org/10.1002/jcc.21507.
222. Javanainen M, Martinez-Seara H. Efficient preparation and analysis of membrane and membrane protein systems. *Biochim Biophys Acta Biomembr*. 2016;1858(10):2468–2482. https://doi.org/10.1016/j.bbamem.2016.02.036.
223. Ghahremanpour MM, Arab SS, Aghazadeh SB, Zhang J, van der Spoel D. MemBuilder: a web-based graphical interface to build heterogeneously mixed membrane bilayers for the GROMACS biomolecular simulation program. *Bioinformatics*. 2013;30(3):439–441. https://doi.org/10.1093/bioinformatics/btt680.

224. Wassenaar TA, Ingólfsson HI, Böckmann RA, Tieleman DP, Marrink SJ. Computational lipidomics with insane: a versatile tool for generating custom membranes for molecular simulations. *J Chem Theory Comput*. 2015;11(5):2144–2155. https://doi.org/10.1021/acs.jctc.5b00209.
225. Gutmann T, Schäfer IB, Poojari C, et al. Cryo-EM structure of the complete and ligand-saturated insulin receptor ectodomain. *J Cell Biol*. 2020;219(1). https://doi.org/10.1083/jcb.201907210.
226. Mobarak E, Håversen L, Manna M, et al. Glucosylceramide modifies the LPS-induced inflammatory response in macrophages and the orientation of the LPS/TLR4 complex in silico. *Sci Rep*. 2018;8(1):13600.
227. Kaszuba K, Grzybek M, Orłowski A, et al. N-glycosylation as determinant of epidermal growth factor receptor conformation in membranes. *Proc Natl Acad Sci*. 2015;112(14):4334–4339. https://doi.org/10.1073/pnas.1503262112.
228. Danne R, Poojari C, Martinez-Seara H, et al. doGlycans-tools for preparing carbohydrate structures for atomistic simulations of glycoproteins, glycolipids, and carbohydrate polymers for GROMACS. *J Chem Inf Model*. 2017;57(10):2401–2406. https://doi.org/10.1021/acs.jcim.7b00237.
229. Park SJ, Lee J, Qi Y, et al. CHARMM-GUI glycan modeler for modeling and simulation of carbohydrates and glycoconjugates. *Glycobiology*. 2019;29(4):320–331. https://doi.org/10.1093/glycob/cwz003.
230. Case DA, Ben-Shalom IY, Brozell SR, et al. *AMBER 2019*. San Francisco: University of California; 2019.
231. McGibbon RT, Beauchamp KA, Harrigan MP, et al. MDTraj: a modern open library for the analysis of molecular dynamics trajectories. *Biophys J*. 2015;109(8):1528–1532. https://doi.org/10.1016/j.bpj.2015.08.015.
232. Schrödinger LLC. *The PyMOL Molecular Graphics System, Version 1.8;* 2015.
233. Pettersen EF, Goddard TD, Huang CC, et al. Ucsf chimera—a visualization system for exploratory research and analysis. *J Comput Chem*. 2004;25(13):1605–1612. https://doi.org/10.1002/jcc.20084.
234. Natick M. *MATLAB version 9.1 (R2016b)*. The Mathworks, Inc.; 2016.
235. Williams T. Gnuplot 4.4: an interactive plotting program; 2010. http://www.gnuplot.info/docs_4.4/gnuplot.pdf.
236. Romo TD, Grossfield A. LOOS: an extensible platform for the structural analysis of simulations. *2009 Annual International Conference of the IEEE Engineering in Medicine and Biology Society*. 2009:2332–2335. https://doi.org/10.1109/IEMBS.2009.5335065.
237. Gapsys V, de Groot BL, Rodolfo R. Computational analysis of local membrane properties. *J Comput Aided Mol Des*. 2013;27(10):845–858. https://doi.org/10.1007/s10822-013-9684-0.
238. Allen WJ, Lemkul JA, Bevan DR. GridMAT-MD: a grid-based membrane analysis tool for use with molecular dynamics. *J Comput Chem*. 2009;30(12):1952–1958. https://doi.org/10.1002/jcc.21172.
239. Carr M, MacPhee CE. Membrainy: a 'smart', unified membrane analysis tool. *Source Code Biol Med*. 2015;10(1):3.
240. Guixà-González R, Rodriguez-Espigares I, Ramírez-Anguita JM, et al. MEMBPLUGIN: studying membrane complexity in VMD. *Bioinformatics*. 2014;30(10):1478–1480. https://doi.org/10.1093/bioinformatics/btu037.
241. Buchoux S. FATSLiM: a fast and robust software to analyze MD simulations of membranes. *Bioinformatics*. 2016;33(1):133–134. https://doi.org/10.1093/bioinformatics/btw563.
242. Castillo N, Monticelli L, Barnoud J, Tieleman DP. Free energy of WALP23 dimer association in DMPC, DPPC, and DOPC bilayers. *Chem Phys Lipids*. 2013;169:95–105. https://doi.org/10.1016/j.chemphyslip.2013.02.001.

243. Michaud-Agrawal N, Denning EJ, Woolf TB, Beckstein O. MDAnalysis: a toolkit for the analysis of molecular dynamics simulations. *J Comput Chem*. 2011;32(10): 2319–2327. https://doi.org/10.1002/jcc.21787.
244. Hilger D, Masureel M, Kobilka BK. Structure and dynamics of GPCR signaling complexes. *Nat Struct Mol Biol*. 2018;25(1):4–12.
245. Sriram K, Insel PA. G protein-coupled receptors as targets for approved drugs: how many targets and how many drugs? *Mol Pharmacol*. 2018;93(4):251–258. https://doi.org/10.1124/mol.117.111062.
246. Paila YD, Chattopadhyay A. The function of G-protein coupled receptors and membrane cholesterol: specific or general interaction? *Glycoconj J*. 2008;26(6):711. https://doi.org/10.1007/s10719-008-9218-5.
247. Oates J, Watts A. Uncovering the intimate relationship between lipids, cholesterol and GPCR activation. *Curr Opin Struct Biol*. 2011;21(6):802–807. https://doi.org/10.1016/j.sbi.2011.09.007.
248. Pucadyil TJ, Chattopadhyay A. Cholesterol modulates ligand binding and G-protein coupling to serotonin1A receptors from bovine hippocampus. *Biochim Biophys Acta Biomembr*. 2004;1663(1):188–200. https://doi.org/10.1016/j.bbamem.2004.03.010.
249. Gimpl G, Fahrenholz F. Cholesterol as stabilizer of the oxytocin receptor. *Biochim Biophys Acta Biomembr*. 2002;1564(2):384–392. https://doi.org/10.1016/S0005-2736(02)00475-3.
250. Jastrzebska B, Debinski A, Filipek S, Palczewski K. Role of membrane integrity on G protein-coupled receptors: rhodopsin stability and function. *Prog Lipid Res*. 2011;50(3):267–277. https://doi.org/10.1016/j.plipres.2011.03.002.
251. Cherezov V, Rosenbaum DM, Hanson MA, et al. High-resolution crystal structure of an engineered human β2-adrenergic G protein-coupled receptor. *Science*. 2007;318(5854):1258–1265. https://doi.org/10.1126/science.1150577.
252. Michael FB. Modulation of rhodopsin function by properties of the membrane bilayer. *Chem Phys Lipids*. 1994;73(1):159–180. https://doi.org/10.1016/0009-3084(94)90180-5.
253. Manna M, Niemelä M, Tynkkynen J, et al. Mechanism of allosteric regulation of β_2-adrenergic receptor by cholesterol. *eLife*. 2016;5:e18432. https://doi.org/10.7554/eLife.18432.
254. Cang X, Yang L, Yang J, et al. Cholesterol-β1AR interaction versus cholesterol-β2AR interaction. *Proteins*. 2014;82(5):760–770. https://doi.org/10.1002/prot.24456.
255. Paila YD, Tiwari S, Sengupta D, Chattopadhyay A. Molecular modeling of the human serotonin1A receptor: role of membrane cholesterol in ligand binding of the receptor. *Mol BioSyst*. 2011;7(1):224–234. https://doi.org/10.1039/C0MB00148A.
256. Shan J, Khelashvili G, Mondal S, Mehler EL, Weinstein H. Ligand-dependent conformations and dynamics of the serotonin 5-HT2A receptor determine its activation and membrane-driven oligomerization properties. *PLoS Comput Biol*. 2012;8(4):1–15. https://doi.org/10.1371/journal.pcbi.1002473.
257. Hurst DP, Grossfield A, Lynch DL, et al. A lipid pathway for ligand binding is necessary for a cannabinoid G protein-coupled receptor. *J Biol Chem*. 2010;285(23): 17954–17964.
258. Pitman MC, Grossfield A, Suits F, Feller SE. Role of cholesterol and polyunsaturated chains in lipid-protein interactions: molecular dynamics simulation of rhodopsin in a realistic membrane environment. *J Am Chem Soc*. 2005;127(13):4576–4577. https://doi.org/10.1021/ja042715y.
259. Lee JY, Lyman E. Predictions for cholesterol interaction sites on the A_{2A} adenosine receptor. *J Am Chem Soc*. 2012;134(40):16512–16515. https://doi.org/10.1021/ja307532d.

260. Lyman E, Higgs C, Kim B, et al. A role for a specific cholesterol interaction in stabilizing the Apo configuration of the human A_{2A} adenosine receptor. *Structure*. 2009;17(12):1660–1668.
261. Marino KA, Shang Y, Filizola M. Insights into the function of opioid receptors from molecular dynamics simulations of available crystal structures. *Br J Pharmacol*. 2018;175(14):2834–2845.
262. Yuan S, Wu R, Latek D, Trzaskowski B, Filipek S. Lipid receptor S1P1 activation scheme concluded from microsecond all-atom molecular dynamics simulations. *PLoS Comput Biol*. 2013;9(10):1–8. https://doi.org/10.1371/journal.pcbi.1003261.
263. Morra G, Razavi AM, Pandey K, Weinstein H, Menon AK, Khelashvili G. Mechanisms of lipid scrambling by the G protein-coupled receptor opsin. *Structure*. 2018;26(2):356–367.
264. Montgomery D, Campbell A, Sullivan HJ, Wu C. Molecular dynamics simulation of biased agonists at the dopamine D2 receptor suggests the mechanism of receptor functional selectivity. *J Biomol Struct Dyn*. 2019;37(12):3206–3225.
265. Liu W, Chun E, Thompson AA, et al. Structural basis for allosteric regulation of GPCRs by sodium ions. *Science*. 2012;337(6091):232–236. https://doi.org/10.1126/science.1219218.
266. Guixà-González R, Albasanz JL, Rodriguez-Espigares I, et al. Membrane cholesterol access into a G-protein-coupled receptor. *Nat Commun*. 2017;8:14505.
267. Jaakola VP, Griffith MT, Hanson MA, et al. The 2.6 angstrom crystal structure of a human A2A adenosine receptor bound to an antagonist. *Science*. 2008;322(5905): 1211–1217. https://doi.org/10.1126/science.1164772.
268. Ernst OP, Menon AK. Phospholipid scrambling by rhodopsin. *Photochem Photobiol Sci*. 2015;14:1922–1931. https://doi.org/10.1039/C5PP00195A.
269. Goren MA, Morizumi T, Menon I, et al. Constitutive phospholipid scramblase activity of a G protein-coupled receptor. *Nat Commun*. 2014;5:5115.
270. Menon I, Huber T, Sanyal S, et al. Opsin is a phospholipid flippase. *Curr Biol*. 2011;21(2):149–153. https://doi.org/10.1016/j.cub.2010.12.031.
271. Pomorski TG, Menon AK. Lipid somersaults: uncovering the mechanisms of protein-mediated lipid flipping. *Prog Lipid Res*. 2016;64:69–84. https://doi.org/10.1016/j.plipres.2016.08.003.
272. Bevers EM, Williamson PL. Getting to the outer leaflet: physiology of phosphatidylserine exposure at the plasma membrane. *Physiol Rev*. 2016;96(2):605–645. https://doi.org/10.1152/physrev.00020.2015.
273. Pomorski T, Menon AK. Lipid flippases and their biological functions. *Cell Mol Life Sci*. 2006;63(24):2908–2921. https://doi.org/10.1007/s00018-006-6167-7.
274. Sanyal S, Menon AK. Flipping lipids: why an' what's the reason for? *ACS Chem Biol*. 2009;4(11):895–909. https://doi.org/10.1021/cb900163d.
275. Ploier B, Menon AK. A fluorescence-based assay of phospholipid scramblase activity. *J Vis Exp*. 2016;115:1–8.
276. Alberts B, Johnson A, Lewis J, Raff M, Roberts K, Walter P. Principles of membrane transport. In: Alberts B, Johnson A, Lewis J, Raff M, Roberts K, Walter P, eds. In: *Molecular Biology of the Cell*. 4th ed. Garland Science; 2002:1585–1603.
277. Martens C, Shekhar M, Borysik AJ, et al. Direct protein-lipid interactions shape the conformational landscape of secondary transporters. *Nat Commun*. 2018;9(1):4151.
278. Quistgaard EM, Löw C, Moberg P, Trésaugues L, Nordlund P. Structural basis for substrate transport in the GLUT-homology family of monosaccharide transporters. *Nat Struct Mol Biol*. 2013;20(6):766.
279. Mirza O, Guan L, Verner G, Iwata S, Kaback HR. Structural evidence for induced fit and a mechanism for sugar/H+ symport in LacY. *EMBO J*. 2006;25(6):1177–1183. https://doi.org/10.1038/sj.emboj.7601028.

280. Khelashvili G, Stanley N, Sahai MA, et al. Spontaneous inward opening of the dopamine transporter is triggered by PIP_2-regulated dynamics of the N-Terminus. *ACS Chem Neurosci*. 2015;6(11):1825–1837. https://doi.org/10.1021/acschemneuro.5b00179.
281. Penmatsa A, Gouaux E. How LeuT shapes our understanding of the mechanisms of sodium-coupled neurotransmitter transporters. *J Physiol*. 2014;592(5):863–869. https://doi.org/10.1113/jphysiol.2013.259051.
282. Nichols CG, Lopatin AN. Inward rectifier potassium channels. *Annu Rev Physiol*. 1997;59(1):171–191. https://doi.org/10.1146/annurev.physiol.59.1.171.
283. Hibino H, Inanobe A, Furutani K, Murakami S, Findlay I, Kurachi Y. Inwardly rectifying potassium channels: their structure, function, and physiological roles. *Physiol Rev*. 2010;90(1):291–366. https://doi.org/10.1152/physrev.00021.2009.
284. Rosenhouse-Dantsker A, Noskov S, Durdagi S, Durdagi S, Logothetis DE, Levitan I. Identification of novel cholesterol-binding regions in Kir2 channels. *J Biolog Chem*. 2013;288(43):31154–31164. https://doi.org/10.1074/jbc.M113.496117.
285. Spiro RG. Glycoproteins. In: Anfinsen CB, Edsall JT, Richards FM, eds. vol. 27. *Advances in Protein Chemistry*. Academic Press; 1973:349–467. https://doi.org/10.1016/S0065-3233(08)60451-9.
286. Meyer B, Möller H. Conformation of glycopeptides and glycoproteins. In: Wittmann V, ed. *Glycopeptides and Glycoproteins: Synthesis, Structure, and Application*. Berlin, Heidelberg: Springer; 2007:187–251. https://doi.org/10.1007/128_2006_078.
287. Wormald MR, Rudd PM, Harvey DJ, Chang SC, Scragg IG, Dwek RA. Variations in oligosaccharide-protein interactions in immunoglobulin G determine the site-specific glycosylation profiles and modulate the dynamic motion of the Fc oligosaccharides. *Biochemistry*. 1997;36(6):1370–1380. https://doi.org/10.1021/bi9621472.
288. Shental-Bechor D, Levy Y. Folding of glycoproteins: toward understanding the biophysics of the glycosylation code. *Curr Opin Struct Biol*. 2009;19(5):524–533. https://doi.org/10.1016/j.sbi.2009.07.002.
289. Shental-Bechor D, Levy Y. Effect of glycosylation on protein folding: a close look at thermodynamic stabilization. *Proc Natl Acad Sci*. 2008;105(24):8256–8261. https://doi.org/10.1073/pnas.0801340105.
290. Flintegaard TV, Thygesen P, Rahbek-Nielsen H, et al. N-glycosylation increases the circulatory half-life of human growth hormone. *Endocrinology*. 2010;151(11):5326–5336. https://doi.org/10.1210/en.2010-0574.
291. Van Kooyk Y, Rabinovich GA. Protein-glycan interactions in the control of innate and adaptive immune responses. *Nat Immunol*. 2008;9(6):593.
292. Spiro RG. Protein glycosylation: nature, distribution, enzymatic formation, and disease implications of glycopeptide bonds. *Glycobiology*. 2002;12(4). https://doi.org/10.1093/glycob/12.4.43R43R–56R.
293. Shinzawa-Itoh K, Aoyama H, Muramoto K, et al. Structures and physiological roles of 13 integral lipids of bovine heart cytochrome c oxidase. *EMBO J*. 2007;26(6):1713–1725. https://doi.org/10.1038/sj.emboj.7601618.
294. Malkamäki A, Sharma V. Atomistic insights into cardiolipin binding sites of cytochrome c oxidase. *Biochim Biophys Acta*. 2019;1860(3):224–232. https://doi.org/10.1016/j.bbabio.2018.11.004.
295. Dudkina NV, Kouřil R, Peters K, Braun HP, Boekema EJ. Structure and function of mitochondrial supercomplexes. *Biochim Biophys Acta*. 2010;1797(6):664–670. https://doi.org/10.1016/j.bbabio.2009.12.013.
296. Osellame LD, Blacker TS, Duchen MR. Cellular and molecular mechanisms of mitochondrial function. *Best Pract Res Clin Endocrinol Metab*. 2012;26(6):711–723. https://doi.org/10.1016/j.beem.2012.05.003.
297. Schmidt O, Pfanner N, Meisinger C. Mitochondrial protein import: from proteomics to functional mechanisms. *Nat Rev Mol Cell Biol*. 2010;11(9):655.

298. Friedman JR, Nunnari J. Mitochondrial form and function. *Nature*. 2014;505(7483): 335–343.
299. Duchen MR. Mitochondria and calcium: from cell signalling to cell death. *J Physiol*. 2000;529(1):57–68. https://doi.org/10.1111/j.1469-7793.2000.00057.x.
300. Hill S, Remmen HV. Mitochondrial stress signaling in longevity: a new role for mitochondrial function in aging. *Redox Biol*. 2014;2:936–944. https://doi.org/10.1016/j.redox.2014.07.005.
301. Kühlbrandt W. Structure and function of mitochondrial membrane protein complexes. *BMC Biol*. 2015;13(1):89. https://doi.org/10.1186/s12915-015-0201-x.
302. Schlame M, Towbin JA, Heerdt PM, Jehle R, DiMauro S, Blanck TJJ. Deficiency of tetralinoleoyl-cardiolipin in Barth syndrome. *Ann Neurol*. 2002;51(5):634–637. https://doi.org/10.1002/ana.10176.
303. Valianpour F, Wanders RJA, Barth PG, Overmars H, van Gennip AH. Quantitative and compositional study of cardiolipin in platelets by electrospray ionization mass spectrometry: application for the identification of Barth syndrome patients. *Clin Chem*. 2002;48(9):1390–1397. http://clinchem.aaccjnls.org/content/48/9/1390.
304. Hunte C. Specific protein-lipid interactions in membrane proteins. *Biochem Soc Trans*. 2005;33(5):938–942. https://doi.org/10.1042/BST0330938.
305. Sedlák E, Robinson NC. Phospholipase A2 digestion of cardiolipin bound to bovine cytochrome c oxidase alters both activity and quaternary structure. *Biochemistry*. 1999;38(45):14966–14972. https://doi.org/10.1021/bi9914053.
306. Hardy J, Selkoe DJ. The amyloid hypothesis of Alzheimer's disease: progress and problems on the road to therapeutics. *Science*. 2002;297(5580):353–356. https://doi.org/10.1126/science.1072994.
307. Selkoe DJ. Alzheimer's disease is a synaptic failure. *Science*. 2002;298(5594):789–791. https://doi.org/10.1126/science.1074069.
308. Selkoe DJ. Alzheimer's disease: genes, proteins, and therapy. *Physiol Rev*. 2001;81(2):741–766. https://doi.org/10.1152/physrev.2001.81.2.741.
309. Yan Y, Wang C. Aβ42 is more rigid than Aβ40 at the C terminus: implications for Aβ aggregation and toxicity. *J Mol Biol*. 2006;364(5):853–862. https://doi.org/10.1016/j.jmb.2006.09.046.
310. Kayed R, Head E, Thompson JL, et al. Common structure of soluble amyloid oligomers implies common mechanism of pathogenesis. *Science*. 2003;300(5618):486–489. https://doi.org/10.1126/science.1079469.
311. Haass C, Selkoe DJ. Soluble protein oligomers in neurodegeneration: lessons from the Alzheimer's amyloid β-peptide. *Nat Rev Mol Cell Biol*. 2007;8(2):101.
312. Chimon S, Shaibat MA, Jones CR, Calero DC, Aizezi B, Ishii Y. Evidence of fibril-like β-sheet structures in a neurotoxic amyloid intermediate of Alzheimer's β-amyloid. *Nat Struct Mol Biol*. 2007;14(12):1157.
313. Straub JE, Thirumalai D. Membrane-protein interactions are key to understanding amyloid formation. *J Phys Chem Lett*. 2014;5(3):633–635. https://doi.org/10.1021/jz500054d.
314. Vestergaard M, Hamada T, Takagi M. Using model membranes for the study of amyloid beta:lipid interactions and neurotoxicity. *Biotechnol Bioeng*. 2008;99(4):753–763. https://doi.org/10.1002/bit.21731.
315. Matsuzaki K. Physicochemical interactions of amyloid β-peptide with lipid bilayers. *Biochim Biophys Acta Biomembr*. 2007;1768(8):1935–1942. https://doi.org/10.1016/j.bbamem.2007.02.009.
316. Butterfield SM, Lashuel HA. Amyloidogenic protein-membrane interactions: mechanistic insight from model systems. *Angew Chem Int Ed*. 2010;49(33):5628–5654. https://doi.org/10.1002/anie.200906670.
317. Makin OS, Serpell LC. The structure of amyloid. *Fibre Diffr Rev*. 2004;12:29–35.

318. Williams TL, Serpell LC. Membrane and surface interactions of Alzheimer's Aβ peptide–insights into the mechanism of cytotoxicity. *FEBS J*. 2011;278(20):3905–3917. https://doi.org/10.1111/j.1742-4658.2011.08228.x.
319. Poojari C, Kukol A, Strodel B. How the amyloid-β peptide and membranes affect each other: an extensive simulation study. *Biochim Biophys Acta Biomembr*. 2013;1828(2):327–339. https://doi.org/10.1016/j.bbamem.2012.09.001.
320. Poojari C, Strodel B. Stability of transmembrane amyloid β-peptide and membrane integrity tested by molecular modeling of site-specific Aβ42 mutations. *PLoS ONE*. 2013;8(11):1–12. https://doi.org/10.1371/journal.pone.0078399.
321. Lemkul JA, Bevan DR. Lipid composition influences the release of Alzheimer's amyloid β-peptide from membranes. *Protein Sci*. 2011;20(9):1530–1545. https://doi.org/10.1002/pro.678.
322. Owen MC, Kulig W, Poojari C, Rog T, Strodel B. Physiologically-relevant levels of sphingomyelin, but not GM1, induces a β-sheet-rich structure in the amyloid-β(1-42) monomer. *Biochim Biophys Acta Biomembr*. 2018;1860(9):1709–1720. https://doi.org/10.1016/j.bbamem.2018.03.026.
323. Ntarakas N, Ermilova I, Lyubartsev AP. Effect of lipid saturation on amyloid-beta peptide partitioning and aggregation in neuronal membranes: molecular dynamics simulations. *Eur Biophys J*. 2019;48(8):813–824. https://doi.org/10.1007/s00249-019-01407-x.
324. Lu Y, Shi XF, Nguyen PH, Sterpone F, Salsbury FR, Derreumaux P. Amyloid-β(29-42) dimeric conformations in membranes rich in omega-3 and omega-6 polyunsaturated fatty acids. *J Phys Chem B*. 2019;123(12):2687–2696. https://doi.org/10.1021/acs.jpcb.9b00431.
325. Söderberg M, Edlund C, Kristensson K, Dallner G. Fatty acid composition of brain phospholipids in aging and in Alzheimer's disease. *Lipids*. 1991;26(6):421. https://doi.org/10.1007/BF02536067.
326. Wood PL. Lipidomics of Alzheimer's disease: current status. *Alzheimer's Res Ther*. 2012;4(1):5.
327. Söderberg M, Edlund C, Alafuzoff I, Kristensson K, Dallner G. Lipid composition in different regions of the brain in Alzheimer's disease/senile dementia of Alzheimer's type. *J Neurochem*. 1992;59(5):1646–1653. https://doi.org/10.1111/j.1471-4159.1992.tb10994.x.
328. Hossain S, Hashimoto M, Katakura M, Miwa K, Shimada T, Shido O. Mechanism of docosahexaenoic acid-induced inhibition of in vitro Aβ1-42 fibrillation and Aβ1-42-induced toxicity in SH-S5Y5 cells. *J Neurochem*. 2009;111(2):568–579. https://doi.org/10.1111/j.1471-4159.2009.06336.x.
329. Ionov M, Klajnert B, Gardikis K, et al. Effect of amyloid beta peptides Aβ1-28 and Aβ25-40 on model lipid membranes. *J Thermal Anal Calorim*. 2010;99(3):741–747. https://doi.org/10.1007/s10973-009-0405-9.
330. Jia Y, Qian Z, Zhang Y, Wei G. Adsorption and orientation of human islet amyloid polypeptide (hIAPP) monomer at anionic lipid bilayers: implications for membrane-mediated aggregation. *Int J Mol Sci*. 2013;14(3):6241–6258.
331. Qian Z, Jia Y, Wei G. Binding orientations and lipid interactions of human amylin at zwitterionic and anionic lipid bilayers. *J Diabetes Res*. 2016;2016:1–13.
332. Dong X, Qiao Q, Qian Z, Wei G. Recent computational studies of membrane interaction and disruption of human islet amyloid polypeptide: monomers, oligomers and protofibrils. *Biochim Biophys Acta Biomembr*. 2018;1860(9):1826–1839. https://doi.org/10.1016/j.bbamem.2018.03.006.
333. Dignon GL, Zerze GH, Mittal J. Interplay between membrane composition and structural stability of membrane-bound hIAPP. *J Phys Chem B*. 2017;121(37):8661–8668. https://doi.org/10.1021/acs.jpcb.7b05689.

334. Zhang Y, Luo Y, Deng Y, Mu Y, Wei G. Lipid interaction and membrane perturbation of human islet amyloid polypeptide monomer and dimer by molecular dynamics simulations. *PLoS ONE*. 2012;7(5):1–10. https://doi.org/10.1371/journal.pone.0038191.
335. Zhao J, Luo Y, Jang H, et al. Probing ion channel activity of human islet amyloid polypeptide (amylin). *Biochim Biophys Acta Biomembr*. 2012;1818(12):3121–3130. https://doi.org/10.1016/j.bbamem.2012.08.012.
336. Zhao J, Hu R, Sciacca MFM, et al. Non-selective ion channel activity of polymorphic human islet amyloid polypeptide (amylin) double channels. *Phys Chem Chem Phys*. 2014;16:2368–2377. https://doi.org/10.1039/C3CP53345J.
337. Quist A, Doudevski I, Lin H, et al. Amyloid ion channels: a common structural link for protein-misfolding disease. *Proc Natl Acad Sci*. 2005;102(30):10427–10432. https://doi.org/10.1073/pnas.0502066102.
338. Poojari C, Xiao D, Batista VS, Strodel B. Membrane permeation induced by aggregates of human islet amyloid polypeptides. *Biophys J*. 2013;105(10):2323–2332. https://doi.org/10.1016/j.bpj.2013.09.045.
339. Luca S, Yau WM, Leapman R, Tycko R. Peptide conformation and supramolecular organization in amylin fibrils: constraints from solid-state NMR. *Biochemistry*. 2007;46(47):13505–13522. https://doi.org/10.1021/bi701427q.
340. Bedrood S, Li Y, Isas JM, et al. Fibril structure of human islet amyloid polypeptide. *J Biol Chem*. 2012;287(8):5235–5241. https://doi.org/10.1074/jbc.M111.327817.
341. Xiao D, Fu L, Liu J, Batista VS, Yan ECY. Amphiphilic adsorption of human islet amyloid polypeptide aggregates to lipid/aqueous interfaces. *J Mol Biol*. 2012;421(4):537–547. https://doi.org/10.1016/j.jmb.2011.12.035.
342. Yasuda T, Nakata Y, Mochizuki H. α-synuclein and neuronal cell death. *Mol Neurobiol*. 2013;47(2):466–483. https://doi.org/10.1007/s12035-012-8327-0.
343. Rao JN, Dua V, Ulmer TS. Characterization of α-synuclein interactions with selected aggregation-inhibiting small molecules. *Biochemistry*. 2008;47(16):4651–4656. https://doi.org/10.1021/bi8002378.
344. Press-Sandler O, Miller Y. Molecular mechanisms of membrane-associated amyloid aggregation: computational perspective and challenges. *Biochim Biophys Acta Biomembr*. 2018;1860(9):1889–1905. https://doi.org/10.1016/j.bbamem.2018.03.014.
345. Eliezer D, Kutluay E, Bussell R, Browne G. Conformational properties of α-synuclein in its free and lipid-associated states. *J Mol Biol*. 2001;307(4):1061–1073. https://doi.org/10.1006/jmbi.2001.4538.
346. Ulmer TS, Bax A, Cole NB, Nussbaum RL. Structure and dynamics of micelle-bound human α-synuclein. *J Biol Chem*. 2005;280(10):9595–9603. https://doi.org/10.1074/jbc.M411805200.
347. Rao JN, Jao CC, Hegde BG, Langen R, Ulmer TS. A combinatorial NMR and EPR approach for evaluating the structural ensemble of partially folded proteins. *J Am Chem Soc*. 2010;132(25):8657–8668. https://doi.org/10.1021/ja100646t.
348. Li B, Ge P, Murray KA, et al. Cryo-EM of full-length α-synuclein reveals fibril polymorphs with a common structural kernel. *Nat Commun*. 2018;9(1):3609.
349. Pfefferkorn CM, Heinrich F, Sodt AJ, et al. Depth of α-synuclein in a bilayer determined by fluorescence, neutron reflectometry, and computation. *Biophys J*. 2012;102(3):613–621. https://doi.org/10.1016/j.bpj.2011.12.051.
350. Perlmutter JD, Braun AR, Sachs JN. Curvature dynamics of α-synuclein familial Parkinson disease mutants: molecular simulations of the micelle- and bilayer-bound forms. *J Biol Chem*. 2009;284(11):7177–7189. https://doi.org/10.1074/jbc.M808895200.
351. Garten M, Prévost C, Cadart C, et al. Methyl-branched lipids promote the membrane adsorption of α-synuclein by enhancing shallow lipid-packing defects. *Phys Chem Chem Phys*. 2015;17:15589–15597. https://doi.org/10.1039/C5CP00244C.

352. Viennet T, Wördehoff MM, Uluca B, et al. Structural insights from lipid-bilayer nanodiscs link α-synuclein membrane-binding modes to amyloid fibril formation. *Commun Biol*. 2018;1(1):44.
353. Bikfalvi A, Klein S, Pintucci G, Rifkin DB. Biological roles of fibroblast growth factor-2*. *Endocrine Reviews*. 1997;18(1):26–45. https://doi.org/10.1210/edrv.18.1.0292.
354. Presta M, Dell'Era P, Mitola S, Moroni E, Ronca R, Rusnati M. Fibroblast growth factor/fibroblast growth factor receptor system in angiogenesis. *Cytokine Growth Factor Rev*. 2005;16(2):159–178. https://doi.org/10.1016/j.cytogfr.2005.01.004.
355. Noh KH, Kim SH, Kim JH, et al. API5 confers tumoral immune escape through FGF2-dependent cell survival pathway. *Cancer Research*. 2014;74(13):3556–3566. https://doi.org/10.1158/0008-5472.CAN-13-3225.
356. Pardo OE, Wellbrock C, Khanzada UK, et al. FGF-2 protects small cell lung cancer cells from apoptosis through a complex involving PKCε, B-Raf and S6K2. *EMBO J*. 2006;25(13):3078–3088. https://doi.org/10.1038/sj.emboj.7601198.
357. La Venuta G, Zeitler M, Steringer JP, Müller HM, Nickel W. The startling properties of fibroblast growth factor 2: how to exit mammalian cells without a signal peptide at hand. *J Biol Chem*. 2015;290(45):27015–27020. https://doi.org/10.1074/jbc.R115.689257.
358. Nickel W. The unconventional secretory machinery of fibroblast growth factor 2. *Traffic*. 2011;12(7):799–805. https://doi.org/10.1111/j.1600-0854.2011.01187.x.
359. Nickel W, Rabouille C. Mechanisms of regulated unconventional protein secretion. *Nat Rev Mol cell Biol*. 2009;10(2):148.
360. Nickel W. Unconventional secretion: an extracellular trap for export of fibroblast growth factor 2. *J Cell Sci*. 2007;120(14):2295–2299. https://doi.org/10.1242/jcs.011080.
361. Temmerman K, Ebert AD, Müller HM, Sinning I, Tews I, Nickel W. A direct role for phosphatidylinositol-4,5-bisphosphate in unconventional secretion of fibroblast growth factor 2. *Traffic*. 2008;9(7):1204–1217. https://doi.org/10.1111/j.1600-0854.2008.00749.x.
362. Steringer JP, Bleicken S, Andreas H, et al. Phosphatidylinositol 4,5-bisphosphate (pi(4,5)p2)-dependent oligomerization of fibroblast growth factor 2 (fgf2) triggers the formation of a lipidic membrane pore implicated in unconventional secretion. *J Biol Chem*. 2012;287(33):27659–27669. https://doi.org/10.1074/jbc.M112.381939.
363. Steringer JP, Müller HM, Nickel W. Unconventional secretion of fibroblast growth factor 2-a novel type of protein translocation across membranes? *J Mol Biol*. 2015;427(6, Pt. A):1202–1210. https://doi.org/10.1016/j.jmb.2014.07.012.
364. Müller HM, Steringer JP, Wegehingel S, et al. Formation of disulfide bridges drives oligomerization, membrane pore formation, and translocation of fibroblast growth factor 2 to cell surfaces. *J Biol Chem*. 2015;290(14):8925–8937. https://doi.org/10.1074/jbc.M114.622456.
365. Steringer JP, Lange S, Čujová S, et al. Key steps in unconventional secretion of fibroblast growth factor 2 reconstituted with purified components. *eLife*. 2017;6:e28985. https://doi.org/10.7554/eLife.28985.
366. Rayne F, Debaisieux S, Bonhoure A, Beaumelle B. HIV-1 Tat is unconventionally secreted through the plasma membrane. *Cell Biol Int*. 2010;34(4):409–413. https://doi.org/10.1042/CBI20090376.
367. Debaisieux S, Rayne F, Yezid H, Beaumelle B. The ins and outs of HIV-1 Tat. *Traffic*. 2012;13(3):355–363. https://doi.org/10.1111/j.1600-0854.2011.01286.x.
368. Vitale N, Beaumelle B, Bader MF, Tryoen-Toth P. HIV-1 Tat protein perturbs diacylglycerol production at the plasma membrane of neurosecretory cells during exocytosis. *Commun Integr Biol*. 2013;6(5):e25145. https://doi.org/10.4161/cib.25145.

369. Martín-Sánchez F, Diamond C, Zeitler M, et al. Inflammasome-dependent il-1β release depends upon membrane permeabilisation. *Cell Death Differ*. 2016;23(7):1219.
370. Cho W, Stahelin RV. Membrane-protein interactions in cell signaling and membrane trafficking. *Annu Rev Biophys Biomol Struct*. 2005;34(1):119–151. https://doi.org/10.1146/annurev.biophys.33.110502.133337.
371. Di Paolo G, De Camilli P. Phosphoinositides in cell regulation and membrane dynamics. *Nature*. 2006;443(7112):651.
372. Kutateladze TG. Translation of the phosphoinositide code by PI effectors. *Nat Chem Biol*. 2010;6(7):507.
373. Stahelin RV, Scott JL, Frick CT. Cellular and molecular interactions of phosphoinositides and peripheral proteins. *Chem Phys Lipids*. 2014;182:3–18. https://doi.org/10.1016/j.chemphyslip.2014.02.002.
374. Lemmon MA. Membrane recognition by phospholipid-binding domains. *Nat Rev Mol Cell Biol*. 2008;9(2):99.
375. Morales KA, Igumenova TI. Synergistic effect of pb2+ and phosphatidylinositol 4,5-bisphosphate on c2 domain-membrane interactions. *Biochemistry*. 2012;51(16):3349–3360. https://doi.org/10.1021/bi201850h.
376. Lai CL, Landgraf KE, Voth GA, Falke JJ. Membrane docking geometry and target lipid stoichiometry of membrane-bound PKCα C2 domain: a combined molecular dynamics and experimental study. *J Mol Biol*. 2010;402(2):301–310. https://doi.org/10.1016/j.jmb.2010.07.037.
377. Ceccarelli DFJ, Blasutig IM, Goudreault M, et al. Non-canonical interaction of phosphoinositides with pleckstrin homology domains of Tiam1 and ArhGAP9. *J Biol Chem*. 2007;282(18):13864–13874. https://doi.org/10.1074/jbc.M700505200.
378. Jian X, Tang WK, Zhai P, et al. Molecular basis for cooperative binding of anionic phospholipids to the PH domain of the Arf GAP ASAP1. *Structure*. 2015;23(11):1977–1988. https://doi.org/10.1016/j.str.2015.08.008.
379. Pant S, Tajkhorshid E. Microscopic characterization of GRP1 PH domain interaction with anionic membranes. *J Comput Chem*. 2019;9999:1–11. https://doi.org/10.1002/jcc.26109.
380. Senju Y, Kalimeri M, Koskela EV, et al. Mechanistic principles underlying regulation of the actin cytoskeleton by phosphoinositides. *Proc Natl Acad Sci*. 2017;114(43):E8977–E8986. https://doi.org/10.1073/pnas.1705032114.
381. DiNitto JP, Delprato A, Lee MTG, et al. Structural basis and mechanism of autoregulation in 3-phosphoinositide-dependent Grp1 family Arf GTPase exchange factors. *Mol Cell*. 2007;28(4):569–583. https://doi.org/10.1016/j.molcel.2007.09.017.
382. Fuss B, Becker T, Zinke I, Hoch M. The cytohesin Steppke is essential for insulin signalling in Drosophila. *Nature*. 2006;444(7121):945.
383. Hafner M, Schmitz A, Grüne I, et al. Inhibition of cytohesins by SecinH3 leads to hepatic insulin resistance. *Nature*. 2006;444(7121):941.
384. Claing A, Chen W, Miller WE, et al. β-arrestin-mediated ADP-ribosylation factor 6 activation and β2-adrenergic receptor endocytosis. *J Biol Chem*. 2001;276(45):42509–42513. https://doi.org/10.1074/jbc.M108399200.
385. Clodi M, Vollenweider P, Klarlund J, et al. Effects of general receptor for phosphoinositides 1 on insulin and insulin-like growth factor I-induced cytoskeletal rearrangement, glucose transporter-4 translocation, and deoxyribonucleic acid synthesis. *Endocrinology*. 1998;139(12):4984–4990. https://doi.org/10.1210/endo.139.12.6351.
386. Frank SR, Hatfield JC, Casanova JE. Remodeling of the actin cytoskeleton is coordinately regulated by protein kinase C and the ADP-ribosylation factor nucleotide exchange factor ARNO. *Mol Biol Cell*. 1998;9(11):3133–3146. https://doi.org/10.1091/mbc.9.11.3133.

387. Blanchoin L, Boujemaa-Paterski R, Sykes C, Plastino J. Actin dynamics, architecture, and mechanics in cell motility. *Physiol Rev*. 2014;94(1):235–263.
388. Pollard TD, Cooper JA. Actin, a central player in cell shape and movement. *Science*. 2009;326(5957):1208–1212. https://doi.org/10.1126/science.1175862.
389. Saarikangas J, Zhao H, Lappalainen P. Regulation of the actin cytoskeleton-plasma membrane interplay by phosphoinositides. *Physiol Rev*. 2010;90(1):259–289. https://doi.org/10.1152/physrev.00036.2009.
390. Yin HL, Janmey PA. Phosphoinositide regulation of the actin cytoskeleton. *Annu Rev Physiol*. 2003;65(1):761–789. https://doi.org/10.1146/annurev.physiol.65.092101.142517.
391. Gorelik R, Yang C, Kameswaran V, Dominguez R, Svitkina T. Mechanisms of plasma membrane targeting of formin mDia2 through its amino terminal domains. *Mol Biol Cell*. 2011;22(2):189–201. https://doi.org/10.1091/mbc.e10-03-0256.
392. van Rheenen J, Song X, van Roosmalen W, et al. EGF-induced PIP2 hydrolysis releases and activates cofilin locally in carcinoma cells. *J Cell Biol*. 2007;179(6):1247–1259. https://doi.org/10.1083/jcb.200706206.
393. Chinthalapudi K, Rangarajan ES, Patil DN, George EM, Brown DT, Izard T. Lipid binding promotes oligomerization and focal adhesion activity of vinculin. *J Cell Biol*. 2014;207(5):643–656. https://doi.org/10.1083/jcb.201404128.
394. Rivera MG, Vasilescu D, Papayannopoulos V, Lim WA, Mayer BJ. A reciprocal interdependence between Nck and PI(4,5)P2 promotes localized N-WASp-mediated actin polymerization in living cells. *Mol Cell*. 2009;36(3):525–535. https://doi.org/10.1016/j.molcel.2009.10.025.
395. Wollman R, Meyer T. Coordinated oscillations in cortical actin and Ca2+ correlate with cycles of vesicle secretion. *Nat Cell Biol*. 2012;14(12):1261.
396. Yonezawa N, Nishida E, Iida K, Yahara I, Sakai H. Inhibition of the interactions of cofilin, destrin, and deoxyribonuclease I with actin by phosphoinositides. *J Biol Chem*. 1990;265(15):8382–8386.
397. Janmey PA, Stossel TP. Modulation of gelsolin function by phosphatidylinositol 4,5-bisphosphate. *Nature*. 1987;325(6102):362.
398. Schafer DA, Jennings PB, Cooper JA. Dynamics of capping protein and actin assembly in vitro: uncapping barbed ends by polyphosphoinositides. *J Cell Biol*. 1996;135(1):169–179. https://doi.org/10.1083/jcb.135.1.169.
399. Prehoda KE, Scott JA, Mullins RD, Lim WA. Integration of multiple signals through cooperative regulation of the N-WASP-Arp2/3 complex. *Science*. 2000;290(5492):801–806. https://doi.org/10.1126/science.290.5492.801.
400. Rohatgi R, Ho HYH, Kirschner MW. Mechanism of N-wasp activation by CDC42 and phosphatidylinositol 4,5-bisphosphate. *J Cell Biol*. 2000;150(6):1299–1310. https://doi.org/10.1083/jcb.150.6.1299.
401. Martel V, Racaud-Sultan C, Dupe S, et al. Conformation, localization, and integrin binding of talin depend on its interaction with phosphoinositides. *J Biol Chem*. 2001;276(24):21217–21227. https://doi.org/10.1074/jbc.M102373200.
402. Yamamoto M, Hilgemann DH, Feng S, et al. Phosphatidylinositol 4,5-bisphosphate induces actin stress-fiber formation and inhibits membrane ruffling in Cv1 cells. *J Cell Biol*. 2001;152(5):867–876. https://doi.org/10.1083/jcb.152.5.867.
403. Raucher D, Stauffer T, Chen W, et al. Phosphatidylinositol 4,5-bisphosphate functions as a second messenger that regulates cytoskeleton-plasma membrane adhesion. *Cell*. 2000;100(2):221–228. https://doi.org/10.1016/S0092-8674(00)81560-3.
404. Rozelle AL, Machesky LM, Yamamoto M, et al. Phosphatidylinositol 4,5-bisphosphate induces actin-based movement of raft-enriched vesicles through WASP-Arp2/3. *Curr Biol*. 2000;10(6):311–320. https://doi.org/10.1016/S0960-9822(00)00384-5.

405. Cunningham CC, Vegners R, Bucki R, et al. Cell permeant polyphosphoinositide-binding peptides that block cell motility and actin assembly. *J Biol Chem*. 2001;276(46):43390–43399. https://doi.org/10.1074/jbc.M105289200.
406. Kielian M. Mechanisms of virus membrane fusion proteins. *Annu Rev Virol*. 2014;1(1):171–189. https://doi.org/10.1146/annurev-virology-031413-085521.
407. Kim IS, Jenni S, Stanifer ML, et al. Mechanism of membrane fusion induced by vesicular stomatitis virus G protein. *Proc Natl Acad Sci*. 2017;114(1):E28–E36. https://doi.org/10.1073/pnas.1618883114.
408. Guardado-Calvo P, Atkovska K, Jeffers SA, et al. A glycerophospholipid-specific pocket in the RVFV class II fusion protein drives target membrane insertion. *Science*. 2017;358(6363):663–667. https://doi.org/10.1126/science.aal2712.
409. Mizushima N. Autophagy: process and function. *Genes Dev*. 2007;21(22):2861–2873. https://doi.org/10.1101/gad.1599207. http://genesdev.cshlp.org/content/21/22/2861.abstract.
410. Lee WS, Yoo WH, Chae HJ. ER stress and autophagy. *Curr Mol Med*. 2015;15(8):735–745.
411. Kirkin V, Lamark T, Sou YS, et al. A role for NBR1 in autophagosomal degradation of ubiquitinated substrates. *Mol Cell*. 2009;33(4):505–516. https://doi.org/10.1016/j.molcel.2009.01.020.
412. Khaminets A, Heinrich T, Mari M, et al. Regulation of endoplasmic reticulum turnover by selective autophagy. *Nature*. 2015;522:354–3581. https://doi.org/10.1038/nature14498.
413. Brady JP, Claridge JK, Smith PG, Schnell JR. A conserved amphipathic helix is required for membrane tubule formation by Yop1p. *Proc Natl Acad Sci*. 2015;112(7):E639–E648. https://doi.org/10.1073/pnas.1415882112.
414. Breeze E, Dzimitrowicz N, Kriechbaumer V, et al. A C-terminal amphipathic helix is necessary for the in vivo tubule-shaping function of a plant reticulon. *Proc Natl Acad Sci*. 2016;113(39):10902–10907. https://doi.org/10.1073/pnas.1605434113.
415. Hu J, Shibata Y, Voss C, Rist JM, Rapoport TA. Membrane proteins of the endoplasmic reticulum induce high-curvature tubules. *Science*. 2008;319(5867):1247–1250. https://doi.org/10.1126/science.1153634.
416. Voeltz GK, Prinz WA, Shibata Y, et al. A class of membrane proteins shaping the tubular endoplasmic reticulum. *Cell*. 2006;124(3):573–586. https://doi.org/10.1016/j.cell.2005.11.047.
417. Bhaskara RM, Grumati P, Garcia-Pardo J, et al. Curvature induction and membrane remodeling by FAM134B reticulon homology domain assist selective ER-phagy. *Nat Commun*. 2019;10(1):1–13.
418. Walther TC, Farese RV. Lipid droplets and cellular lipid metabolism. *Annu Rev Biochem*. 2012;81(1):687–714. https://doi.org/10.1146/annurev-biochem-061009-102430.
419. Zoni V, Campomanes P, Khaddaj R, Thiam AR, Schneiter R, Vanni S. Lipid droplet biogenesis is driven by liquid-liquid phase separation. *bioRxiv*. 2020. https://doi.org/10.1101/777466.
420. Bacle A, Gautier R, Jackson CL, Fuchs PFJ, Vanni S. Interdigitation between triglycerides and lipids modulates surface properties of lipid droplets. *Biophys J*. 2017;112(7):1417–1430. https://doi.org/10.1016/j.bpj.2017.02.032.
421. MacDermaid CM, Kashyap HK, DeVane RH, et al. Molecular dynamics simulations of cholesterol-rich membranes using a coarse-grained force field for cyclic alkanes. *J Chem Phys*. 2015;143(24):243144. https://doi.org/10.1063/1.4937153.
422. Campomanes P, Zoni V, Vanni SL. Local accumulation of diacylglycerol alters membrane properties nonlinearly due to its transbilayer activity. *Commun Chem*. 2019;2:1–8.

423. Shinoda W, DeVane R, Klein ML. Coarse-grained molecular modeling of non-ionic surfactant self-assembly. *Soft Matter*. 2008;4:2454–2462. https://doi.org/10.1039/B808701F.
424. Yan R, Qian H, Lukmantara I, et al. Human SEIPIN binds anionic phospholipids. *Dev Cell*. 2018;47(2):248–256.e4. https://doi.org/10.1016/j.devcel.2018.09.010.
425. Salo Y, Li S, Vihinen H, et al. Seipin facilitates triglyceride flow to lipid droplet and counteracts droplet ripening via endoplasmic reticulum contact. *Dev Cell*. 2019;50(4). https://doi.org/10.1016/j.devcel.2019.05.016478–493.e9.
426. Cartwright BR, Binns DD, Hilton CL, Han S, Gao Q, Goodman JM. Seipin performs dissectible functions in promoting lipid droplet biogenesis and regulating droplet morphology. *Mol Biol Cell*. 2015;26(4):726–739. https://doi.org/10.1091/mbc.E14-08-1303.
427. Nettebrock NT, Bohnert M. Born this way—biogenesis of lipid droplets from specialized ER subdomains. *Biochim Biophys Acta*. 2020;1865(1). https://doi.org/10.1016/j.bbalip.2019.04.008.
428. Dupuy AD, Engelman DM. Protein area occupancy at the center of the red blood cell membrane. *Proc Natl Acad Sci*. 2008;105(8):2848–2852. https://doi.org/10.1073/pnas.0712379105.
429. Nyholm TKM. Lipid-protein interplay and lateral organization in biomembranes. *Chem Phys Lipids*. 2015;189:48–55. https://doi.org/10.1016/j.chemphyslip.2015.05.008.
430. Contreras FX, Ernst AM, Wieland F, Brügger B. Specificity of intramembrane protein-lipid interactions. *Cold Spring Harb Perspect Biol*. 2011;3(6):1–18. https://doi.org/10.1101/cshperspect.a004705.
431. Corradi V, Mendez-Villuendas E, Ingólfsson HI, et al. Lipid-protein interactions are unique fingerprints for membrane proteins. *ACS Cent Sci*. 2018;4(6):709–717. https://doi.org/10.1021/acscentsci.8b00143.